University of California
Santa Barbara

Acoustic patterning of 3D printed composites for anisotropic conductivity and multifunctionality

A dissertation submitted in partial satisfaction
of the requirements for the degree

Doctor of Philosophy
in
Materials

by

Drew Shrader Melchert

Committee in charge:

Professor Daniel Gianola, Chair
Professor Matthew Begley
Professor Christopher Bates
Professor Carl Meinhart

March 2022

The Dissertation of Drew Shrader Melchert is approved.

Professor Matthew Begley

Professor Christopher Bates

Professor Carl Meinhart

Professor Daniel Gianola, Committee Chair

December 2021

Acoustic patterning of 3D printed composites for anisotropic conductivity and multifunctionality

by

Drew Shrader Melchert

Acknowledgements

I would like to thank all the people who contributed to this work: My primary advisor, Prof. Dan Gianola, first of all for giving me the opportunity to join his group. His guidance and mentorship throughout the years has been invaluable, and he is a continual source of insightful scientific and professional ideas. Dan's ability to track the details of my work and suggest promising directions for research while encouraging a healthy degree of decision-making freedom has made my research a joy. My co-advisor, Prof. Matt Begley, has provided inspiring discussions and direction for my projects, and keeping research ideas grounded and useful but still intellectually interesting and fun to work on.

The Gianola and Begley research groups at UCSB have been wonderful for discussions and activities outside of work. Between the companionship, feedback, brainstorming, and troubleshooting sessions, these groups have been a joy to be a part of. My research builds off the efforts of group members Rachel Collino, Tyler Ray, Leanne Friedrich, Keith Johnson, and Danny Strickland; to them I am also grateful for all the support over the years.

Thank you to my other committee members, Professors Chris Bates and Carl Meinhart, for having open doors for discussion and feedback. The Materials Department administration and Microscopy Facility, Microfluidics Lab, and Materials Preparation Lab and their staff were of great aid to this work.

During the last two years, I have had the opportunity to conduct my graduate research at Lawrence Livermore National Laboratory in the Materials Engineering Division led by Dr. Christopher Spadaccini. The support from Chris and his group has been incredible, providing entirely new research avenues and professional development opportunities. I would like to acknowledge my funding during this time by the UC Laboratory Fees Research Program In-Residence Graduate Fellowship LGF-20-654,066. Earlier work was supported

by the Institute for Collaborative Biotechnologies through contract no. W911NF-09-D-0001 from the U.S. Army Research Office.

Other discussions, particularly with collaborators Dr. Neil Dolinski and Veronica Reynolds, Matthew Wong, Amir Tahmasebipour and Dr. Danny Strickland, were excellent ways to learn about others' research and advance my own.

Finally, thank you to my friends for making this such a fun time of life here in Santa Barbara, to my peers for inspiring excellence in research and life, and to my family for being so wonderful and supportive, and for getting me to where I am now.

Curriculum Vitæ

Drew Shrader Melchert

Education

2021	Ph.D. in Materials (Expected), University of California, Santa Barbara.
2016	M.A. in Physics, University of Chicago.

Professional Appointments

- UC-National Laboratory In-Residence Graduate Fellowship at Lawrence Livermore National Laboratory, 2020-2022

Publications

- D. S. Melchert, A. Tahmasebipour, D. S. Gianola, C. Meinhart, M. R. Begley, C. Spadaccini. "Anisotropic thermally conductive composites enabled by acoustophoresis and stereolithography." *In preparation* **2021**.
- D. S. Melchert, K. Johnson, B. Giera, E. J. Fong, M. Shusteff, J. Mancini, J. J. Karnes, C. L. Cobb, C. Spadaccini, D. S. Gianola, M. R. Begley. "Modeling meso-and microstructure in materials patterned with acoustic focusing." *Materials & Design* **2021**, *202*, p. 1170607.
- M. S. Wong, D. Melchert, M. Haggmark, D. J. Myers, S. Grandrothula, M. de Vries, D. Gianola, M. Begley, T. Magarlith, J. S. Speck, S. P. Den-Baars, S. Nakamura. "Acousto-fluidic assembly of III-nitride micro-light-emitting diodes with magnetic alignment." *Light-Emitting Devices, Materials, and Applications XXV* **2021**, *202*, 109512.
- D. J. Strickland, D. S. Melchert, J. L. Hor, C. P. Ortiz, D. Lee, D. S. Gianola. "Microscopic origin of shear banding as a localized driven glass transition in compressed colloidal pillars." *Physical Review E* **2020**, *102*, 032605.
- D. S. Melchert, R. R. Collino, T. R. Ray, N. D. Dolinski, L. Friedrich, M. R. Begley, D. S. Gianola. "Flexible conductive composites with programmed electrical anisotropy using acoustophoresis." *Advanced Materials Technologies* **2019**, 1900586.
- M. Sadati, Y. Zhou, D. Melchert, A. Guo, J. Martinez-Gonzalez, T. F. Roberts, R. Zhang, J. J. de Pablo. "Spherical nematic shell with prolate ellipsoidal core." *Soft Matter* **2017**.
- D. F. Agterberg, D. S. Melchert, M. K. Kashyap. "Emergent loop current order from pair wave superconductivity." *Physical Review B* **2015**, *91*, 5.

Abstract

Acoustic patterning of 3D printed composites for anisotropic conductivity and multifunctionality

by

Drew Shrader Melchert

A versatile class of composite materials composed of functional filler particles in polymer matrices are increasingly used in high-performance applications that leverage their adaptable mechanical, electrical, thermal, and other functional properties. The choice of constituent materials largely determines these properties: for example, long fibers redistribute stress efficiently, highly conductive filler particles impart their conductivity to the material, and combinations of ionic and electrically conductive fillers with energy storage materials increase the capacity of battery electrodes. The performance of these composites, however, is highly dependent on the internal arrangement of particles. Consequently, controlling this internal structure enables property improvements and novel functionalities. In particular, combining microstructure control with the design freedom of 3D printing presents opportunities to maximize the performance of functional components by spatially modulating properties and their directionality (e.g. reinforcing high-stress regions, prescribing electrical interconnects, or directing heat away from hot spots), as well as introducing novel combinations of properties.

To develop this structural control in printed materials, this work utilizes pressure fields to assemble filler particles into patterns within composites during 3D printing. Particle patterns are engineered to improve material properties by leveraging microscopic acoustic forces on particles, tailoring the particle arrangement for improvements in the functionality of the material. This acoustic patterning technique is integrated into 3D printing with

attention to processing constraints (e.g. component and feature sizes, material properties, cost, throughput rate, etc.) required in existing and emerging technological applications. In particular, 3D printed composites with high electrical or thermal conductivity, which are simultaneously mechanically flexible or strain-tolerant, are targeted for advancing the emerging fields of flexible electronics and soft robotics, and for alleviating the bottleneck in cooling of electronic devices.

Acoustically patterned composites exhibit increased electrical and thermal conductivity (by many orders of magnitude under some conditions) compared to conventional, unpatterned composites via concentrated particle contact density and optimized transport pathways. Simultaneously, patterning enhances mechanical flexibility by reducing the required loading of filler particles and encapsulating conductive particle networks in thick sheathes of strain-absorbing polymer. The magnitude and directionality of electrical and thermal transport is configurable over a wide range via manipulation of the orientation and connectivity of filler particles, introducing processing routes for printing components with embedded electrical interconnects or directional cooling networks.

Computational modeling of acoustic forces probes the design space of possible particle structures, which are compared to detailed particle-level material characterization to understand and then optimize the patterning process for desired microstructures. These structural details inform the physics of electrical and thermal conduction between particles in the material as well as particle rearrangements during mechanical deformation. Finally, this work investigates methods for expanding control over composite microstructure, including patterning hierarchically structured particles and manipulating particles with multiple external fields.

Thesis: Assembling particles into patterns within composite materials using pressure fields during 3D printing improves functionalities like anisotropic electrical and thermal conductivity and enables novel combinations of properties, filling research gaps for

multifunctional composites. This dissertation presents evidence in defence of this thesis.

Contents

Chapter 1

Introduction

1.1 General Introduction

This dissertation investigates the use of sound in materials engineering. "Sound" refers to vibrations that travel through a medium like air, for example those created by plucking a guitar string. The string transfers its vibration to the top of the guitar body, which in turn pushes against the surrounding air, sending vibrations through the air until they disturb tiny hairs in our ears, which we sense as hearing. As these vibrations travel through the air we describe them as pressure waves, which refers to the alternating compression and expansion of the air. We can quantify frequency of this alternation (which we sense as the pitch of a sound), as well as the amplitude and direction of travel, as part of this wave description. We can control the frequency of these waves for example by changing the length or tension of a guitar string so that it vibrates at different rates, but the speed of their travel is fixed by the speed of sound of the medium ($\sim$750 miles per hour in air, $\sim$3000 miles per hour in water, numbers determined in part by how easy it is to compress the medium). We experience the reflection of these waves off of hard surfaces as echoes, and in denser media (e.g. underwater) we observe how sounds can travel further and

reflect more times before dying out.

These are the intuitive underlying physics of acoustic phenomena, which can be extended to smaller size scales in science and engineering for powerful effects. At higher frequencies, the size of the wave itself (the distance between compressed and expanded regions in the medium, called the wavelength) shrinks. Waves with shorter wavelength will reflect off of smaller obstacles, whereas longer wavelength (lower frequency) waves can bend or diffract around small obstacles instead of totally reflecting, reforming behind the obstacle because only a small portion of the wave is disturbed by it. As a result, high-frequency waves can be used to detect reflections off of small obstacles in a process called echo-location, used for example by bats for finding mosquitoes in the dark. Since the sound bats use to do this is higher frequency than that audible by humans (>20 kHz), it is called "ultrasound." We can mimic this echo-location ability with technology called ultrasound imaging, which detects obstacles in the human body (e.g. tissues and fluids with different densities) on a size scale down to about 200 µm, about half the thickness of a fingernail, using pressure waves with frequencies of 2-20 MHz. A similar process is used to quickly detect tiny cracks or voids in the frames and fuselages of airplanes before they pose serious threat of damage, which would otherwise be difficult to catch because they may be buried within the structure of the plane.

In addition to being detected for echo-location, when these pressure waves reflect off the surfaces of small obstacles, they also exert forces on the obstacles. Similarly to how we can feel loud sounds in our body (especially when underwater, because the coupling between water and our water-based bodies is better than with air), and in more extreme cases how loud sounds rupture eardrums and how shockwaves knock things over, the reflection of waves imparts a portion of their momentum to the solid obstacle. On small scales this force can be exploited to move particles around. In water, this acoustic manipulation can move particles as small as ∼0.5 µm, which is about the size of a bacteria (red blood cells

are ∼5 µm wide, and human hair is ∼70 µm thick). While this acoustic manipulation is used most often in biological applications for sorting cells (e.g. sorting the fat cells out of blood), it can be used on particles made of any solid material, e.g. plastic, metal, ceramic, etc.

This material-agnostic feature of acoustic particle manipulation introduces opportunities in materials engineering to assemble small filler particles into patterns within materials during fabrication. These patterns can significantly improve the properties of materials when designed properly. For example, wood is made up of many ∼20 µm fibers, all aligned and woven into patterns (wood grain) that give it high stiffness and strength along the direction of the fibers, though it may be prone to splitting in the perpendicular directions. Trees orient these patterns in complex curved paths to support massive cantilevered loads in their trunks and branches[1]. In engineered materials, carbon fiber composites (made of carbon fibers in epoxy) accomplish similar properties by aligning the carbon fibers along the directions in a part that need to be strong before allowing the epoxy to cure.

In this work, pressure fields are used to align and pattern filler particles (including carbon fibers) in polymer matrices (like epoxy). The particles are small relative to the wavelength, so the waves are not fully reflected but only slightly disturbed (scattered) and can continue propagating. The particles are pushed to the low-pressure nodes of the pressure wave (similarly to how sand moves on a plate over a speaker), as illustrated in Figure 1.1, typically aligning and concentrating into lines that change with the sound frequency, creating composites with architected particle patterns.

As shown in Figure 1.2, the architecture of acoustically patterned composites is controlled on several length scales. Macroscopically, i.e. on the scale of the samples or printed components themselves (millimeters to centimeters), the geometry of the samples is determined by the fabrication process, and with 3D printing this macroscale geometry is highly customizable. On the mesoscale (hundreds of micrometers), the acoustically assembled

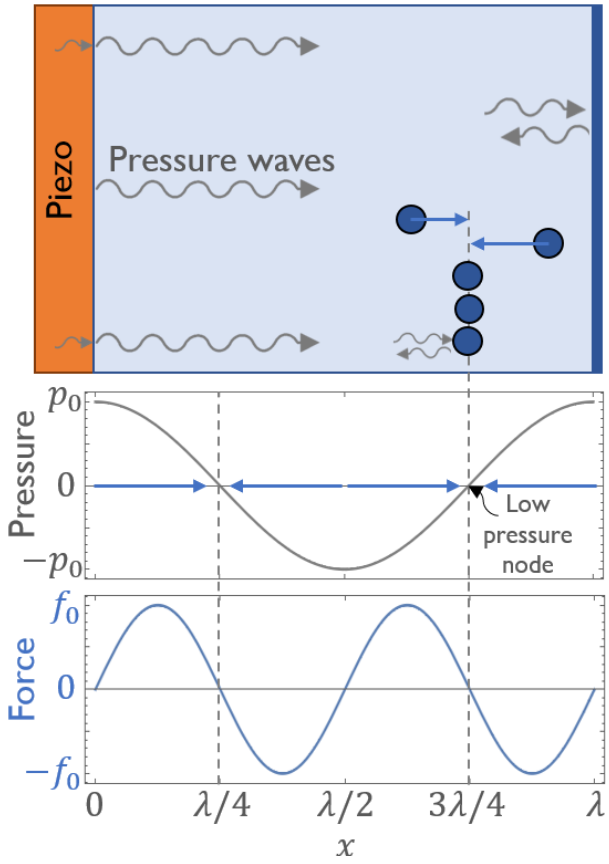

Figure 1.1: A schematic illustrating the pressure waves (oscillating in the time domain) induced in a fluid by a vibrating piezoelectric transducer. The pressure waves, when driven at a resonant frequency of the channel, form a sinusoidal standing pressure wave, periodic in space with wavelength λ. The time-averaged pressure field exerts a force on particles that pushes them along the gradient of the pressure field to low-pressure nodes (via a second-order effect i.e. the time-averaged square of pressure).

patterns themselves have features like stripe spacing, width, and interconnectivity that are controlled via acoustic parameters and particle properties. On the microscale (∼0.5-100 µm), the arrangement of particles can be modulated by leveraging particle geometry and acoustic forces to pack particles into configurations that optimize the functionality of the material.

1.2 State of the Art

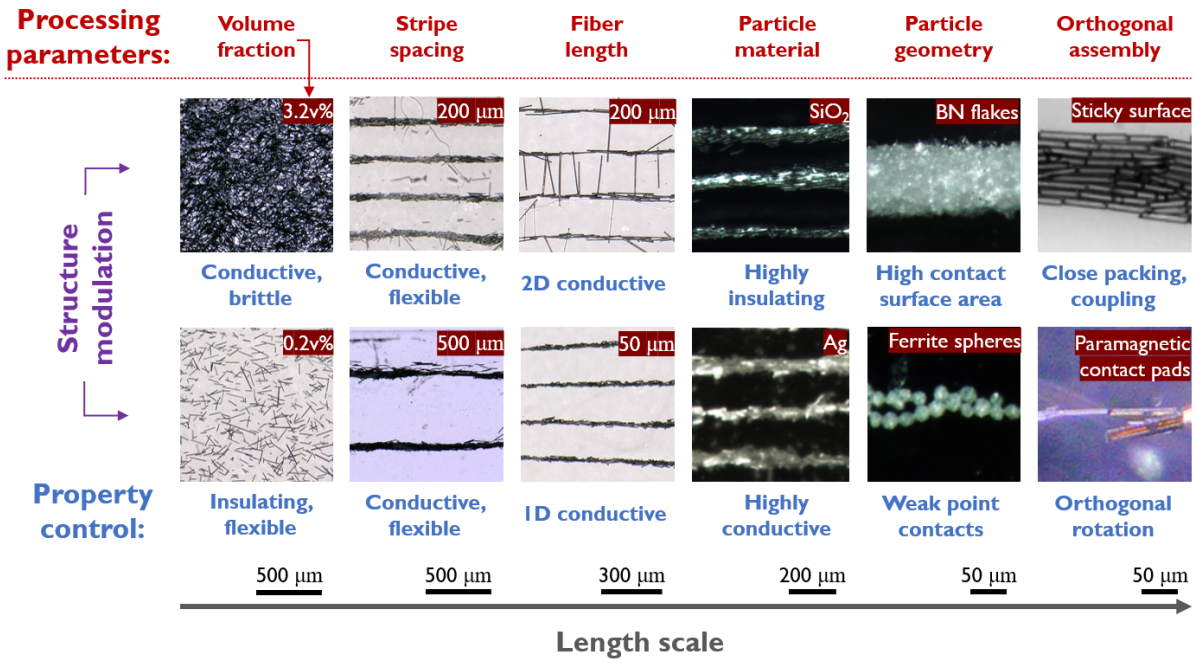

Figure 1.2: A table of the variety of processing parameters available in acoustic patterning, with examples of various structural states that can be modulated between, and the resulting properties they control.

Architected materials have proven useful in structural[2–4], electrical[5–8], thermal[9–11], and electrochemical[12–18] applications because their functional properties can be significantly improved over their unpatterned counterparts by optimizing microstructure for the application at hand, e.g. to redistribute stress or guide electrical, thermal, or species transport[19,20], Detailed, application-grounded discussions and literature comparisons of

patterned and unpatterned composites' electrical and thermal conductivity are given in the introductions of Sections 3.1 and 3.2 of this dissertation, and mechanical flexibility is surveyed in Sections 3.2 and 4.1.

Such patterned materials have been fabricated by directly printing the microstructure (e.g. with microstereolithography)[2,21–23], utilizing stochastic patterning approaches like freeze-casting[24,25], or using self or directed assembly during processing[26–31]. While direct printing and self assembly of microstructure are limited in speed and scale[32,33], directed assembly is emerging as a powerful approach for fast, large-scale patterning, particularly when integrated into 3D printing of composite materials (consisting of filler particles within a polymer or ceramic matrix)[20,26]. Directed assembly using pressure fields, i.e. acoustophoresis of filler particles, in particular has advantages in its versatility in particle and matrix material choices, micron-to-cm scale capabilities, up to mm/s speed, and numerous degrees of freedom in particle manipulation[28,34].

Acoustophoresis allows for deterministic particle positioning, in contrast to electromagnetic field assisted assembly[29–31,35] or hydrodynamic shear alignment[4,36,37] which quickly rotate particles but cannot reliably translate particles into predetermined patterns, though it can chain particles very slowly (taking upwards of 10 minutes)[38–40]. Versatility in particle placement allows optimization of properties (especially in transport applications where particles must be translated into networks), and acoustic focusing is unique in meeting this need by allowing assembly of complex patterns, even of user-defined patterns[41–43]. Acoustic focusing can also handle a larger variety of particle and fluid materials than electromagnetic assembly because it depends only on the contrast in density and compressibility between the particle and fluid material, not permittivity (as in dielectrophoresis), conductivity, charge (as in electrophoresis), magnetism, or other material properties[26,44]. Other stochastic approaches like freeze-casting or laser-directed alignment[25] show promise for patterning certain materials, but these are generally restricted to specific material

systems and microstructural configurations.

Acoustophoresis is also highly scalable, assembling µm- to mm-size structures in seconds[45–47], in contrast to self-assembly processes that are limited by diffusion rates and are prohibitively slow to assemble >10 µm structures[45–47]. Though used primarily for cell sorting and other biological characterization[44,48], acoustic focusing has attracted interest in materials design for non-invasively patterning functional materials[28,41,49–52], and has garnered interest for use in 3D printing via direct ink writing[45,53,54] and stereolithography[41,51]. Electrical elements have been successfully printed with the latter method in recent years[41,51], although the acoustic reservoir print bath used in stereolithography has yet limited it to producing $\lesssim$ 50 mm components; direct ink writing is scalable to larger-scale applications. Assembly and printing dynamics of direct-ink write printing with acoustophoresis has been studied[45,53–55] as an approach which avoids the filler particle size and resolution limitations, material compatibility issues, and the high production time, complexity, and cost associated with multiple-nozzle printing of embedded functional elements[36,56–59].

1.3 Motivation and Scope

The motivation for patterning particles in composite materials is to form particle structures that enhance the properties of the material. Long fibers like those in wood and carbon fiber composites, if they are longer than the wavelength of the pressure field, cross multiple low pressure nodes and thus cannot be reliably aligned or moved large distances[28,60]. As a result, automating the layup of carbon fiber composites or other structural materials is best addressed with other methods, because the long fibers are necessary to distribute stress over large distances (which is what gives carbon fiber and wood its strength)[61,62]. Many other applications, however, use short fibers or flakes, which

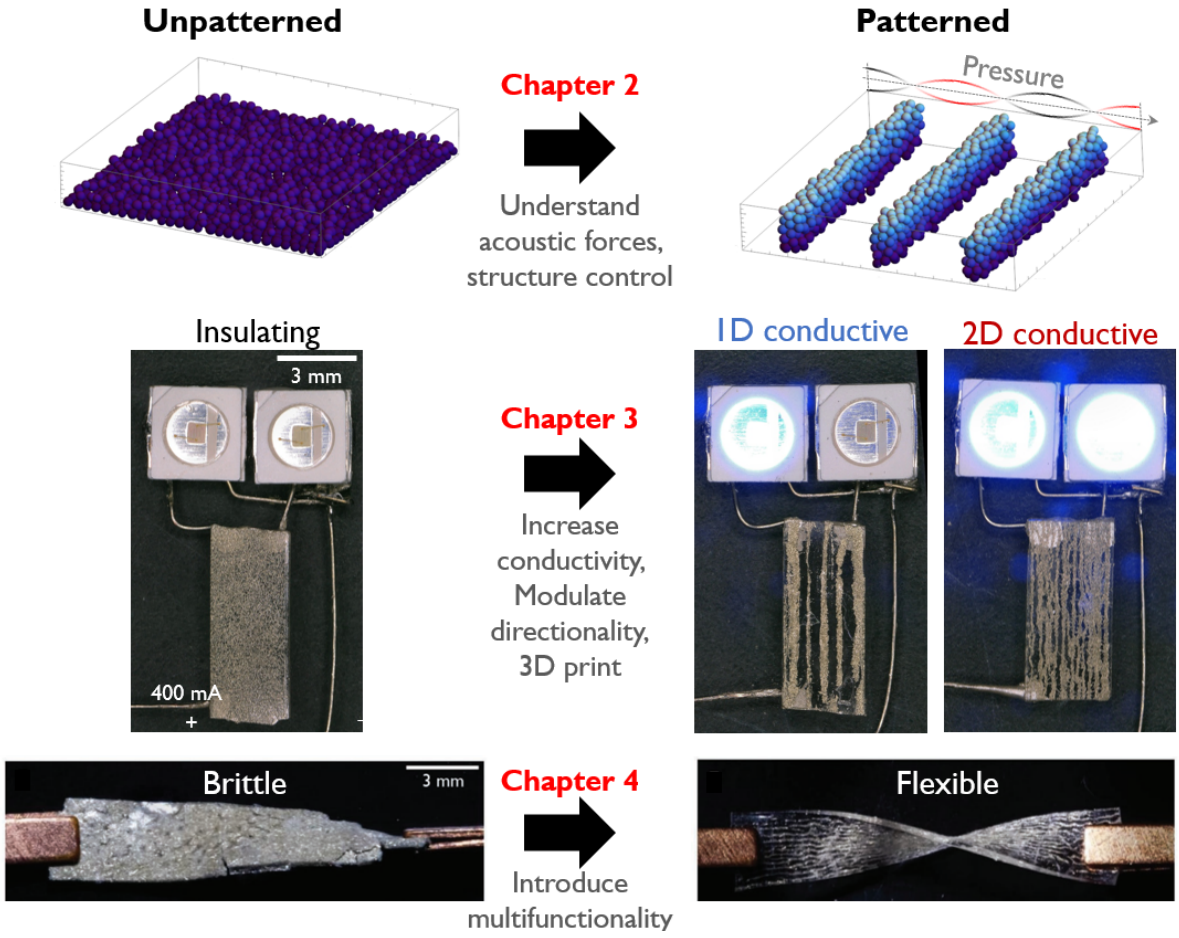

Figure 1.3: An illustration of the property enhancements possible by patterning composites using pressure fields, including modulating the magnitude and directionality of electrical conductivity and improving the strain tolerance of conductive materials, along with an outline of the main themes of each chapter of this dissertation.

see strong benefits from patterning these types of filler particles into engineered structures.

Electrically conductive composites present a promising opportunity for wiring electronics in complex devices at lower cost than traditional wiring processes[63,64]. Particularly when combined with 3D printing, which is pushing the frontier of design complexity, next-generation printed components with integrated electronics have complex capabilities at lower cost, e.g. inexpensive medical diagnostic tools, wearable sensors that monitor bodily functions, conventional and soft robots, etc[5,63,65,66].

Electrically conductive composites, however, are severely limited because polymers like epoxy are electrically insulating. This limitation requires very high loading of conductive (typically metallic) filler particles to reach high conductivity (as detailed in Section 3.1)[6,28,67]. The conductive particles must come into contact and form a continuous contacting circuit across the material to become conductive, which, when relying on filler particles randomly mixed into polymer, requires a high loading of particles to increase the chances of forming a continuous network. Using acoustic particle manipulation, however, the filler particles are aligned and compacted into stripes, requiring much fewer particles[28]. This effect, shown in Figure 1.3 and investigated in Section 3.1, increases conductivity by orders of magnitude, and lowers the filler particle loading required for high conductivity. This lower filler particle loading in turn improves the mechanical flexibility of the material significantly, allowing use in wearable electronics which need to flex with our skin, as detailed in Section 4.1. In addition, more complex patterns are assembled to modulate the conductivity of the material between insulating material, 1D conductive material (i.e. wires running in one direction in the material), and 2D (nearly-isotropic) conductive material, all using the same ink. Using this method, 3D printed parts with integrated electrical interconnects and flexible hinges can be fabricated.

Along a similar vein, the thermal conductivity of composites can be maximized along certain directions. As electronic components miniaturize, the bottleneck in further power

density improvements is increasingly limitations in cooling, instead of smaller component size[65,68,69]. Since fabricating smaller aluminum or copper heatsinks incurs a large processing cost, composite-based heatsinks, heat spreaders, and packaging are a promising solution to allow further improvements in devices' power capabilities[68,69]. Currently available composites, however, have too low of thermal conductivity because randomly-mixed filler particles do not form efficient continuous heat transport pathways[68,70]. Methods to align filler particles are under investigation[68,71–73], especially during 3D printing, and acoustic assembly introduces a way to not only align but also compact filler particles together to form highly conductive networks. The enhancement of thermal conductivity in 3D printed composites using acoustics is investigated in Section 3.2.

Increasing conductivity at lower particle loading by improving the particle contact network efficiency allows improvement of other functional properties simultaneously. As mentioned above, to reach high conductivity, high filler loading is typically required, which makes composites prohibitively brittle[5,6,71,73–79]. Developing methods to improve conductivity at low loading is in high demand for both flexible electronics and thermal materials (to withstand thermal cycling[68,71,73] and additionally allow processing at low viscosity, e.g. for infill around small electronic components). This opportunity for orthogonal control of multiple functional properties is investigated in Chapter 4. Experiments that isolate the mechanical response of the particle assemblies reveal deformation mechanisms that alter or preserve the functionality of the composite. Further, opportunities to develop novel functionalities by patterning particles which themselves have structure on the nano- or micro-scale are explored. This hierarchical assembly has promising implications for both composite materials and patterned materials where either the particle or matrix phase is sacrificial, i.e. removed to leave a structured single phase (for example by patterning hierarchical porosity for ionic conduction in battery electrodes).

Before investigating the properties of acoustically patterned composites, however, a

theoretical framework for the physics behind acoustic patterning must be established. In Section 2, the theoretical understanding of the acoustic forces on particles in pressure fields (and torques, on non-spherical particles) is reviewed. Development of models is undertaken to map out the range of structures possible in patterned composites, on both the meso- and micro-scale (i.e. the shape of patterns as well as the particle arrangement within them). Improvements to the computational efficiency of these models is a main theme of this section, to develop methods for probing structure when thousands of particles interact within pressure fields, complete with scattering off of each particle. More complex particle shapes require more complex models that can handle fewer particles, but these nonetheless give valuable insights into the acoustic control over micro- and meso-structure. To this end, both molecular-dynamics-style models and finite element models are used and validated against experimental observations.

In each chapter, a detailed motivation description and literature review will be given to contextualize this work within the state of the art. The final chapter will cover promising directions for future work.

1.4 Permissions and Attributions

1. The content of Section 2.1 is the result of a collaboration with Kieth Johnson, Brian Giera, Erika Fong, Maxim Shusteff, Julie Mancini, John Karnes, Corie Cobb, Christopher Spadaccini, Daniel Gianola, and Matthew Begley, and has previously appeared in *Materials & Design*[34]. It is reproduced here with the permission of Elsevier: `http://doi.org/10.1016/j.matdes.2021.109512`.

2. The content of Section 2.2 and 3.2 is the result of a collaboration with Amir Tahmasebipour, Xin Liu, Julie Mancini, Bryan Moran, Brian Giera, Ishan Joshipura, Maxim Shusteff, Carl Meinhart, Corie Cobb, Christopher Spadaccini, Daniel Gianola,

and Matthew Begley.

3. The content of Section 3.1 and 4.1 is the result of a collaboration with Rachel Collino, Tyler Ray, Neil Dolinski, Leanne Friedrich, Daniel Gianola, and Matthew Begley, and has previously appeared in *Advanced Materials Technologies* [28]. It is reproduced here with the permission of Wiley: `http://doi.org/10.1002/admt.201900586`.

4. The content of Section 4 is the result of a collaboration with Daniel Strickland, Hyo Lyn Hor, Carloz Ortiz, Daeyeon Lee, and Daniel Gianola, and has previously appeared in *Physical Review E* [80]. It is reproduced here with the permission of APS: `http://doi.org/10.1103/PhysRevE.102.032605`.

5. The content of Section 4.3 is the result of a collaboration with Matthew Wong, Michael Haggmark, Daniel Myers, Srinivas Grandrothula, Mattanjah de Vries, Daniel Gianola, Matthew Begley, Tal Margalith, James Speck, Steven DenBaars, and Shuji Nakamura and has previously appeared in *Light-Emitting Devices, Materials, and Applications XXV* [81]. It is reproduced here with the permission of ISOP: `http://doi.org/10.1117/12.2581801`.

Chapter 2

The theory of acoustic patterning

This chapter introduces the theory of acoustic manipulation of particles during processing of composite materials. The first section (Section 2.1) starts with the numerically simplest case, spherical particles in standing waves, and builds up models of many interacting particles to map out the design space of acoustically patterned materials. The following sections investigate rod- and flake-like particles, which have desirable properties in composite materials applications but which require more advanced modeling. The experimental validation in the following section was performed by Keith Johnson, and portions of the work here was published in *Materials & Design*[34]. The finite element modeling framework described in Section 2.3 was developed in collaboration with Amir Tahmasebipour and Prof. Carl Meinhart.

2.1 Acoustic patterning of spheres

2.1.1 Introduction

In order to optimize acoustic patterning of composites for functional material applications, a systematic understanding of how to control focused particle pattern morphology

and microstructure must be attained. While recent experimental studies on functional materials made with acoustic focusing have investigated the role of basic ink properties (i.e. filler loading and rheology) in determining material properties[28,41,51,82,83], relationships between these and other important processing parameters (acoustic, material, and device parameters) and the structural features of particle patterns are still not well understood, much less the corresponding changes in functional performance. Elucidating these relationships will provide a better understanding of how to control pattern geometry and functional material properties for better incorporation into materials design and processing. While mapping this design space experimentally with meso- and micro-structural characterization would be an expensive and time-consuming process, in recent years the understanding of acoustic forces has advanced to the point that simulations are well suited to the task of efficiently mapping this space, as well as providing additional insight into the material architecture and microstructure.

The acoustic forces on particles arise from a transfer of momentum from the pressure and velocity fields of the surrounding fluid to the particle surface. The pressure field itself can be treated as the sum of perturbations including the induced background field (e.g. the incoming waves constituting a standing wave), the field scattered off the particle surface, and the field scattered off of other nearby particles. The physics of this problem is encapsulated in the acoustic wave equation, which for the simplest case of an isolated, incompressible sphere was shown as early as 1934[84] to give rise to a simple sinusoidal force (in a standing wave). The solutions to this problem have been refined since then for compressible spheres, notably by Gorkov[85], and for viscous fluid media. These developments have been succinctly summarized by Bruus[86], culminating in relatively simple analytical expressions for the acoustic radiation force on spheres (which will be demonstrated in this section to be highly accurate to the most complete models available, as well as to experimental observations).

These solutions to the wave equation become more complex when multiple particles are present, because the scattered pressure fields off their surfaces interact with other particles. Since this work targets the structural features of acoustically patterned composites, which pack many interacting particles in close proximity, these interparticle interactions are critical to capture accurately, but become computationally costly. Models for these forces have seen much progress in recent years, elucidating details of the forces on interacting solid particles in arbitrary applied pressure fields in viscous media[60,87–89]. Solving for these forces, however, involves a multipole expansion solution of the acoustic wave equation with many interacting scattered field perturbations, a computationally expensive procedure not appropriate for simulation of large systems of contacting particles over many timesteps, since it scales with the cube of the number of particles (on the order of hours per timestep for more than 100 particles, when simulations may have millions of timesteps)[87].

As a result, instead of thoroughly treating the solutions to the wave equation, this section employs closed-form approximations of the solutions for acoustic and hydrodynamic forces to enable many iterations on simulations of relatively large systems of interacting particles in a comparatively short time ($\sim$10 hours for 10^7 timesteps with $\sim$1000 particles). By using the appropriate assumptions, the error introduced in these approximations is kept low in the relevant regimes. To investigate the structure that these forces assemble in dense systems of particles, we incorporate these closed-form approximations into a molecular dynamics framework to track both the assembly dynamics and steady-state particle structures under a wide variety of parameter configurations, and extract the dependence of morphological features of the particle assemblies on the input processing parameters. We validate this model with measurements from experiments and find excellent agreement in mesostructural feature descriptors.

In this study, analysis of acoustically assembled structures begins with mesoscopic features like focused line width, height, and profile. We find that these features have clear

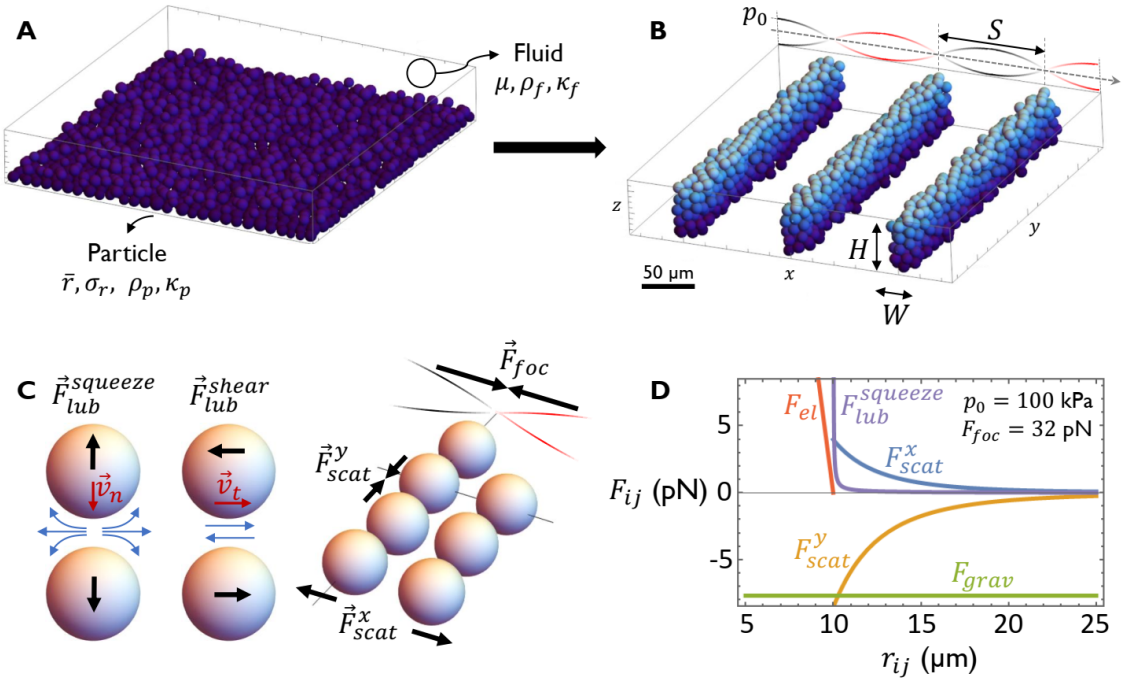

Figure 2.1: A schematic of the simulation parameters. **A** The initial conditions of the simulation and input parameters. **B** With the application of a standing pressure wave with amplitude p_0, particles are focused to the low-pressure nodes into lines with spacing S, width W, and height H. Particles are colored by their z position for clarity. **C** Illustrations of the interparticle lubrication and scattering forces, along with the focusing body force. **D** Plot of the radial interparticle forces versus particle separation, along with the magnitudes of the focusing force F_{foc} and gravitational force F_{grav}, for an example configuration with a particle pair at $\overline{x} = S/4$ from the origin (aligned either along the x or y axes) and with diameters $d_i = d_j = 10$ μm, pressure amplitude $p_0 = 100$ kPa, constant particle approach velocity $\mathbf{v}_n^{ij} = 1$ μm/s, and a very soft $K_{el} = 10^{-5}$ N/m (to illustrate the form of the elastic normal force).

dependence on ink properties, assembly parameters (like focusing wavelength and pressure amplitude), and channel geometry, and we provide maps of these features to guide future experimental studies. Next, we investigate the microscopic features of particle structures, including the local volume fraction, geometry of the void space, and particle contact network anisotropy. Although these microstructural features are not as sensitive to input parameters as the mesoscopic structure is at steady state (and thus can be less readily modulated during materials processing) we find that they have favorable properties for

a variety of transport functionalities by nature of the assembly process which targets anisotropic, packed structures. Finally, we discuss focusing dynamics, and find that acoustic assembly time scales are amenable to integration into materials fabrication processes like 3D printing and roll-to-roll processing. We systematically span the operating space of acoustic focusing for processing architected materials by performing molecular dynamics simulations on systems of $N > 300$ particles. These simulations advance particle positions in time according to Newton's equations of motion, starting with initial configurations corresponding to either dispersed or settled suspensions, and utilizing accurate closed-form models of acoustic and hydrodynamic particle interactions. Ultimately, this process provides particle trajectories which we analyze to elucidate dynamic and steady-state behavior of the particle assemblies formed by acoustic focusing.

2.1.2 Simulation Framework

The simulation code was written in Wolfram Research Inc. *Mathematica* 12 and compiled in *C*, with particle positions saved to file for analysis. The simulations are contained within a box with hard (elastic) boundary conditions on all faces, as illustrated in Figure 2.1A. The box size is chosen to be large enough to avoid size effects, but small enough for fast computation. This is confirmed by doubling the system size in the y direction, which produces no measurable effect on the properties studied (line width, volume fraction, or kinetic energy). Changing the system size in the x (focusing) or z (settling) directions has important consequences discussed below, though edge effects in x are also observed to be negligible, allowing generalization of the periodic focused structure to larger systems in x or y (with more pressure nodes or longer focused lines).

The simulation is initialized with particles in a fluid at a volume fraction ϕ. Particles are on the micron scale and the system is athermal (i.e. not subject to Brownian motion).

Symbol	Description	Default value
L_x	Channel width in focusing direction	300 µm
$\overline{d}$	Mean particle diameter	10 µm
d_i	Diameter of particle with index $i \in [1, N]$	10 µm
σ_r	Diameter standard deviation	0.1 µm
ρ_p	Particle density	2500 kg/m^3
κ_p	Particle compressibility	(36.7 GPa)$^{-1}$
ρ_f	Fluid density	1000 kg/m^3
κ_f	Fluid compressibility	(2.2 GPa)$^{-1}$
μ	Fluid viscosity	0.89 mPa s
δt	Timestep	100 ns
λ	Acoustic wavelength	600 µm
ϕ	Particle:fluid volume fraction	10%
p_0	Pressure amplitude	300 kPa

Table 2.1: Input parameters.

The particles have diameter of mean $\overline{d}$ and standard deviation σ_r (polydispersity is generated as a Gaussian distribution), and unless otherwise mentioned the materials are silica spheres in water (for facile comparison to experiment), with particle density and compressibility ρ_p and κ_p, and fluid density, compressibility, and viscosity ρ_f, κ_f, and μ (values tabulated in Table 2.1). Note that these properties for water are very similar to those of inviscid, rapid-curing photopolymers commonly used in 3D printing, such as hexanediol diacrylate, and while these are the main focus of this study, other particle and (Newtonian) fluid materials produce similar structures but different dynamics, as detailed below. The initial configuration of particles are of two types: in the first, particles are placed randomly throughout the simulation box and given a small random velocity, corresponding to uniform dispersion of particles; in the second, an initialization period is allowed during which particles settle to the channel floor via gravity.

2.1.3 Forces on interacting spheres

Particles are subject to gravitational forces (F_{grav}) in the z direction (denoted $\hat{\mathbf{z}}$), Stokes' drag (F_{drag}), hydrodynamic particle interactions (F_{lub}), and linear elastic interactions (F_{el}) between particles, as detailed below. When the applied pressure field is turned on, particles are also subject to the acoustic focusing force (primary radiation force) F_{foc}, which is a translational body force, and a short-range interparticle interaction F_{scat}, which is a result of incoming pressure waves scattering off of particle surfaces, all detailed below. The total force on a particle with index i at a given timestep is

$$\mathbf{F}^i_{tot} = \mathbf{F}^i_{drag} + \mathbf{F}^i_{grav} + \mathbf{F}^i_{foc} + \sum_{j \neq i}^{N} \left(\mathbf{F}^{ij}_{lub} + \mathbf{F}^{ij}_{el} + \mathbf{F}^{ij}_{scat} \right),$$

where body forces are denoted by i and interparticle forces due to particle j by ij. Each particle's position is advanced in time via Verlet integration: $\mathbf{r}^i_{t+\delta t} = \mathbf{r}^i_t + \mathbf{v}_i \delta t + (\delta t)^2 \mathbf{F}^i_{tot}/m_i$, where $m_i = \frac{1}{6}\pi d_i^3 \rho_p$ is the particle mass, d_i is the diameter, δt is the timestep duration (typically 100 ns), and $\mathbf{v}_i = (\mathbf{r}^i_t - \mathbf{r}^i_{t-\delta t})/\delta t$ is the instantaneous velocity[90].

The first body force included here is the drag force:

$$\mathbf{F}^i_{drag} = -3\pi\mu d_i \mathbf{v}_i, \tag{2.1}$$

Stokes' formulation for low Reynolds' number, which slows all particle motion. This force opposes a particle's velocity, and scales with the particle size and with the viscosity of the fluid.

Next is the gravitational force:

$$\mathbf{F}^i_{grav} = -m_i g(1 - \rho_f/\rho_p)\hat{\mathbf{z}}, \tag{2.2}$$

where $g = 9.8$ m/s^2 is the gravitational acceleration. This is a constant body force on particles acting in the $-\hat{\mathbf{z}}$ direction, and incorporates the buoyancy force.

The focusing force is the final body force included, which acts on particles when a standing pressure wave is induced in the fluid. For a standing wave with n low-pressure nodes spanning the length L_x of the box in the x direction, the wavelength is $\lambda = 2L_x/n$ and the wave number is $k = 2\pi/\lambda$, as illustrated in Figure 2.1B. The focusing force is:

$$\mathbf{F}^i_{foc} = -f_0 \sin(2kx_i)\hat{\mathbf{x}}, \tag{2.3}$$

$$f_0 = \frac{\pi\kappa_f \Phi m_i}{2\lambda} p_0^2, \qquad \Phi = \frac{5\rho_p - 2\rho_f}{2\rho_p + \rho_f} - \frac{\kappa_p}{\kappa_f}, \tag{2.4}$$

where x_i is the x-component of the particle position $\mathbf{r}_i = x_i\hat{\mathbf{x}} + y_i\hat{\mathbf{y}} + z_i\hat{\mathbf{z}}$. The focusing force reflects the sinusoidal shape of the standing pressure wave (illustrated in Figure 2.1B,C) induced by exciting the channel at a resonant frequency of the system. This force pushes particles to the nearest low-pressure node in the standing wave, and has force magnitude f_0 which scales with the square of the pressure wave amplitude p_0, the volume (mass) of the particle, and the contrast Φ in density and compressibility between the particle material and fluid. The form of the focusing force used here is King's formula, a highly accurate closed-form expression which closely approximates the full multipole expansion solution of the acoustic wave equation, with $< 5\%$ error even when multiple interacting particles are present (for small particles, $k\overline{d} < 0.15$) [84,87].

Interparticle forces arise from hydrodynamic interactions as illustrated in Figure 2.1C, which are dominated by squeeze and shear lubrication forces, $\mathbf{F}^{ij}_{lub} = \mathbf{F}^{ij}_{lub,squeeze} + \mathbf{F}^{ij}_{lub,shear}$. These forces are written in terms of the normalized clearance distance between particle surfaces $\epsilon_{ij} = (2r_{ij} - d_i - d_j)/d_i$ where $r_{ij} = ||\mathbf{r}_j - \mathbf{r}_i||$ is the distance between particle

centers:

$$\mathbf{F}^{ij}_{lub,squeeze}(\epsilon_{ij} > \epsilon_0) = 3\pi\mu d_i \mathbf{v}_n^{ij} \left(\frac{a_{ij}^2}{1+a_{ij}^2} \left[\frac{1}{\epsilon_{ij}} - \frac{1}{3} \right] - \frac{a_{ij}(1+7a_{ij}+a_{ij}^2)}{5(1+a_{ij})^3} \ln \frac{\epsilon_{ij}}{3} \right), \quad (2.5)$$

$$\mathbf{F}^{ij}_{lub,shear}(\epsilon_{ij} > \epsilon_0) = -3\pi\mu d_i \mathbf{v}_t^{ij} \, \frac{4a_{ij}(2+a_{ij}+2a_{ij}^2)}{15(1+a_{ij})^3} \ln \frac{\epsilon_{ij}}{3}, \quad (2.6)$$

where $\mathbf{v}_n^{ij}$ is the normal component of the velocity between particles i and j (negative for approaching particles), $\mathbf{v}_t^{ij} = \mathbf{v}_j - \mathbf{v}_i - \mathbf{v}_n^{ij}$ is the transverse component, $a_{ij} = d_j/d_i$ is the relative size of each particle, and $\epsilon_0 = 0.001$ (one thousandth of a radius) is the particle roughness. These forces oppose motion when particles approach one another, scaling with particle size and viscosity similarly to the drag force, and additionally with the particle approach speed. The magnitude of these forces depends critically on the distance between particles, as plotted in Figure 2.1D, with a singularity as the gap between surfaces closes (i.e. $\epsilon_{ij} \to 0$ or $r_{ij} \to [d_i + d_j]/2$). The force is truncated when particle roughness asperities come into contact, if a boundary layer does not prevent contact first, at a clearance of $\epsilon_{ij} \leq \epsilon_0$ [91]. Since they are significant only when particles are approaching one another relatively rapidly, the primary effect of these forces is to slow down particles initially approaching the particle aggregate at the low-pressure node.

These lubrication forces take analytical forms demonstrated to match well with fully resolved fluid simulations, with $< 5\%$ error for $\epsilon_{ij} < 1$ [91,92] (and the forces vanish for $\epsilon_{ij} > 1$, or $r_{ij} > 20$ µm as plotted in Figure 2.1D), allowing rapid and accurate calculation of interactions between a large number of particles. These forces can be superimposed for arbitrary particle arrangements because of the linearity of the Stokes' equations [91]. Here, a very slight scaling of the force tail ensures that it decays to zero at an interaction cutoff of $r_{ij} = 2.5\overline{d}$ to ensure smooth behavior in the case of anomalous velocities (not

observed here);[91] this is the only difference from the classic solution by Cooley[92]. Since a small boundary layer is present between particle surfaces as a result of the squeeze lubrication force, friction and rotation of particles are assumed to have negligible influence (in experiment, this behavior can be enforced via surface chemistry)[28].

Particles also have a linear elastic normal force when they overlap with walls or other particles:

$$\mathbf{F}_{el}^{ij}(\epsilon_{ij} \leq \epsilon_0) = K_{el}\epsilon_{ij}\hat{\mathbf{r}}_{ij}, \tag{2.7}$$

with a stiffness coefficient $K_{el} = 1$ N/m, which is relatively soft in physical terms for numerical efficiency, but still several orders of magnitude stronger than the other forces in the system. For comparison, Figure 2.1D is plotted with a very soft $K_{el} = 10^{-5}$ N/m to illustrate the form of the force. The behavior of granular flows on this scale has been shown to be insensitive to this value, since the hydrodynamic interactions prevent particle interpenetration or rebound after collisions (because momentum is quickly lost to the fluid)—in other words, the elastic normal force only comes into effect when the particles are nearly stationary with respect to one another[91,93].

Finally, the acoustic scattering force is a short-range interparticle force that arises from the incident pressure waves scattering off of nearby particles[88,89,94,95]. Since the waves are traveling in the x direction, the scattering force depends on the location $\overline{x} = \frac{x_i+x_j}{2}$ and orientation $\cos\alpha = (x_j - x_i)/r_{ij}$ of a particle pair with respect to the focusing axis, though it is independent of the orientation in the y-z plane, $\tan\gamma = (z_j - z_i)/(y_j - y_i)$.

This force is:

$$\mathbf{F}_{scat}^{ij} = -\frac{f_0\lambda}{\pi\Phi}\left(\frac{d_i+d_j}{4}\right)^3 \times \left(\frac{(\rho_p/\rho_f-1)^2}{2}\frac{\cos^2(k\overline{x})}{r_{ij}^4}\left[\left(\frac{3}{2}\cos^2\alpha-1\right)\hat{\mathbf{r}}_{ij}-\left(\cos^2(\alpha+\pi/4)-\frac{1}{2}\right)\hat{\mathbf{t}}_{ij}\right] - \frac{k^2(\kappa_p/\kappa_f-1)^2}{3}\frac{\sin^2(k\overline{x})}{r_{ij}^2}\hat{\mathbf{r}}_{ij}\right). \quad (2.8)$$

The dominant term in the scattering force is the strong, short-range r_{ij}^{-4} radial ($\hat{\mathbf{r}}_{ij}$) repulsion, which is largest for particles aligned along the x direction ($\alpha = 0, \pi$) and zero when particles are aligned along the y axis ($\alpha = \pi/2$). The force also has a strong tangential ($\hat{\mathbf{t}}_{ij} = -\sin\alpha\ \hat{\mathbf{x}} + \cos\gamma\cos\alpha\ \hat{\mathbf{y}} + \sin\gamma\cos\alpha\ \hat{\mathbf{z}}$) component, which is maximum at off-axis angles ($\alpha = \pi/4$) and pushes particles away from the x axis. There is a weaker (r_{ij}^{-2}) attractive term which is independent of particle orientation, so that the force is attractive for particles aligned along the y or z axes, but repulsive for particles aligned in x. The r_{ij} dependence of this force is illustrated in Figure 2.1 for particles aligned along x ($\alpha = 0$) and along y or z ($\alpha = \pi/2$). An plot of the angle and separation dependence is also shown in Figure 2.2A-B. The magnitude of this force again scales with particle volume, pressure amplitude, and material properties, similarly to the focusing force.

The form of the scattering force used here is adapted from an established analytical approximation[89,94–96] which has small error from the full open-form multipole expansion solution of the wave equation (for the range of particle sizes studied here, $k\overline{d} < 0.15$), allowing for fast computation of interactions among many particles. Simulation of ∼1000 particles for 10^7 time steps takes approximately ten hours on a single 2.3 GHz CPU core. By comparison, using the multipole expansion method (with enough terms to converge to 1% error) the computation time of a single time step of three spheres takes 30 seconds, and ten spheres takes one hour[87]. Our approximation is based on the far-field solution

for small particles, and assumes single scattering, symmetry arguments, and only uses the dipole expansion terms. It has been demonstrated that the scattering interactions can be well-approximated by such pairwise forces even in systems of many particles, since the interaction of other particles' scattered fields makes a negligible contribution to the force[97]. The expression used here has been slightly modified from Weiser's form[94,95] to incorporate the tangential component of the force via an empirical fit to the full multipole solution reported in Sepehrirahnama et al.[87]. A comparison between the full expansion and our model is shown in Figure 2.2.

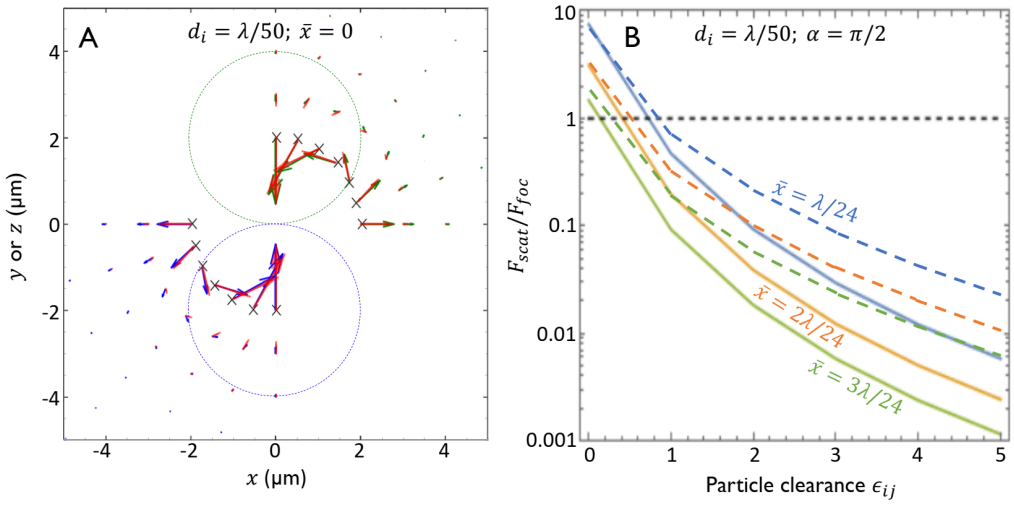

Figure 2.2: **A** A comparison of the analytical scattering force $\mathbf{F}_{scat}$ used in this work (red vectors) to the full potential multipole expansion presented in Sepehrirahnama et al. 2015 (blue and green vectors)[87], with $\lambda = 200$ μm for two spheres with $d_i = 4$ μm centered on the endpoints of the vectors, with $\overline{x} = 0$ (i.e. at the low pressure node). The circles are drawn oriented at $\alpha = \pi/2$ and in contact, $\epsilon_{ij} = 0$. The underlying (blue and green) vectors are reproduced from Sepehrirahnama et al. 2015[87] with the permission of the Acoustical Society of America. **B** The analytical scattering force magnitudes (solid lines) compared to the multipole expansion solution (dashed lines)[87], plotted versus clearance distance normalized by particle radius for various particle pair locations relative to the low-pressure node, $\overline{x}$, with particles aligned in the transverse (y or z) direction, $\alpha = \pi/2$.

Despite the assumptions underlying the form of our force formulation, the error in our closed-form scattering forces compared to the multipole solution (expanded to several

terms beyond the dipole) is negligible for contacting particles at the low-pressure node (for any orientation, Figure 2.2A, and particle size within $k\overline{d} < 0.15$), where it is a dominant force in the system. Further from the node, however, the error approaches ∼20%, though there the scattering force decays relative to the other forces in the system, Figure 2.2B (see also Figure 2.1 for comparison to other forces). The error also increases somewhat for large particle separations, but since the scattering force decays quickly and the highly accurate King's formula dominates for $r_{ij} \gtrsim 1.5\overline{d}$, this error does not appreciably impact particle interaction behavior in dense systems. As a result, these force approximations accurately model the dominant forces in the dense systems of contacting particles investigated here, though the full expansion is more appropriate for modeling systems with few particles where more accurate particle trajectories and equilibrium positions are important. The hydrodynamic interactions among particles in dense, compacted systems dampen or obscure the effects of the scattering interactions, so that the structure and behavior of these systems is not sensitive to small inaccuracies in these forces. Finally, viscous streaming due to induced fluid motion is not included in this model, since large particles (>5 µm) are dominated by the focusing force[48] in the range of pressure amplitudes studied here.

2.1.4 Experimental Validation

Our model was validated by comparing the width of experimentally focused lines of particles to the simulated cases with the same materials, channel geometry, volume fraction, nominal particle size, and pressure amplitude. All of these parameters are straightforward to control experimentally except for the pressure amplitude, which scales with the square of the voltage applied to the piezo but has significant variability due to fluctuations in acoustic losses in the system between trials[98]. As such, p_0 must be measured in each

experimental trial in order to compare the results to the corresponding simulations.

For these experiments, silica particles (Corpuscular, 10-25 µm diameter) were dispersed in water using a vortexer, and fed into glass microchannels. The channels were constructed from borosilicate capillaries with 0.3 × 3 mm rectangular cavity cross section (Borotubing Vitrotubes) cut to 15 mm and attached to metal ferrules (0.25 mm^2 cross-section, McMaster) with polyolefin heat-shrink and Epoxy (5-min, Devcon) and loaded with syringes via plastic tubing (TYGON, 0.04" ID). The channels were superglued to piezoelectric transducers (2 mm thick PZT26, Steminc SMPL20W15T21R111). The piezos were fixed to the side of the channel so that the actuation direction was oriented parallel to the focusing direction in the channel[28,99,100]. The piezos were soldered to BNC connectors and driven with a signal generator, power supply and amplifier (Fluke 294, Tenma 72-7245, Minicircuits LZY-22+) and monitored in parallel with an oscilloscope (Agilent). A 3.3 MHz signal was used and the voltage range was 10-40 V. Particle volume fraction was limited to 5v%

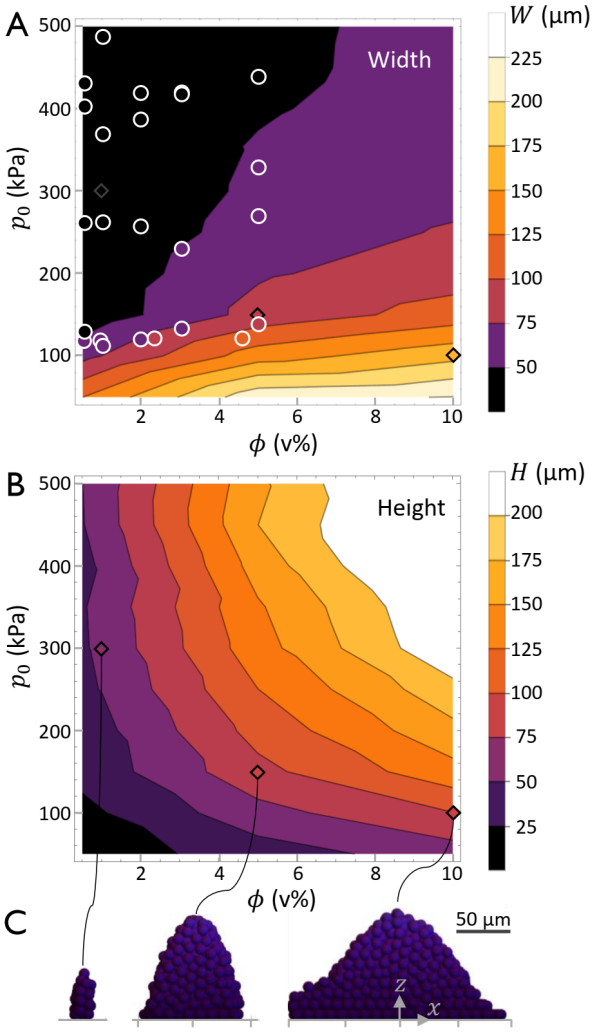

Figure 2.3: The **A** width and **B** height of focused lines at various particle loading ϕ and pressure amplitude p_0 values, for 10.0 ± 0.1 µm diameter SiO_2 particles in water, with 300 µm channel height, pre-settled ICs, and $S = \lambda/2 = 200$ µm line spacing. Experimental points are circle markers colored by their measured line width values, tabulated in Table 2.2. **C** Profiles of the simulated focused lines (black diamonds in A-B).

because of difficulty in accurately and reliably measuring line width at higher loading. The piezo was held at ambient temperature by a water-cooled copper heatsink.

The pressure amplitude was determined by recording videos of the focusing process with a Point Grey Grasshopper 3 camera attached to a Nikon Eclipse TI-U microscope. Using *Tracker Video Analysis and Modeling Tool*, samples of four isolated particles were tracked and the trajectories were fitted to

$$x(t) = \frac{1}{k}\arctan\left(\tan[kx(0)]\exp\left[\frac{\Phi}{9\eta}(k\bar{d})^2 E_{ac} t\right]\right),$$

a solution of the balance of King's acoustic force and drag, to extract the acoustic energy density E_{ac}[98]. The pressure amplitude was then calculated as $p_0 = 2\sqrt{\rho_f c_f^2 E_{ac}}$ where $c_f = 1480$ m/s is the speed of sound in water. The line width was measured at steady state at four to six representative points along lines in each trial. Four to five trials were conducted at each combination of volume fraction and voltage, and these trials were averaged to give the points shown in Figure 2.3A colored by their measured width value, for comparison to the simulated results (shown as a contour map, as detailed in the next section below). For a visual comparison, see Figure 2.6D-F. A list of these values with error estimates is also given in Table 2.2 and a plot of all individual trials is given in Figure 2.9. These experimentally measured values match the simulated cases closely, validating the accuracy of our analytical model. Since the width of the focused lines is sensitive to the focusing and scattering forces, this close match allows us to assert that our model accurately describes these forces, and thus also the morphology and microstructure of the simulated assembled structures.

In the following sections we first discuss the extent of control that can be achieved over the geometry of focused lines, and then we investigate the microscopic details of the particle packing within focused structures. The mesoscopic geometry of the particle

patterns can be controlled to match processing targets and scale material properties, and while the microstructure is less sensitive to changes in the input parameters, we find it has favorable properties for the performance of functional patterned materials.

2.1.5 Mesostructural Analysis

Metrics

The width W gives the width of a focused line of particles excluding the outermost 5% of particles. The width is plotted for various particle loading values (volume fractions) ϕ and pressure amplitudes p_0 in Figure 2.3A, and for various channel heights and initial conditions in Figure 2.4C. W is calculated using the standard deviation of the particle x center coordinates (two standard deviations on each side of the center of a line plus $\overline{d}$) to differentiate cases where lines overlap slightly. The x coordinates of particles are approximately normally distributed in almost all cases ($p_0 \gtrsim 100$ kPa or $\phi \lesssim 8\%$), so that this measure excludes any outliers and gives the width of the innermost 95% of particles, closely matching the boundaries of the lines. For the widest lines where these boundaries are not well defined, W exceeds the line spacing. In these cases, higher W values indicate more overlap of lines (closer to uniform distribution of particles). The height $H = \max(z_i)$ of the lines includes all particles, since because of gravity there are very few outliers in the z coordinates. The length of the lines in the y direction is equal to the channel length, L_y, in all cases studied here.

Results

As illustrated in Figure 2.3, the width of focused lines increases with volume fraction ϕ, as is expected as the number of particles in the system grows. As pressure amplitude increases, i.e. as stronger focusing forces are induced, the lines are compressed so that

W decreases and H increases. There is relatively weak dependence on p_0 above 200 kPa where the vertical components of interparticle forces outcompete gravity more strongly. Additionally, as shown in the contour plots spanning a wider range of W, Figure 2.10, the focusing wavelength controls the line spacing $S = \lambda/2 = L_x/n$ (measured center-to-center) and scales directly with the line width, resulting in width limits of $\overline{d} < W < S$ at any given wavelength.

Though p_0 and ϕ are the primary means of controlling line geometry, initial conditions also play an important role. As shown in Figure 2.4, if particles are initially suspended and dispersed when focusing is turned on (dashed lines), the particles are focused to the center of the channel faster than they can settle (at moderate to high pressure amplitudes, >400 kPa; see Figure 2.7 for a discussion on time scales), so that they are stacked in a vertical line against gravity (low W, H reaching the top of the channel). This corresponds to cases where ink is delivered to the focusing chamber and focused immediately, or active mixing methods are used to keep particles suspended, or when the density mismatch between particles and fluid is very low. When the particles have been allowed to initially settle, however (solid lines), the focusing forces must lift particles off the channel floor as the particle lines are compressed together by the focusing force. As a result, the particles do not reach the top of the channel (except in 50 µm or shorter channels) and the lines are significantly wider. Because the competition between the focusing forces and gravity plays a larger role in determining structure compared to the dispersed initial conditions, the line width and height are also much more sensitive to changes in pressure amplitude.

Line width and height are relatively insensitive to particle size and polydispersity. W increases about one diameter over the range of $\overline{d}$ studied (e.g. from $W \approx 15$ µm for $\overline{d} = 2$ µm to $W \approx 25$ µm for $\overline{d} = 15$ µm at a fixed $S = 42$ µm, corresponding trivially to the increase in $\overline{d}$), and has negligible changes between polydispersity of $\sigma_r = 0.01\overline{d}$ and $\sigma_r = 0.1\overline{d}$. Focusing rates, on the other hand, are sensitive to particle size, as discussed

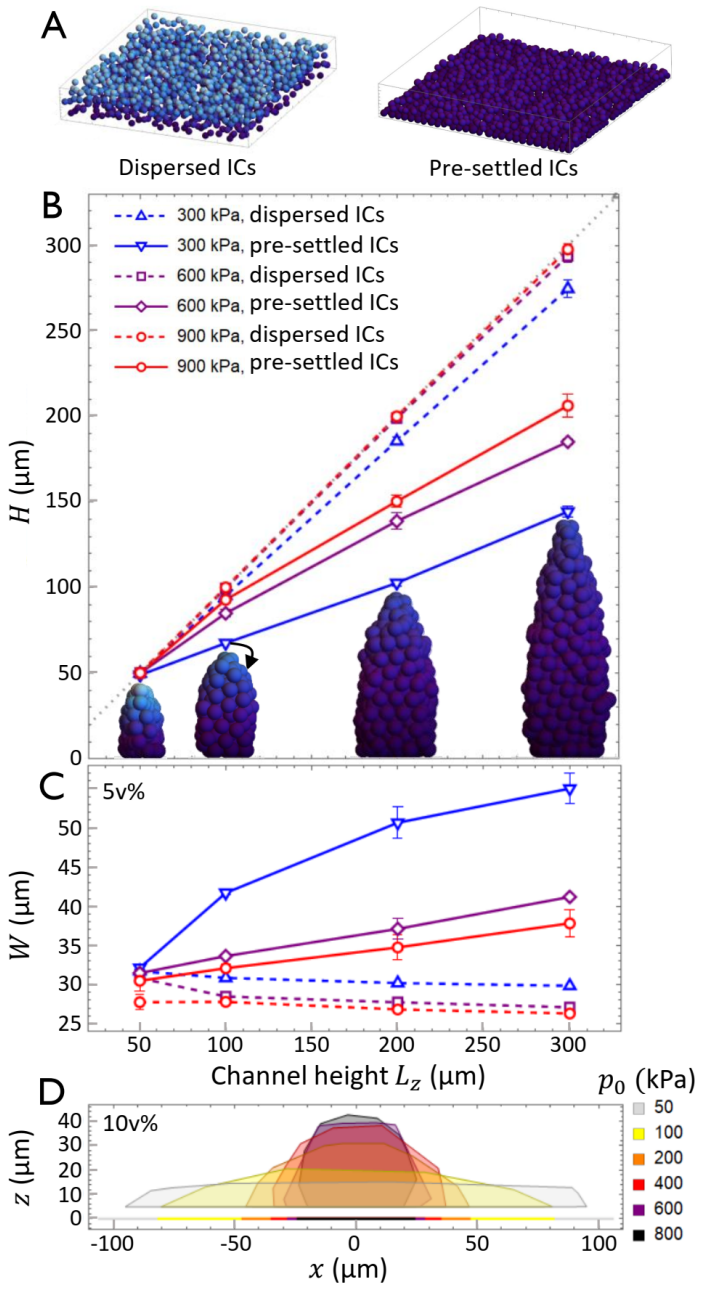

Figure 2.4: **A** Dispersed and settled initial conditions ($L_z = 50$ µm). The **B** height and **C** width of focused lines versus L_z, with snapshots of line profiles (for the pre-settled 300 kPa case) approximately scaled to the axes, for 10.0 ± 0.1 µm diameter SiO_2 particles in water at 5v% with $S = 200$ µm. **D** Line profiles (convex hulls around particle centers), with line width plotted as horizontal bars, for dispersed ICs at 10v% and $L_z = 50$ µm.

below. If focusing is turned off after steady state has been reached, the lines collapse and spread out relatively slowly, e.g. width increases roughly linearly at a rate of 7 µm/s for 10 µm spheres at 10v% in a 50 µm high box (see Figure 2.8).

Discussion

We find that the line width can span the entire range from a single particle diameter to the line spacing (i.e. from a single particle wide to overlapping). The spacing S itself is an easily controlled parameter via the focusing wavelength (piezo frequency). The lower limit for line spacing is $S \gtrsim 10\overline{d}$ (or $k\overline{d} \ll 1$, the Rayleigh limit required by the force model)[60], although it is possible to manipulate particles in a less ordered way outside this limit[60]. The upper limits are less well understood—continual improvements in acoustic coupling and device design push the attainable acoustic amplitudes higher, allowing focusing in larger channels with wider spacing, but some intrinsic limitation at large wavelengths or energy densities (e.g. from damping[101], viscous streaming[100,102], or even piezo heating) may enforce a hard limit. Experiments with ∼10 µm particles have reported patterns of multiple uniform lines with $100 \lesssim S < 750$ µm[28]. We note that no significant change in mesostructure due to rapid photopolymer curing is observed in experiment, but that this may be system-dependent[28,41,51].

These results outline morphological limits and guide materials engineers to the input parameters needed to meet processing targets for functional materials. For example, to assemble patterns with a desired line spacing and width, which must have given height (e.g. within a certain layer thickness for stereolithography or roll-to-roll processing), these parameter maps will give outlines of the particle loading and channel geometry needed to achieve those patterns. Then, for a given device geometry and ink composition, pressure amplitude and wavelength can be modulated to access the ranges of W and H presented here.

Furthermore, acoustic control of particle pattern morphology has strong ramifications for tuning functional properties in materials. For example, the electrical conductivity of lines of conductive particles in an insulating matrix material scales directly with the cross-sectional area of the lines, as does capacity to absorb species into the particles themselves. In these applications, maximizing W and H within the bounds allowed by the process would yield optimal performance. On the other hand, ionic transport through an electrolyte medium surrounding particles scales with the spacing between lines, and diffusion times into the particle structures themselves scale with cross-sectional area (as does material cost). In applications where there are trade-offs between multiple of these properties, e.g. in battery electrodes, optimization of the assembled line geometry may allow significant performance gains. As an example, while raw electrical conductivity scales with W and H, there are significant diminishing returns beyond the percolation threshold (marked in Figure 2.10 for various wavelengths), and mechanical performance is compromised as volume fraction increases. In experiment, controlling line spacing and width with acoustic assembly parameters in order to pattern highly efficient networks resulted in high conductivity at very low volume fractions and preserved mechanical properties, in addition to providing control over network anisotropy [28]. For any given application, the understanding given here of how geometrical properties scale allows better design of processes and improvements on material performance.

2.1.6 Microstructural Analysis

We next investigate how the acoustic focusing process influences the microscopic features of particle packing and local structure within assembled lines. We investigate measures of local packing density, void shape, and contact network anisotropy, all of which influence transport properties.

Metrics

The local volume fraction ϕ_l is calculated by dividing each particle's volume by the volume of its Voronoi cell (calculated with radical weight by particle diameter—tesselation shown in Figure 2.5A). The outermost particles are excluded when they have Voronoi cells that detect the sides or top of the simulation box (as opposed to other particles) and thus have an ill-defined local volume fraction. This results in a roughly normal distribution of local volume fractions, representing the volume within the outermost layer of particles.

The directed mean free path is a measure of the length of the average interstitial void between particles in each coordinate direction. This value is calculated by first dividing a focused line into nine cubes stacked along the center of the line along the y axis. The cubes have side length $2\overline{d}$. In each of these cubes, 100,000 points are selected randomly within the void space, on a grid with spacing of 0.05 µm. (Denser grids with spacing 0.01 µm or more sampled points have negligible change in result.) Each of these points is extended in the positive and negative directions in x, y, and z until both endpoints intersect with a particle, as illustrated in Figure 2.5A. The lengths of the resulting line segments generated at each sampled point are averaged to give the mean free path in the void space in x, y, and z. The points with any segment exceeding $3\overline{d}$ in length, e.g. those that find a gap between particles and protrude outside of the assembly, are discarded ($\sim$3.5% of them met these criteria). Similarly, for each of these points a circle is drawn about each of the three axes and the maximum diameter before the circle intersects a particle is recorded and averaged to give the directed mean free breadth, also shown in Figure 2.5A.

The contact fabric tensor measures anisotropy in the particle configuration. This is

calculated as

$$F_{kl}^{c} = \langle n_k^m n_l^m \rangle \hat{\mathbf{x}}_k \otimes \hat{\mathbf{x}}_l = \frac{1}{M} \sum_{m}^{M} \begin{bmatrix} n_x^m n_x^m & n_x^m n_y^m & n_x^m n_z^m \\ n_y^m n_x^m & n_y^m n_y^m & n_y^m n_z^m \\ n_z^m n_x^m & n_z^m n_y^m & n_z^m n_z^m \end{bmatrix}, \tag{2.9}$$

where n_k^m is the kth component of the unit normal contact vector $\hat{\mathbf{n}}_m = \mathbf{r}_{ij}/r_{ij}$ for contact m (individual contacts are shown in Figure 2.6A) so that values of $n_y^m = 1$ indicate the particle pair is exactly aligned along the y axis. The angled brackets denote averaging over all M particle contacts in the assembly. The diagonal entries of this tensor are the components of the system-averaged contact vector, so that the deviatoric differences of the tensor, $F_{kk}^c - F_{ll}^c$, give a measure of anisotropy in the contact network (where values of zero indicate isotropy). This value is highly correlated with anisotropy in the assembly stiffness[103] and electrical or thermal conductivity[104], and is a routine measure of configuration anisotropy in granular materials studies.

Results

The local volume fraction within a typical focused line is plotted in a heat map in Figure 2.5B. Aside from a significantly dilated region near the outer free surface of the line, there does not appear to be any pattern in the distribution of packing density, consistent with the expectation that the (symmetric) focusing force dominates over other forces, such as gravity, in the determination of the local structure. The mean of the local volume fraction $\overline{\phi}_l$ is plotted in Figure 2.5D over time for mono- and polydisperse suspensions. After focusing is turned on, the volume fraction rises rapidly as particles are focused and packed together at the low pressure node. Within 0.05 seconds, the line reaches the glass transition $\phi_g \approx 0.58$, and from there slowly approaches the random close packing limit $\phi_j \approx 0.64$, reaching a steady state after ∼0.10 seconds (for 800 kPa; see

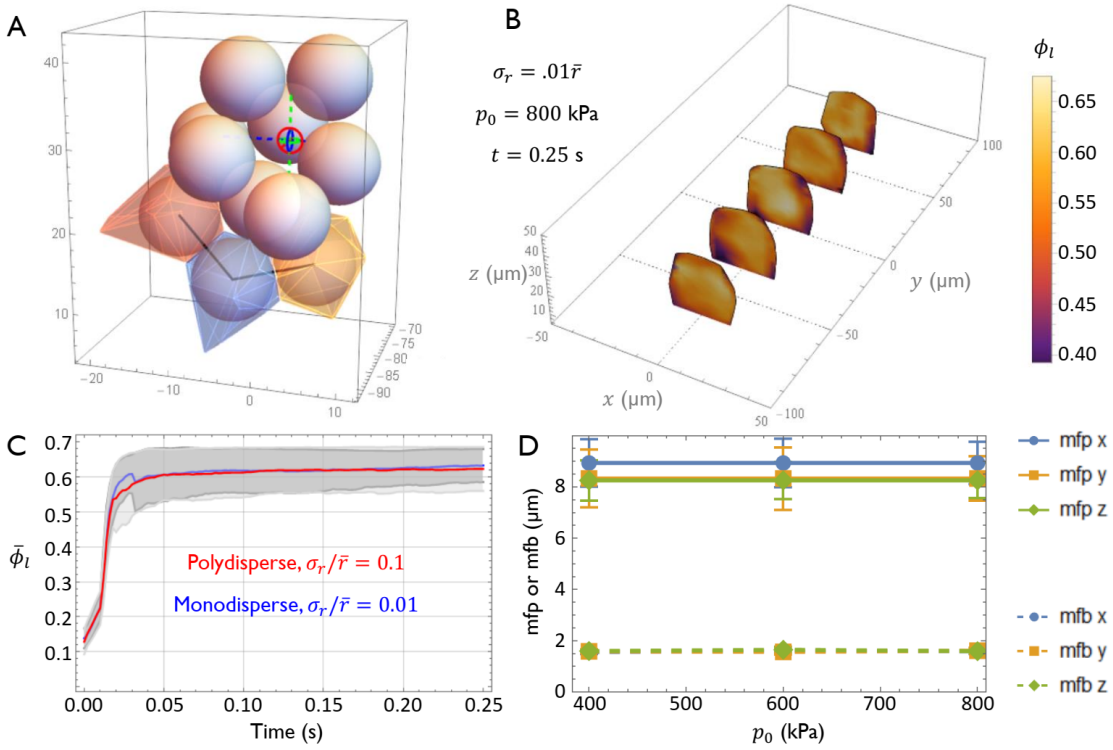

Figure 2.5: **A** Schematic illustrating the Voronoi volume around particles (colored polyhedra), mean free paths around a sampling point (colored lines), and mean free breadths (colored circles) extending from the sampling point to the nearest particle surface. **B** Local volume fraction distribution. **C** Voronoi volume fraction (mean with shaded standard deviation) over time for mono- and poly-disperse particles. All examples are of $p_0 = 800$ kPa and 10v% $10 \pm \sigma_r$ μm particles. **D** Mean free path and mean free breadth (monodisperse).

the dynamics section below for timescales under other conditions). Higher polydispersity cases, $\sigma_r = 0.1\bar{d}$, have slightly lower steady-state packing fraction, ∼0.62. If focusing is turned off after steady state has been reached, the packing fraction decays roughly linearly to $\phi_g \approx 0.58$ in ∼0.45 s, and then decays at a slower rate below ϕ_g as the focused lines spread out (see Figure 2.7 for a detailed picture of time scales). As a result, modulating the focusing force by turning on or off the signal to the piezo (and to a lesser extent, using the appropriate level of polydispersity) allows spanning of the glass transition so that one can control whether the assembled structures are solid- or liquid-like. We note that higher polydispersity values may have a more significant impact on the structure, though

it requires more computational resources to simulate mixtures of large and small particles, which quickly diverge in the range of force magnitudes acting on them (see Figure 2.7B), limiting the scope investigated here.

The mean free paths and breadths are plotted in Figure 2.5D for steady-state lines focused at several pressure amplitudes. These results show insignificant anisotropy in void geometry, as well as insensitivity to pressure amplitude. The mean free path in the x direction may be slightly longer, as would be expected due to the repulsive scattering forces, but is within error bars of the values for the other directions. A random walk in the void space also revealed insignificant anisotropy in effective diffusion coefficient and tortuosity. Although there is appreciable anisotropy in the particle packing (discussed below), it is too subtle to result in significant void shape anisotropy, due to the noisier nature of void shape statistics. For comparison to other studies, spherical particle granular assemblies compressed uniaxially have mean free path only 5% larger in the compression direction than the transverse direction at 60% strain, corroborating the small difference we observe[103]. Another measure of packing anisotropy, however, the anisotropic pair distribution function $g(\mathbf{r}_{ij})$ (a common measure for anisotropic disordered solids)[105] shown in Figure 2.6C, indicates slightly wider spacing between particles along the x direction (shifted and lowered first peak and elevated first local minimum), consistent with the slightly increased x mean free path.

While the anisotropy in void geometry is very subtle, the anisotropy in the arrangement of particles is more easily quantifiable, as shown in Figure 2.6A-B. There is a transient peak in contact fabric anisotropy that occurs while chains of particles are forming in the y direction before complete focusing (see Figure 2.6E-F). Then, as these chains are compacted together, $(F^c_{xx} - F^c_{yy})/\mathrm{Tr}(F)$ decreases and plateaus at a low-moderate value of 0.1, indicating a somewhat higher density of contacts in the y and z direction compared to the focusing (x) direction. This is likely because the short-range scattered acoustic forces

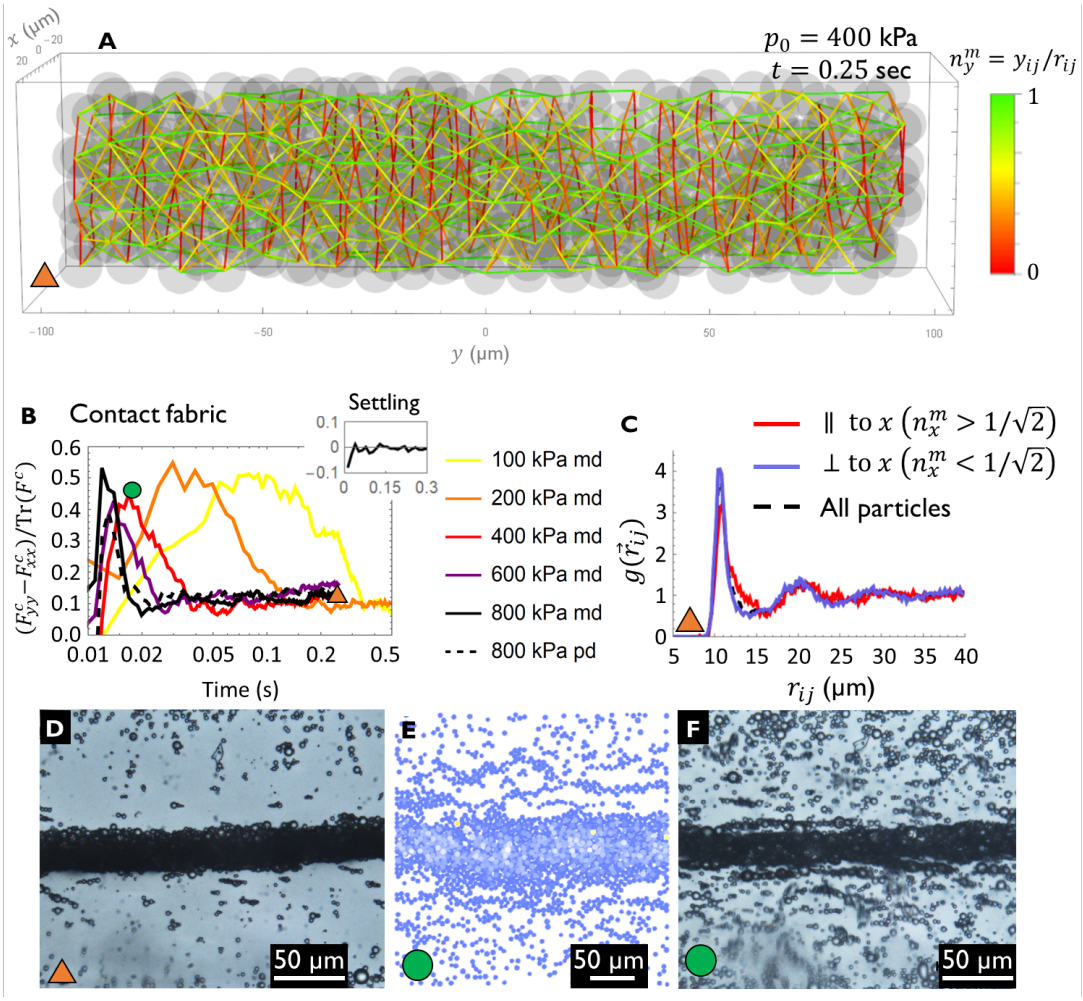

Figure 2.6: **A** A visualization of the contact network of particles, with lines drawn between centers of contacting particles ($r_{ij} \leq 0.51[d_i + d_j]$) and colored by the y component of the normal contact unit vector n_y, i.e. the length of the normalized y component y_{ij} of the separation vector $\mathbf{r}_{ij}$. **B** The normalized deviatoric part of the contact fabric tensor over time. The peak in contact anisotropy occurs before assembly is complete, and is due to the chains of particles forming in the y direction during focusing, **C** The anisotropic pair distribution function for particle pairs aligned parallel (within an angle of $\pi/4$) or perpendicular to the focusing (x) axis. **D** Experimental image of the steady-state particle structure focused at 400 kPa (captured at $\sim$ 0.1 sec after focusing started). **E** Simulated and **F** experimental images of the structure at peak anisotropy ($\sim$0.02 sec) before steady state is reached, marked by a green circle in **B**.

dominate for contacting particles, pushing the particles into alignment along the y and z axes. In granular assemblies compressed uniaxially along the x direction, the deviator plateaus at -0.4 after 20% strain, and reaches a maximum of -0.5 at 10% strain[103]. Note that the sign of the deviator in this uniaxial compression experiment is opposite to our case, as expected because our scattering forces align particles in the transverse directions to the loading (see Figure 2.2).

Particles with a higher aspect ratio of 0.5 (ovoids) were reported to have contact fabric deviator values that approach 1.0 at high strains (60%), mean free path differences of $\sim$15%, and mean free breadth differences of $\sim$5%[103]. This suggests that acoustic focusing of anisotropic particles, as opposed to spheres, could also lead to much higher anisotropy in void shape and contact distribution. Polydispersity does not play a major role in anisotropy (see Figure 2.6B, 800 kPa curves).

Discussion

The microstructural properties discussed in this section play a critical role in determining the functional properties of focused particle structures, and by extension the material properties of patterned composites. For materials engineers designing functional materials patterned using acoustics, the microstructural descriptors reported here (local porosity, anisotropy, etc.) inform modeling of the performance of the materials, e.g. conductivity in battery electrodes. Although the packing fraction, void shape anisotropy, and contact density anisotropy show little change at steady state across the range of pressure amplitudes studied here, and thus cannot be readily modulated in composites cured after the completed focusing process, they have values that are favorable for various transport applications, by virtue of the directional acoustic assembly process which is designed to pattern anisotropic, densely packed structures. This insensitivity to input parameters is likely because the particles are nearly jammed at steady state for the

pressure amplitudes studies here, leaving little excess free volume that would be required for higher packing anisotropy. Though this makes modulation more difficult, it allows relaxation of experimental constraints.

For transport materials where species diffuse through the fluid medium surrounding particles, higher mean free breadth directly correlates with lower tortuosity and higher permeability (i.e. faster transport) [103]. Anisotropy in these values leads to higher anisotropy in transport rates, as well. Higher local volume fraction, on the other hand, directly correlates with absorptive capacity density (e.g. the volumetric capacity of battery electrodes) and generally higher tortuosity and thus slower transport. Since there is a trade-off between those functionalities, tailoring the microstructure anisotropy provides a route to optimize performance. For example, the gradient in packing density we observed near the surface of the focused lines could be beneficial to optimizing transport into the center of the lines while maintaining high capacity. In addition, there is a slight gradient in particle size in the polydisperse cases, with large particles at the center of the line and smaller particles at the surface, because the focusing force scales with particle volume. For $\overline{d} \pm \sigma_r = 10 \pm 1.5$ µm, the only particles on the outermost surface ($|x_i| > 22$ µm) have $d_i < 10$ µm, while the very largest particles $d_i > 14$ µm are at the center ($|x_i| < 10$ µm). Cyclic focusing and structure relaxation steps may further increase the magnitude of this gradient, though we observed no change over 10 cycles. While polydispersity does not significantly affect the mesoscopic geometry of the lines, it can be used to modulate microscopic properties like volume fraction and, though it bears further investigation (especially with anisotropic particles), transport rate gradients. We also note that significant change in microstructure due to rapid photopolymer curing during focusing is not reported in experiment, though detailed characterization has not been undertaken [28,51].

For electrical or thermal transport through the networks of contacting particles (or species transport through etched sacrificial particle voids in a solidified matrix), conduc-

tivity scales strongly with contact density[6,106]. As a result, the high volume fractions approaching the random close packing limit attainable with acoustic focusing enable the high local contact density needed for high conductivity (even at low global ϕ)[28]. We note that conductivity may also arise between particles separated by thin layers of dielectric medium, which may allow sufficient conductivity or break down during application of voltage, and that surface chemistry can be tuned to control these boundary layers and interfacial properties[28,107,108]. Additionally, anisotropy in electrical conductivity is strongly linearly correlated with the contact fabric tensor deviator plotted in Figure 2.6[106]. The anisotropy observed here correlates with higher conductivity along the focused lines (in the y direction) as chains of particles form due to the scattering forces, which may explain the high axial conductivity reported in experiment[28,51]. Higher anisotropy values can also be achieved with anisotropic particles;[28] though modeling the scattering forces on these particles is more difficult, a similar force-fitting method to that presented here or a model of anisotropic particles decomposed into conjoined spheres may provide insight[53].

2.1.7 Dynamics

The time-scales for assembly of suspensions with various particle densities and diameters, fluid viscosities, and applied pressure amplitudes are shown in Figure 2.7. The time for complete assembly increases dramatically for particles with density below 1000 kg/m^3 (that of the fluid), for small particles with diameter $\overline{d} < 10$ µm, and for pressure amplitudes below 100 kPa. It also increases linearly with fluid viscosity. For polydisperse suspensions, the larger particles focus faster and exert higher scattering forces, while the smaller particles focus slower. We note that the structural features of patterns made with higher-density particles or higher-viscosity fluid have similar form to the silica-water system, provided the assembly time and pressure amplitude are scaled to reach the

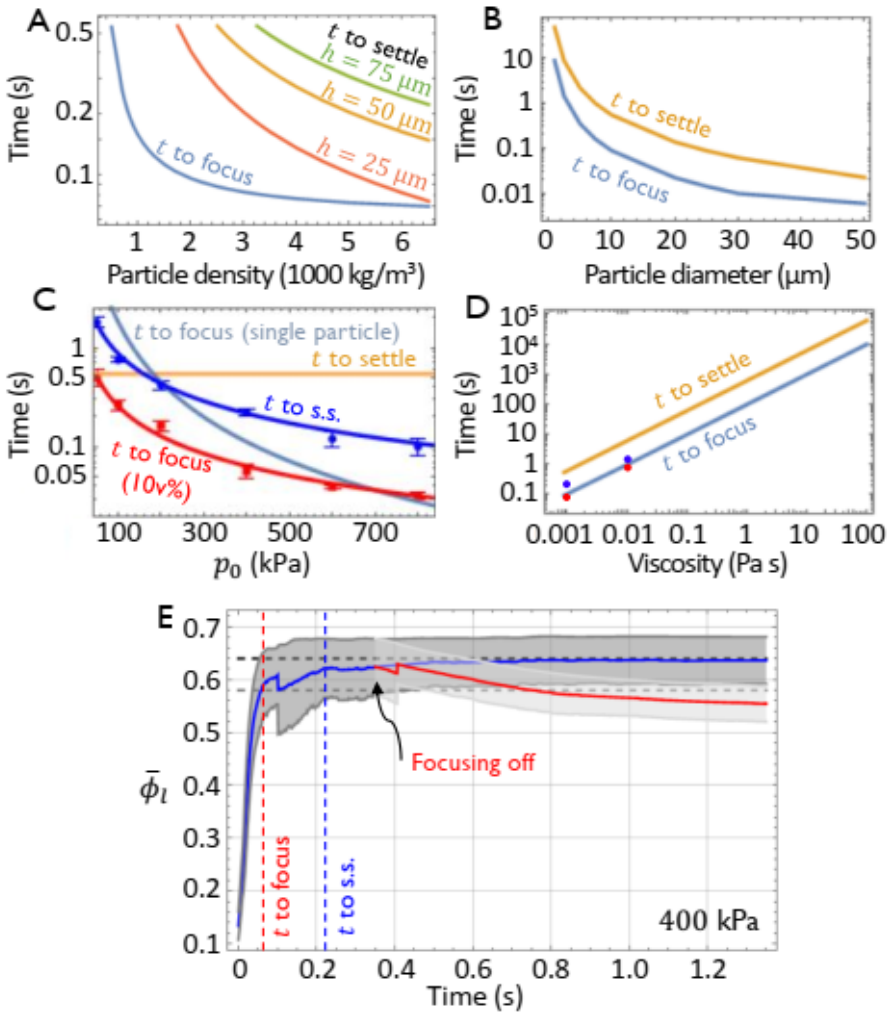

Figure 2.7: **A-D** Dependence of assembly time scales on various parameters. Unless otherwise noted, $\rho_p = 2500$ kg/m^3 and $\mu = .89$ mPa s (silica in water), $L_z = 50$ µm, $S = 200$ µm, the particle diameters are 10.0 ± 0.1 µm, and $p_0 = 400$ kPa. The plotted times to focus are calculations for isolated particles, except in **C** where multi-particle measurements for 10v% are given as fits of the form $t \propto p_0^{-1}$ to two measures of focusing times (as marked in **E** by red and blue dashed lines). **E** Plot of local volume fraction (mean, with shaded bands standard deviation) over time. The red dashed line marks the time to focus (first inflection point in ϕ) and the blue dashed line marks the time to reach steady state in system energy. The solid red curve is the relaxation behavior after focusing is turned off. The random close packing limit is marked at $\phi_j \approx 0.64$ and the glass transition at $\phi_g \approx 0.58$.

close-packed steady state.

The time it takes for the focusing process to be completed can be measured in various ways for dense suspensions of many particles, since after the particles are concentrated near the low-pressure node, a relatively slow particle rearrangement process continues to evolve the structure. Two time scales are shown in Figure 2.7C and E: the first is a "time to focus," which marks the inflection point in $\overline{\phi}_l$ where nearly all particles have reached the aggregate and subsequent evolution is relatively minor and due largely to particle rearrangements. This is defined as the logistic growth characteristic time scale via a fit of $\overline{\phi}_l$ versus time. The second measure is the time to steady state, after which evolution slows even further, measured where the line width, kinetic energy, and average force plateau (as shown in Figure 2.8), though volume fraction continues to evolve slightly after this point, Figure 2.7E. Also plotted in Figure 2.7 is the time it takes a single particle to reach the node (from the edge of the channel), which is approximately bounded by the other two measures (these approach the single-particle solution as $\phi \to 0$). At low pressure amplitudes the multi-particle measures are larger because particles have time to rearrange while migrating to the low pressure node and there is less distance to travel compared to a single particle, whereas at high pressure amplitudes it takes longer because the repulsive scattering forces become stronger and prolong the rearrangement process. We note that the experimental focusing times for 100-500 kPa in water or inviscid photopolymer fall in the range of 0.1-0.5 sec, broadly in agreement with the simulated results.

These acoustic assembly times, with appropriately chosen material properties, allow acoustic focusing to be integrated into materials processing without significantly slowing down the manufacturing process. For example, in projection stereolithography, layer cure times are on the order of one second or longer[109], slower than the patterning process, and in extrusion or roll-to-roll processing of battery electrodes, printing speeds of 500 mm/s are attainable when using a modest ∼5 cm long flow-through acoustic focusing

nozzle[45]. On the other hand, these assembly timescales are not so fast as to prohibit curing before steady state, if that is desired, allowing freezing in of transient properties (e.g. high anisotropy values or looser packing) using rapid light-curing technologies.

2.1.8 Conclusions

Numerical simulations of acoustic focusing of composite materials provide accurate maps of input processing parameters and their effect on both the geometrical features of assembled structures and the details of their particle packing. These results inform process design for producing patterned functional composites, particularly those for transport applications. We demonstrate reliable ability to control line width, spacing, and height using both device properties (particle loading, size, dispersion, channel geometry, etc.) and easily tunable acoustic assembly parameters (pressure amplitude, wavelength, etc.). Microstrucutral properties are less sensitive to input parameters, but show useful characteristics for transport properties through both the particles and medium. Finally, the acoustic assembly dynamics are well-suited for incorporation of acoustic focusing into materials processing techniques like 3D printing, and have strong scaling with both ink properties and acoustic parameters. Future work targeting anisotropic particles, high polydispersity, or microstructural effects of curing is warranted. These results pave the way for incorporation of acoustic focusing into materials processing, which may yield significant property improvements in functional patterned materials.

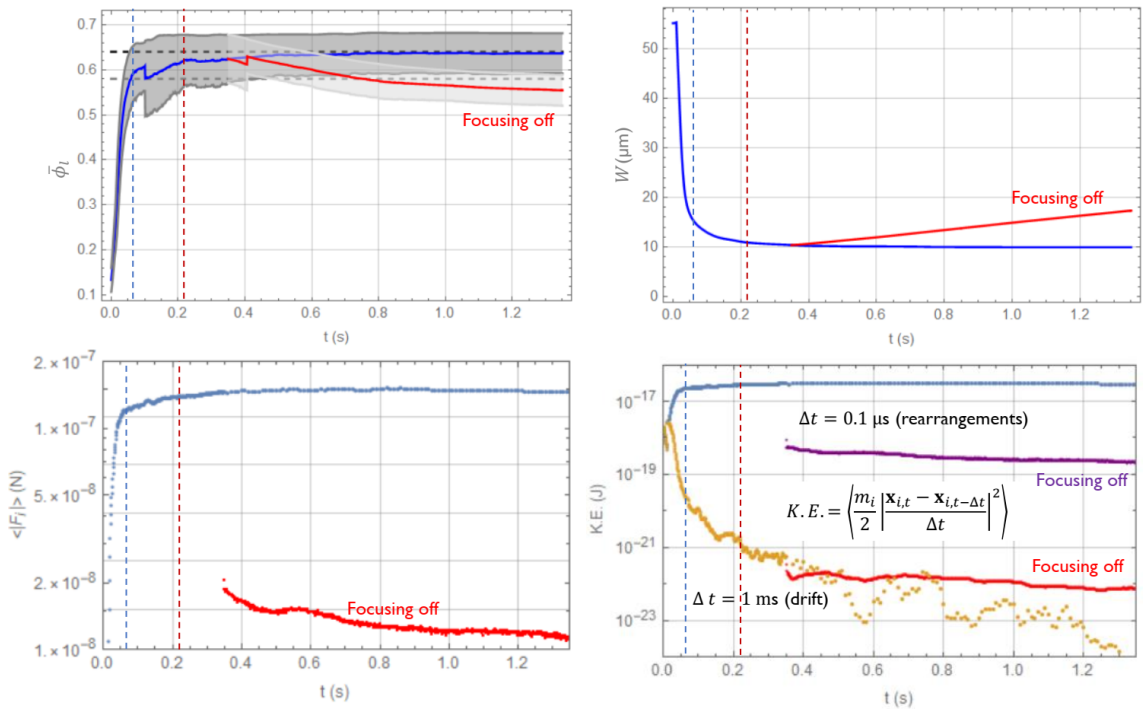

Figure 2.8: Volume fraction $\overline{\phi}_l$, focused line width W, average force on particles, and kinetic energy $K.E.$ (for two displacement timescales Δt, see inset equation) for 10v% 10.0 ± 0.1 μm SiO_2 in water at 400 kPa pressure amplitude. The red (and purple) solid lines are measured when the applied pressure field is turned off at $t = 0.35$ s, and the blue lines are with focusing kept on. The dashed lines mark the timescales for focusing (blue) and steady state (red).

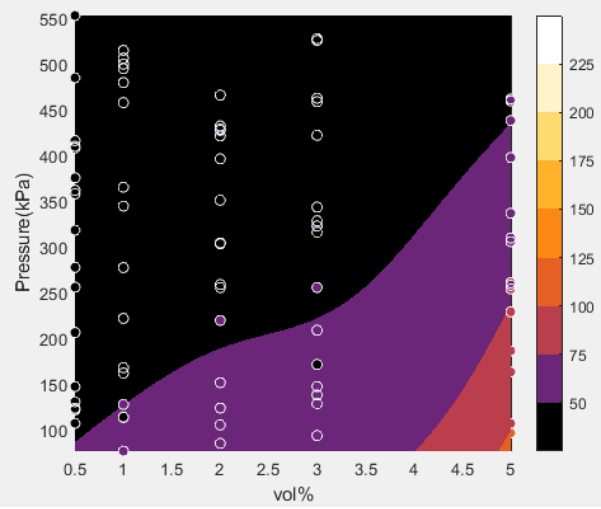

Figure 2.9: All experimental validation trials, with focused line width values in units of μm.

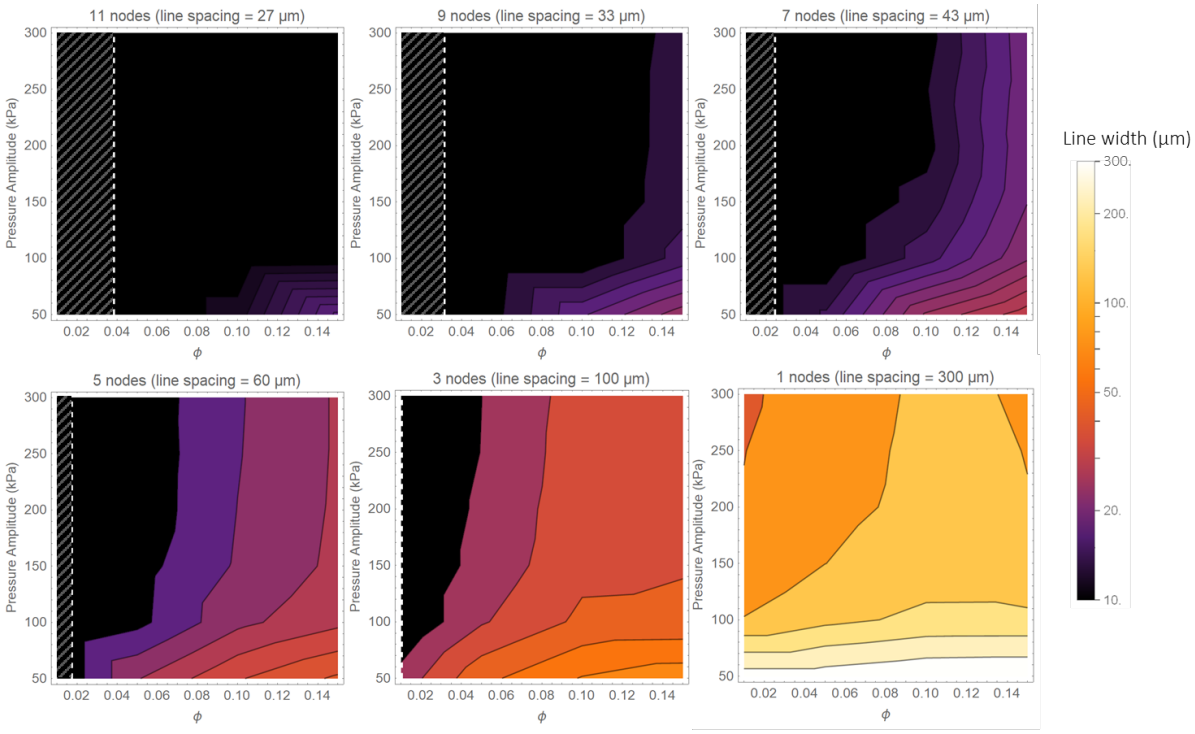

Figure 2.10: The scaling of line width with wavelength (via line spacing), volume fraction, and pressure amplitude, for 10 ± 0.1 SiO_2 spheres in water (50 μm high channel). The white dashed line is the theoretical minimum volume fraction for sphere percolation along the focused lines, so that the shaded region has discontinuous (e.g. electrically insulating) focused lines.

2.2 Acoustic forces and torques on rods and flakes

While the simplicity of forces on spheres in standing waves allows extensive modeling of the microstructural consequences of acoustic forces, in materials applications non-spherical particles are often used, for which analytical models are less straightforward. Rod- and flake-like particles are commonly used in composite materials instead of spheres for their anisotropic properties (e.g. longitudinal stiffness or conductivity). The loss of symmetry from the spherical case adds considerable complexity to solutions for the forces on particles. In addition, acoustic torques are introduced by asymmetric fluxes across the surface of the particle. Although the general scaling of mesostructural features discussed in the previous section for spheres is expected to hold true for non-spherical particles (with minor corrections that scale with the maximum local packing fraction [111] for the given particle geometry), the microstructure will differ with the introduction of this torque, which aligns particles and grants additional asymmetry to the packing. Because the microstructure of patterns with nonspherical particles is less readily simulated (allowing only qualitative inferences from pairwise interactions on a small number of particles instead of simulations of many interacting particles) and because the microstructure of patterned materials is critical to discussions of their properties, the reader will be directed to later sections for discussions of structural ordering and only the construction of the theoretical models will be treated in this section.

As a first approximation, one can model a rod as an assembly of constrained spheres, as will be outlined in this section [53]. Although this model neglects bending of high-aspect ratio particles and the details of scattering off their surfaces, this method gives an efficient estimate of the force and torque on non-spherical particles, including the scattering forces for which analytical expressions are unavailable. These chained-sphere models are used in Section 4.3 to model the rotation of thin rectangular particles around multiple axes,

finding regimes where the torque overcomes gravity.

The force on a rod or flake with center coordinate x_c is calculated using the primary force[84,85] on each sphere as[53]

$$F_{x,ac} = -\sum_{i=1}^{N_l}\sum_{j=1}^{N_w} f_0 \sin\left(2kx_s^{ij}\right),$$

$$x_s^{ij} = x_c + a\left[2i - 1 - N_l\right]\cos\alpha - a\left[2j - 1 - N_w\right]\sin\alpha,$$

where a is the radius of each sphere, α is the orientation of the major axis with respect to the focusing (x) direction, N_l is the number of spheres along the length of the particle, and N_w is the number of spheres along the width (assuming a 2-dimensional rectangular array of spheres). The scattering force is calculated similarly as the summation of interactions between particle pairs (as laid out in the previous section) in each rod, as shown in Figure 2.11A, and the torques by summing the cross products of the moment arm with the total force. Denser packing of spheres in three dimensions can be modeled for example by using the hexagonal close packed arrangement, $\mathbf{x}_s^{ijk}/a = (i + \frac{j+(k \bmod 2)}{2})\hat{\mathbf{x}} + \frac{3j+(k \bmod 2)}{\sqrt{12}}\hat{\mathbf{y}} + k\sqrt{2/3}\,\hat{\mathbf{z}}$ (translated and rotated, if needed). Figure 2.11B illustrates this construction for a mass of focused particles in the low pressure node.

A similar approach, wherein the primary force for a sphere is integrated over the projected area of a rod in the focusing direction, is derived by Yamahira et al.[112]. This model is used to explain the orientational stability of fibers in in Section 3.1, and is compared to experimental observations on long carbon fibers, finding good agreement. The reader is directed to that section for a discussion of the structure created by these forces and torques, because the fiber orientation and resulting structure is integral to the functionality of the materials discussed in that section. Additionally, a comparison of this model and the chained-sphere model is given in the next section (Figure 2.11). Using this projected-area model, the force on rod-like particles F_{rod} pushes particles to

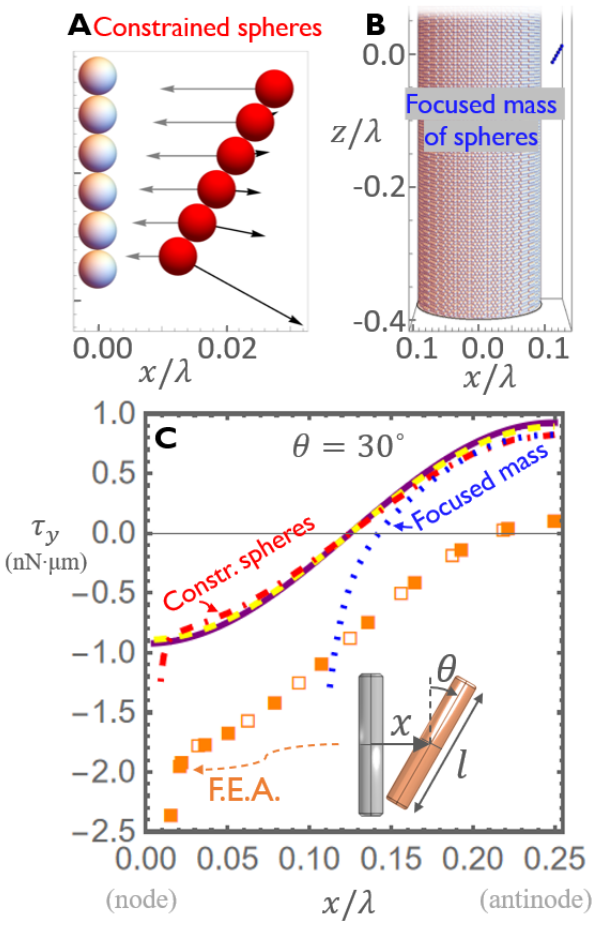

Figure 2.11: **A** Rendering of the constrained-sphere model of a probe rod (colored red) with the primary focusing force on each particle comprising the probe rod drawn as gray arrows and the scattering forces (due to the source rod, gray) as black arrows. The sum of these forces is the total force on the rod. **B** Rendering of a constrained-sphere model with a large mass of spheres at the low-pressure node mimicking a focused line of particles. **C** Comparison of torque calculations on a 3×18 µm boron nitride rod oriented at 30° from the nodal plane at various x positions in a standing pressure wave with wavelength 500 µm. Finite element calculations of the torque on a probe rod (orange in inset) due to the background field and the scattered field due to a source rod (gray) in the low-pressure nodal plane ($x = 0$ and with $\theta = 0$ measured from the z axis) is plotted as orange filled squares. The torque on the isolated probe particle (with no scattering particle) are the empty squares. The constrained sphere model[53] comprising six 3 µm spheres (using the scattering force developed in Section 2.1[34]) is plotted as the red dot-dashed curve (scaled by a factor of 2). Using the same model, the torque with a large mass of scattering particles in the low pressure node (illustrated in B) is plotted as the blue dotted curve. Analytical expressions for rods[112] (projected area method) and spheroids[113] are given as purple and yellow dashed curves, respectively.

the low-pressure nodes, and a torque τ_{rod} aligns them with the y-axis, derived as:[112]

$$F_{rod} = -d^2 E_0 \sin(2kx) \times \\ [(2/3)\Phi |\sin\alpha| \cos^{-1}\alpha \sin(kl\cos\alpha) + \pi k d \Phi_{end} \cos\alpha \cos(kl\cos\alpha)] \quad (2.10)$$

$$\begin{aligned}\tau_{rod} =& (d^2/3k) E_0 \Phi \tan^2\alpha \cos(2kx)[(-kl\cos\alpha)\cos(kl\cos\alpha) + \sin(kl\cos\alpha)] \\ &+ (\pi/2) k l d^3 E_0 \Phi_{end} \sin\alpha |\cos\alpha| \cos(2kx) \sin(kl\cos\alpha)\end{aligned} \quad (2.11)$$

where l is the length of the rod, d is its diameter, $\Phi_{end} \approx 10\Phi/3$ is the factor at the end of the rod, and $E_0 = \kappa_f p_0^2/4$ is the average energy density of the field[112,114,115].

According to this model, fibers longer than a quarter-wavelength ($l > \lambda/4$) are stable in the perpendicular orientation if their initial states are close to perpendicular at an antinode[112], which finds good experimental agreement for long rods (with length $l > \lambda/4$) as discussed in the next section as well as Section 3.1.

2.3 Finite-element calculation of forces on rods and flakes

Although the chained-sphere model discussed in the previous section is useful to calculate forces on long, isolated rods or flakes in a pressure field, it loses accuracy for short rods and when rods come into close proximity with each other. The available analytical models, including the chained-sphere model, do not capture particles' flexural modes or the details of interparticle scattering forces on non-spherical particles. To resolve

these details, finite-element models of the acoustic forces and torques on rods and flakes (modeled as disks) are constructed in this section and are compared to the experimentally observed motion of carbon fibers. In addition, these driving forces give context for the packing of carbon fibers and boron nitride flakes in Section 3.2, finding agreement with experimentally observed particle arrangements. The deviation of these numerically modeled forces from analytical expressions based on constrained-sphere models[53], projected area integration[112], and spheroids[113] is shown in Figure 2.11C. Full maps of the force and torque on rods and flakes (and their consequences for structure and properties) are discussed in detail in Section 3.2.

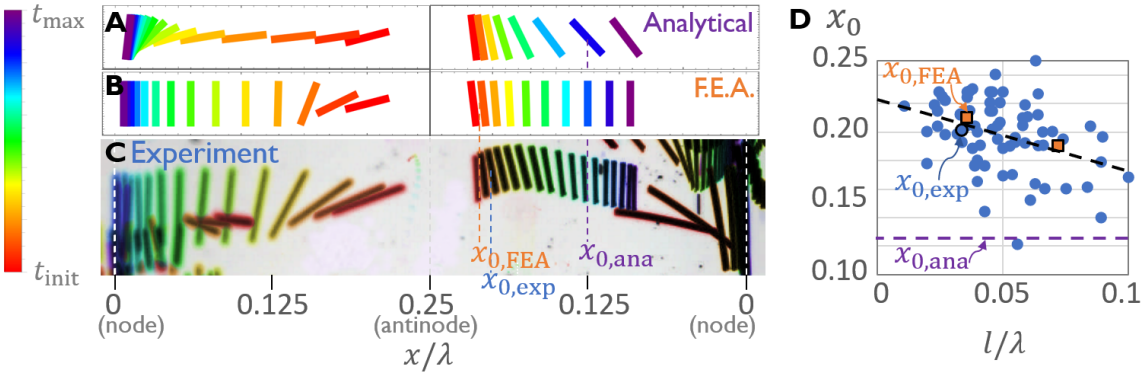

Figure 2.12: **A** Trajectories of fibers according to analytical models (balanced with drag and inertia) with initial positions matched to experimental cases, and **B** trajectories according to the finite element analysis, which better match those observed in experiment. **C** Overlaid video frames of the experimentally focused carbon fibers, colorized by time from red to purple, with the estimated locations x_0 where the torque becomes negative (rotating fibers parallel to the nodal plane). Full image shown in Figure 2.13 **D** Experimentally observed locations x_0 at which fibers begin rotating parallel to the nodal plane (i.e. where the torque changes sign) for various fiber lengths l (blue dots fit with black dashed trendline), as determined from image analysis of videos of focusing of 7 µm diameter carbon fibers in an acrylate photopolymer (with properties very similar to those of boron nitride and water). Finite element calculations are plotted as orange squares, and the analytical prediction as a purple dashed line. The experimental case shown in C is outlined in black (the rod on the left side is not plotted because it immediately begins aligning, so x_0 is not captured).

The main difference between the finite element and analytical models is that the torque

as calculated by finite element analysis serves to align particles along the nodal plane (z direction, i.e. parallel to the focused stripes) unless the particle is very close to the pressure antinode (at $x/\lambda \gtrsim 0.21$), as illustrated in Figure 2.12A. This strong alignment is in agreement with previous finite element simulations on single 2-dimensional rods[116] but in disagreement with the projected area model[112] (plotted as the solid purple line) and spheroids[113] (yellow dashed line) which predict strong counter-alignment (i.e. positive torque, rotating fibers clockwise into alignment along the x axis) instead of negative torque for $0.125 < x/\lambda$, as well as weaker torque for $x/\lambda < 0.125$. This discrepancy is likely due to the inclusion of bending modes of high aspect ratio particles in the finite element analysis method, as well as the inclusion of damping due to scattering from elastic solids in our study.

The constrained sphere model[53], which allows calculation of interparticle scattering effects[34] between rods (plotted as the red dot-dashed line in Figure 2.11C; also shown schematically in Figure 2.11A-B), shows similar short-range scattering to the finite element analysis but dissimilar sign change behavior (at $x/\lambda = 0.125$ instead of 0.22). The sign change in the finite element torque occurs at $x \approx 0.21\lambda$ for rod length 18 µm and at $x \approx 0.19\lambda$ for rod length 36 µm (for $\theta = 30°$). For $\theta = 45°$, the orientation of maximum torque (longest moment arm), the sign change occurs at approximately 0.003λ smaller x for both rod lengths. This does not agree with the analytical expressions, which predicts a sign change at $x = \lambda/8$ for all θ except 0 and 90 degrees, for the reasons discussed above. The sign change in torque at larger x in the finite element model indicates that acoustic patterning more strongly aligns fibers (with higher maximum torque and eariler rotation onset) than previously understood, setting the stage for improving properties via particle alignment and close packing.

To validate these models against experiment, which is important because the torque determines fiber alignment, which is in turn critical for material properties, we experimen-

tally measure fiber rotation behavior to validate the finite element analysis as shown in Figure 2.12C. Fiber trajectories illustrated by the superimposed video frames of carbon fibers in a standing wave in HDDA are compared to modeled trajectories calculated by balancing the numerical forces and torques with drag and inertia, using interpolation functions between calculated values in conjunction with analytical expressions for drag[112]. Rods do not rotate perpendicular to the nodal line at all $\lambda/8 < x < \lambda/4$ as predicted by the analytical models, but instead rotate parallel to the nodal line. To quantify this behavior, a scatter plot of the experimentally observed positions where the torque on fibers changes sign, x_0, is given in Figure 2.12D (blue circles), fitting a linear trend (black dashed line) that coincides with the x_0 predicted by the finite element analysis (orange squares), whereas the analytical models predict $x_0 = \lambda/8$ (purple dashed line). Thus, the experiments validate the finite element analysis but suggest that the analytical models are inaccurate for these short fibers. Additional experimental trajectories are shown in Figure 2.14. The experimental trend and finite element calculations suggest that x_0 approaches 0.125 as fiber length approaches $\lambda/4$, which is the experimentally observed threshold for fiber counter-alignment[28,112,117], suggesting that the analytical models may be more accurate for longer fibers.

One possible reason for this discrepancy is that in some of the experimentally measured cases there are numerous particle aggregated at the low-pressure node, which may cause scattering that affects the rotation of fibers. To account for the effect of scattering off a mass of particles focused at the low-pressure node ($x = 0$), an analytical constrained-sphere model is constructed with the source particle replaced by a hexagonal close-packed cylinder of spheres spanning $-0.1 < x/\lambda < 0.1$ and $-0.4 < x/\lambda < 0.4$ (dotted blue line in Figure 2.11C; illustrated in B). The scattered field off this mass slightly increases x_0 from 0.125 to 0.14 but still predicts strong counter-alignment of fibers (high, positive torque) for $0.14 < x/\lambda < 0.25$, which is not observed in experiment. Thus, scattering does not

cause the discrepancy in x_0 between the analytical models and experiment. Though the finite element analysis accurately captures the behavior of fibers, further theoretical work is needed to better describe the torque on short rods with analytical expressions (which are more numerically efficient than finite element analysis) that match the experiments. Finite element simulations of scattering off a mass of particles are also needed to determine whether the scattering forces due to each particle can be pairwise added (as asserted by recent studies on small numbers of particles[118]) or if the interactions produce nonlinear effects.

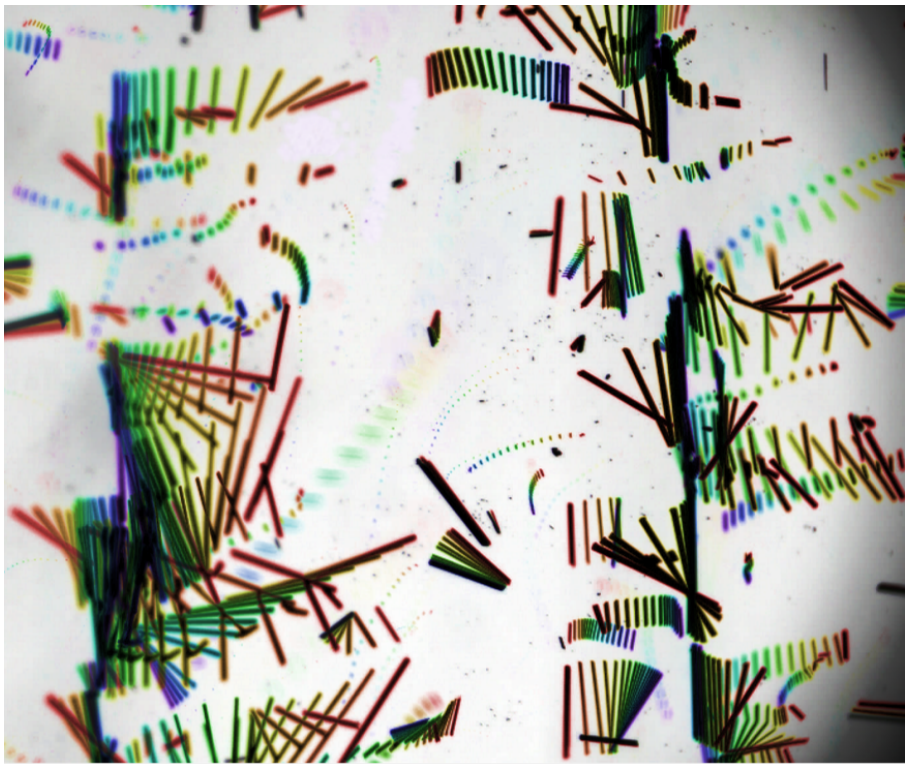

Figure 2.13: The full experimental trajectories of carbon fibers used in Figure 2.12.

2.3.1 Governing Equations

To calculate the acoustic forces and torques on particles with arbitrary shapes using the finite element method, we begin with the governing equations in the fluid. The acoustic

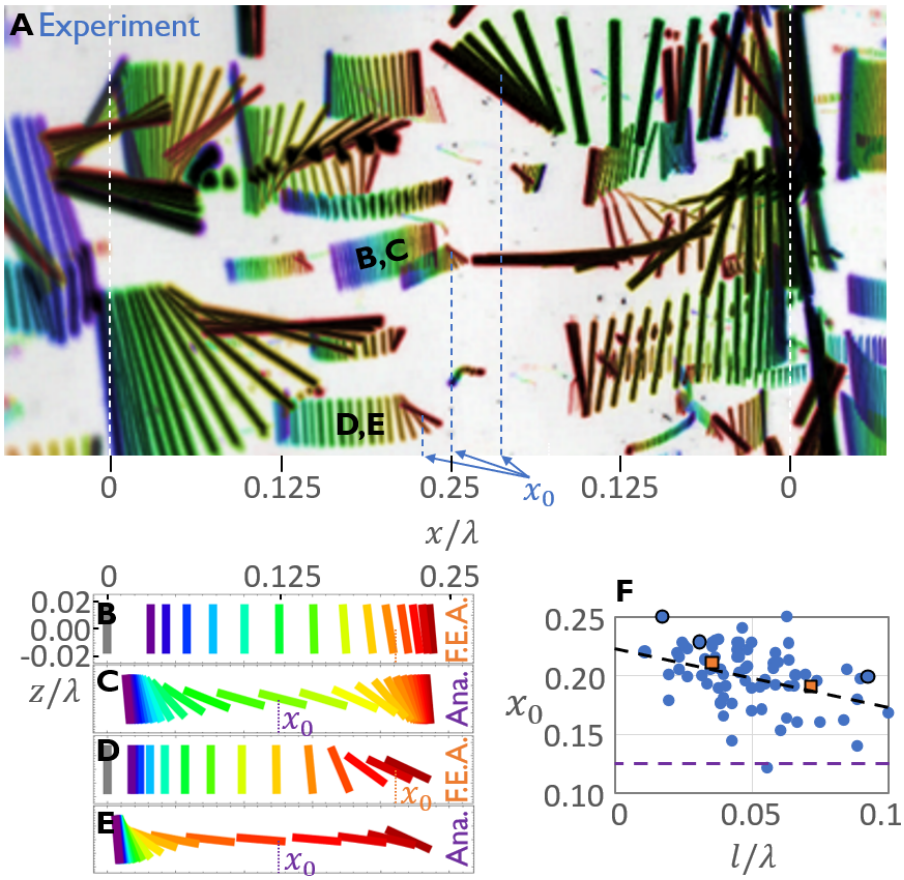

Figure 2.14: **A** A larger image of experimental rod trajectories, compared to trajectories predicted by finite element analysis (**B,D**) and analytical models (**C,E**). The zero-point in torque x_0 illustrated in A are outlined in black in **F**, along with the finite element predictions (orange squares) and the analytical prediction (purple dashed line).

radiation force stems from the non-linear nature of the Navier-Stokes equation which governs the physics of fluids.[119] Generation, propagation and scattering of standing acoustic fields are simulated using a perturbation expansion of the continuity and Navier-Stokes equations,[44]

$$\boldsymbol{\nabla}^2 p + \frac{\omega^2}{c_{\mathrm{fl}}^2} p = 0,$$

$$\mathbf{v} = -\frac{i}{\omega \rho_{\mathrm{fl}}} \boldsymbol{\nabla} p,$$

where, in a time harmonic field with angular frequency ω, p and $\mathbf{v}$ are the acoustic pressure and velocity fields of a fluid with density ρ_{fl} and speed of sound c_{fl}. Small (relative to the wavelength) suspended solid particles in a fluid scatter the incident acoustic wave as the fluid-solid interaction takes place at the acoustic-structure boundary. Resolving the solid displacement field, $\mathbf{u}$, using the equation of motion in Helmholtz form allows capturing the total acoustic pressure as a combination of background and scattered fields:[120]

$$\rho_{\mathrm{sl}} \omega^2 \mathbf{u} + \boldsymbol{\nabla} \cdot \boldsymbol{\sigma}_{\mathrm{s}} = 0$$

$$\boldsymbol{\sigma}_{\mathrm{s}} = \mathbf{C} : \boldsymbol{\epsilon}.$$

These equations are solved for a linear elastic solid of density ρ_{sl} where the stress $\boldsymbol{\sigma}_{\mathrm{s}}$ and strain $\boldsymbol{\epsilon} = \frac{1}{2}\left[\nabla \mathbf{u} + (\nabla \mathbf{u})^T\right]$ fields are related through the elasticity tensor $\mathbf{C}$. Boundary conditions at the fluid-solid interface define acoustic-structure interactions that produce the scattered fields around the particle. This coupling is modeled by balancing the solid acceleration with the fluid pressure as boundary load to the solid domain,

$$\boldsymbol{\sigma}_{\mathrm{s}} \cdot \hat{\mathbf{n}} = -p$$

$$\frac{\boldsymbol{\nabla} p}{\rho_{\mathrm{fl}}} \cdot \hat{\mathbf{n}} = -\omega^2 \ \mathbf{u} \cdot \hat{\mathbf{n}},$$

where $\hat{\mathbf{n}}$ is the unit vector normal to the solid boundary.

2.3.2 Time-averaged fields and attenuation factors

The analytical calculations of time-averaged acoustic radiation forces and torques, although very efficient, are bound by simple particle geometries and background pressure fields.[113,121,122] These calculations often miss the necessary flexural vibrations that are especially important when working with high aspect ratio particles.[117] By developing numerical simulations of the acoustic scattering from a solid body, we may calculate the acoustic radiation force, $\mathbf{F}$ and torque, $\boldsymbol{\tau}$ on a particle of arbitrary geometry in any pressure field.[117] This is done by integrating the time-averaged total pressure and momentum flux on the particle surface $\partial\Omega$,[44]

$$\mathbf{F} = -\int_{\partial\Omega} \mathrm{d}A \left[\left(\frac{\kappa_{\mathrm{fl}}}{2} \langle p^2 \rangle - \frac{\rho_{\mathrm{fl}}}{2} \langle \mathbf{v}^2 \rangle \right) \hat{\mathbf{n}} + \rho_{\mathrm{fl}} \langle (\hat{\mathbf{n}} \cdot \mathbf{v}) \mathbf{v} \rangle \right],$$

$$\boldsymbol{\tau} = -\int_{\partial\Omega} \mathrm{d}A \left\{ \mathbf{r} \times \left[\left(\frac{\kappa_{\mathrm{fl}}}{2} \langle p^2 \rangle - \frac{\rho_{\mathrm{fl}}}{2} \langle \mathbf{v}^2 \rangle \right) \hat{\mathbf{n}} + \rho_{\mathrm{fl}} \langle (\hat{\mathbf{n}} \cdot \mathbf{v}) \mathbf{v} \rangle \right] \right\},$$

where κ_{fl} is the fluid compressibility and the time averaged squared first order total acoustic pressure and velocity are denoted by $\langle p^2 \rangle$ and $\langle \mathbf{v}^2 \rangle$, respectively.

Damping of acoustic waves in a viscous fluid plays an important role on acoustic amplitudes and propagation. To calculate attenuation factors and efficiently damp the acoustic fluid domain, we use a method inspired by Hahn et al. 2015[101] implemented as

$$c_{\mathrm{fl}} = c_0 \ (1 \ + \ i \frac{\varphi_{\mathrm{fl}}}{2}),$$

where the frequency dependent total acoustofluidic loss factor φ_{fl} is $\varphi_{\mathrm{fl}} = \varphi_\eta + \varphi_\delta$, where

the viscous loss factors in the bulk, φ_η, and in the boundary layer ($\delta = \sqrt{2\eta_{\mathrm{fl}}/\rho_{\mathrm{fl}}\omega}$) at the particle surface, φ_δ, for a fluid with dynamic viscosity η_{fl}, and bulk viscosity γ_{fl}, are calculated as

$$\varphi_\eta = \frac{\omega}{\rho_{\mathrm{fl}}\ c_0^2}\ \left(\frac{4}{3}\ \eta_{\mathrm{fl}} + \gamma_{\mathrm{fl}}\right),$$

$$\varphi_\delta = \frac{\rho_{\mathrm{fl}}\ \delta}{4\ E_{\mathrm{st}}^{\mathrm{fl}}}\ \int_{\partial\Omega} \mathrm{d}A \xi_i \xi_i^*,$$

where $E_{\mathrm{st}}^{\mathrm{fl}} = \frac{1}{2}\int_V \mathrm{d}V \kappa_{\mathrm{fl}} \langle p^2 \rangle$ is the stored energy in the bulk of fluid and $\xi_i = v_i - \ \dot{u}_i$ is the relative velocity of fluid and solid domain at the interface.

2.3.3 Numerical Implementation

We solve the damped governing equations subject to boundary conditions presented above using the finite element solver COMSOL Multiphysics 5.6® ("COMSOL Multiphysics Modeling Software," U. S. A.). Calculating the pressure and displacement fields in the relevant domains on a three dimensional grid made up of second order elements with more than 10^6 degrees of freedom. Grid independence was established using a series of simulations similar to Tahmasebipour et al. 2020.[123]. The non-spherical particles are placed within a 3D background standing wave field to produce acoustic scattering and facilitate the calculation of radiation force and torque. The outer boundaries of fluid are Perfectly Matched Layers, avoiding any unwanted reflections back into the acoustic domain. With this method we capture the acoustic radiation from any incident pressure field on any number of particles regardless of position, geometry and material properties, including the interparticle interactions that arise from scattered fields and boundary layers.

Results using this model for rods and flakes are discussed in Section 3.2 and compared to experimental observations. The parameters used in that section are $c_0 = 1497$ m/s,

acoustic energy density $E_{ac} = 111.56$ Pa, $\eta_{\text{fl}} = 0.00089$ m/s, $\kappa_{\text{fl}} = 4.462 \times 10^{-10}$/Pa, wavelength $\lambda = 500$ µm, $\rho_{\text{fl}} = 1000$ kg/m^3, frequency $f = 3$ MHz, $\kappa_{\text{sl}} = 5.2 \times 10^{-11}$/Pa, $\rho_{\text{sl}} = 2100$ kg/m^3, temperature $T = 298$ K.

The simulated particle trajectories are calculated by numerically solving the equations of motion:

$$mx'' = f_a + f_d,$$

$$I\theta'' = \tau_a + \tau_d,$$

where for rods $m = \rho_{\text{sl}}\pi l(d/2)^2$, $f_d = -\eta_{\text{fl}}(4l|\sin\theta| + 3\pi d|\cos\theta|)x'$, $I = ml^2/12$, and $\tau_d = -\eta_{\text{fl}} l^3\theta'/3$ and for disks $m = \rho_{\text{sl}}\pi d(l/2)^2$, $f_d = -\eta_{\text{fl}}(4d|\cos\theta| + 3\pi d|\sin\theta|)x'$, $I = md^2/16$, and $\tau_d = -\eta_{\text{fl}}\pi d^5\theta'/(4l^2)$.[112] f_a and τ_a are interpolation functions of the FEA calculated forces, and $x'(t = 0) = \theta'(t = 0) = 0, z = 0$.

ϕ (v%)	Voltage (V)	p_0 (kPa)	std dev (kPa)	W (µm)	std dev (µm)
0.5	10	25	15	44	2
0.5	20	264	47	32	3
0.5	30	407	55	22	4
0.5	40	434	83	20	6
1.0	10	108	22	56	6
1.0	20	262	160	39	1
1.0	30	370	91	37	3
1.0	40	489	26	32	1.5
2.0	10	116	28	56	5
2.0	20	259	35	46	6
2.0	30	385	72	47	2
2.0	40	421	17	47	4
3.0	10	133	32	52	7
3.0	20	233	74	57	6
3.0	30	424	118	43	4
3.0	40	421	55	45	5
5.0	10	138	43	94	8
5.0	20	270	47	71	10
5.0	30	328	77	60	5
5.0	40	439	36	50	4
0.2	40	120*	30	38	9
0.5	40	120*	30	56	12
0.9	40	120*	30	50	11
2.3	40	120*	30	92	11
4.6	40	120*	30	102	17

Table 2.2: Experimental measurements of focused line widths. Several averages listed, marked with *, were measured using a channel with lossier acoustic coupling to the piezo to access lower pressure amplitudes. Because this lossier coupling resulted in higher spread in measured pressure amplitudes, these were analyzed using both single particle tracking and an additional light intensity fitting method [110] and averaged across a larger number of trials and across volume fractions to yield a pressure measurement with similarly accurate confidence interval as the rest of the data. Lower voltages in this channel did not yield usable results.

Chapter 3

Anisotropic conductivity in acoustically patterned materials

Acoustic patterning presents a unique opportunity for improving the properties of functional composites. Because it can translate particles and compact them into structures with locally high packing fraction, unlike hydrodynamic or electromagnetic assembly which can generally only rotate particles on useful time scales, the contact density of particles can be improved much more than with other assembly techniques. Heat and electrical transport are two functional properties that take particular advantage of high particle contact density, and the extent to which conductivity can be increased over unpatterned composites will be investigated in this section.

The focus of this section is on investigating how processing parameters (including acoustic assembly parameters, device and 3D printing parameters, and particle geometry) can be leveraged to control the structure of the composites (including the orientation and contact density of particles) and thereby modulate the conductivity of the composite. Since acoustic patterning is amenable to forming anisotropic particle structures, an opportunity is presented to control the directionality of thermal and electrical conduction in the

patterned materials, which can be exploited to optimize transport for the application at hand.

Two 3D printing techniques are targeted in this chapter. The first section (Section 3.1) targets direct ink writing, wherein ink is extruded from a nozzle in continuous paths. In this case, acoustic patterning occurs in the printing nozzle, which is developed in this section but the printing process itself is not undertaken. Other members of Dr. Begley's group have detailed the rheology and printing process necessary for form holding with shear-thinning inks using acoustophoresis[45,55,123–128], and this section targets low-viscosity inks for UV-assisted form-holding[129]. The second section (Section 3.2) implements projection micro-stereolithography, projecting ultraviolet light into a bath of photopolymer to fabricate acoustically patterned materials. The strength of direct-ink writing is that it's scalable over large (1 m) areas, but requires rheology that is both low-viscosity in the nozzle to allow particle transport and viscous enough after extrusion (i.e. shear-thinning) for form-holding. Shear-thinning additives generally interfere with material functionalities (blocking particle contacts or contributing to brittle mechanical behavior). These drawbacks are alleviated in stereolithography, which does not have stringent rheology requirements.

3.1 Electrical conductivity

The driving force to stack and pack particles is particularly promising for electrically conductive composites. To reach high electrical conductivity, conductive filler particles must form continuous networks of contacting particles. Stacking particles and concentrating them into lines with high local packing fraction within polymer composites is exactly the structure needed for high conductivity, effectively forming wires in the material. Conventional, unpatterned composites are very inefficient in this regard because they rely on stochastic contact networks between randomly oriented particles uniformly distributed

throughout the material.

In this section, acoustic processing methods are developed for increasing conductivity and forming electrical networks along different directions in the material. We demonstrate that these efficiently patterned materials have an order of magnitude higher conductivity than the dispersed-fiber composites made with the same ink and are conductive at an order of magnitude lower particle loading. Acoustophoresis patterns filler particles into highly efficient percolated networks which utilize up to 97% of the particles in the composite, whereas the inefficient stochastic networks of conventional dispersed-fiber composites utilize $< 5\%$. These patterned materials have conductivity an order of magnitude higher than conventional composites made with the same ink, reaching 48% the conductivity of bulk silver within the assembled silver-particle networks (at 2.6v% loading).

The ultimate use case is 3D printing components with integrated electrical circuits, which requires modulation of conductivity along different directions during printing (using the same ink, if possible, to reduce printer cost and complexity). This section focuses on modulating these electrical properties, finding that controlling the shape of the applied acoustic fields allows control over the anisotropy of the conductive networks and produces materials which are either 2-D conductive, 1-D conductive, or insulating, all using the same nozzle and ink. Integrating this technique into 3D printing is undertaken in the following section (Section 3.2). In the next chapter, the electrical functionality discussed here is also combined with mechanically flexible materials, allowing use in the particularly promising application of 3D printed flexible conductive composites for wearable electronics and soft robotics.

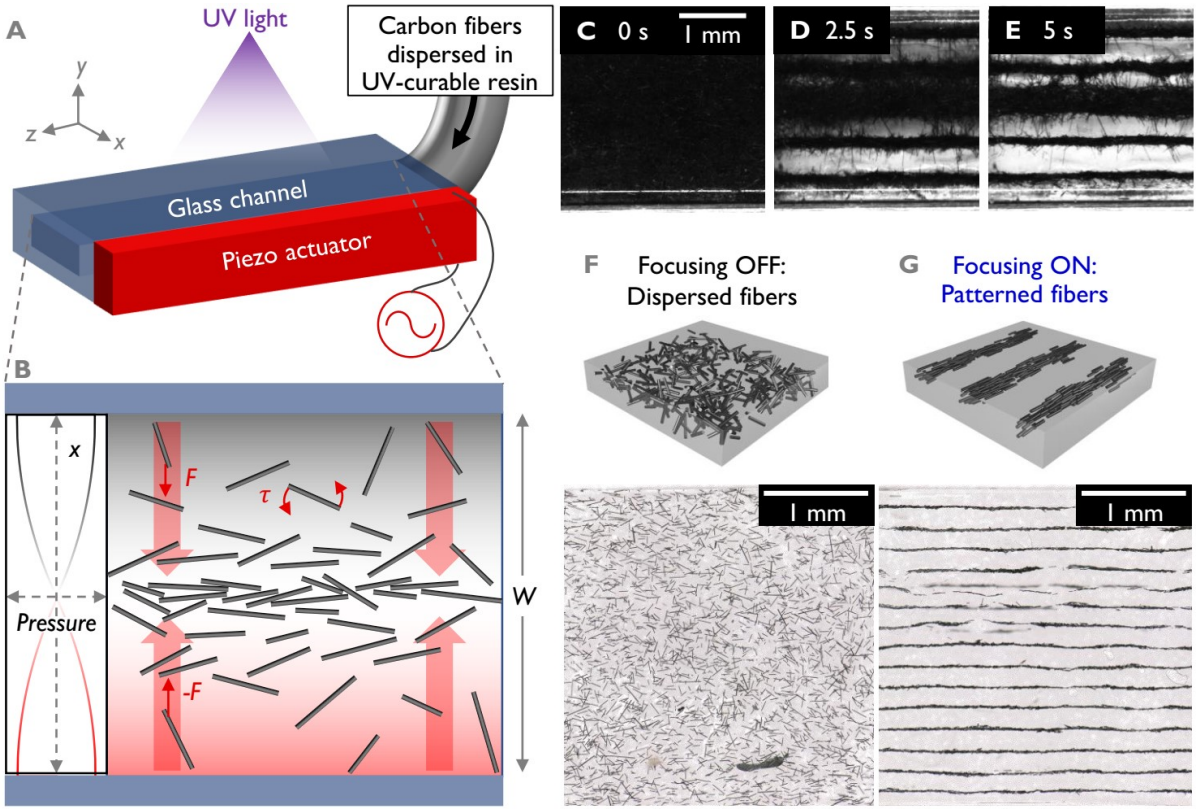

Figure 3.1: **A** Schematic of acoustic focusing device. **B** Diagram of forces aligning and pushing fibers to a low pressure node in a standing pressure half-wave. **C,D,E** Time-lapse of fibers patterned into parallel bundles by acoustic focusing in photopolymer resin, reaching equilibrium positions after 5-6 seconds. **F** Illustration and micrograph of an unpatterned composite with carbon fibers dispersed in acrylate resin (0.36v% carbon fiber). **G** Illustration and micrograph of a patterned carbon fiber composite (0.36v% carbon fiber, the same ink as in **F**) fabricated with acoustic focusing.

3.1.1 Introduction

Acoustophoresis utilizes pressure fields to manipulate particles suspended in a fluid—here, ink in a direct-ink-write printing nozzle. Pressure fields are generated by resonating the channel walls of the glass nozzle with a piezoelectric actuator[44,84,85], as shown in Figure 3.1A. When the walls are oscillated at the channel's fundamental resonant frequency $f_1 = c/(2W)$, where c is the speed of sound in the ink and W is the channel width, a sinusoidal pressure field $P_1 \propto \sin(2\pi x/W)$ is established across the channel. Particles are

pushed to the nearest of n low-pressure nodes spaced equally across the nozzle, as shown in Figure 3.1, and settle due to gravity. Minimal spreading of the focused particle patterns due to gravity is observed, and for the field strengths, particle loading levels, and channel heights used for particle assembly and printing applications, this is unlikely to occur at high enough of a degree to distort focused particle patterns. A thorough treatment of the acoustic forces and torques on rod-like particles is given in Section 2.

To demonstrate spatial programming of electrical conductivity using acoustophoresis, we employed a two-component ink consisting of short carbon fibers or silver-coated glass fibers in acrylate photopolymers. First, composites were UV-cured without acoustic focusing, with fibers uniformly dispersed, as a control case representing conventional 3D-printed fiber composites. Next, using an identical precursor composition, the fibers were focused into bundles using acoustophoresis before the composite was UV-cured, yielding patterned composites. We will first discuss the 1D electrical properties of rigid composites made with either carbon fibers (for their consistency in conductivity) or silver-coated glass fibers (for their high conductivity) first, follwed by a discussion of network anisotropy and material flexibility.

3.1.2 Experimental methods

Materials and Particle Suspension

Milled carbon fibers (Nippon Granoc XN-100-15M; 7±1 µm in diameter and 80±60 µm long) were filtered with sieves into populations with length distributions of 60±20 µm, 90±40 µm, and 130±70 µm. The UV-cure monomer consisted 1,6-hexanediol diacrylate (HDDA) (80% with 100ppm quinone inhibitor, Sigma Aldrich) and 2.5wt% photoinitiator (1-hydroxycyclohexyl phenyl ketone, Sigma Aldrich). The fibers were weighed dry with a microbalance and resin volumes were drawn with micropipettes, then vortexed and

loaded into focusing channels via syringes. The viscosity of this suspension is < 10 cP (Newtonian) at room temperature and low particle volume fractions (< 10v%).

Acoustic Focusing Device

Focusing channels were constructed from borosilicate capillaries, 0.3×3 mm rectangular cavity cross section (Borotubing Vitrotubes) cut to 15 mm and attached to metal ferrules (0.25 mm^2 cross-section, McMaster) with polyolefin heat-shrink and Epoxy (5-min, Devcon) for loading with syringes via plastic tubing (TYGON, .04" ID). The channels were fit into a focusing device, which consists of a piezoelectric transducer superglued to a machined aluminum channel holder (1 mm wall thickness). The piezoelectric transducers (2 mm thick PZT26, 1 MHz thickness mode, Steminc SMPL20W15T21R111) were soldered to BNC connectors and driven with a signal generator, power supply and amplifier (Fluke 294, Tenma 72-7245, Minicircuits LZY-22+) and monitored in parallel with an oscilloscope (Agilent). The channel holder featured a machined lip to hold the glass capillaries snugly in place and was acoustically coupled to the glass capillary with ultrasonic coupling gel (PosiTector). Capillaries were clamped gently in place with rubber bands to avoid compressing the piezo. An air gap was machined in the holder below the capillaries to prevent pressure wave transmission from the channel holder in y- and z-directions and thereby increase pressure field uniformity. The piezo was fixed to the side of the channel holder so that the actuation direction was oriented parallel to the focusing direction in the channel[99,100]. The piezo was coupled to a water-cooled copper heatsink with thermal couplant (Wakefield Type 120) to hold the piezo temperature, measured with a thermocouple, at ambient temperature.

Patterning and Solidification

The unpatterned dispersed-fiber samples made without acoustic focusing were UV-cured immediately in the device (in 3-5 seconds after dispersion, to avoid letting fibers settle) with a 365 nm UV LED (EXFO Omnicure LX400 with focusing lens, $\sim$1 W/cm^2) for one minute (<0.5 seconds to gel, 1 second to solidify).

Patterned samples made with acoustic focusing were made by driving the piezoelectric actuator at a resonant frequency of the piezo-channel system. Resonant frequencies were identified as sharp valleys in the impedance magnitude spectrum (shown in Figure 3.7). At 3.3% carbon fibers in HDDA by volume, resonances were measured at 0.660MHz, 0.948MHz, 1.104 MHz, 3.292 MHz, which are the fourth, fifth, sixth, and fifteenth harmonics of the fundamental resonant frequency (confirmed by counting the number of particle lines formed and by fitting to $f_n = nc/2W$). For other particle volume fractions, the resonant frequencies change slightly due to changes in the speed of sound through the resin-fiber suspension[130]. These resonances were found manually by observing particle patterns through a stereoscope and adjusting the driving frequency until particle patterns were straight and uniform. The piezo actuator center driving frequency (dictated by piezo thickness) was chosen to match these observed device resonant frequencies: 0.667, 1.0, and 3.0 MHz piezo resonances overlap the channel resonances and result in strong excitation. The piezoelectric transducer was driven at 20 Vpp, so that particles reached their equilibrium patterns within six seconds. Higher driving voltages form patterns more quickly ($V \propto \sqrt{E_0}$[98]) but tip the balance of streaming drag forces and acoustic radiation forces so that particles get caught in streaming vortex rolls and don't equilibrate to static positions[100]. After the particles reach their equilibrium positions, the samples were immediately cured with a UV LED.

The ends of the composites were coated with conductive silver epoxy (Circuitworks

Conductive Pen) and contacted with probes (with contact resistance 2 Ohms, as determined by calibration to metal with known conductance). The resistance of the samples was measured with a multimeter (Fluke 115) and a current-voltage sweep using a source meter (Kiethley 2636A). The conductivity of the composite samples was determined using the resistance of the sample and using the cross-sectional area of the entire composite (0.9 mm^2). The percolation threshold ϕ_c is calculated as the average of the highest volume fraction (volume of carbon to total volume) that results in an open circuit and the lowest volume fraction which results in a closed circuit, with error equal to the half difference between the two. Four measurements were taken within 0.5% of the observed transition in each of four trials; an overlap was observed in only one of the trials, and three more measurements were made to identify the outlier in that trial.

3.1.3 Results and Discussion

Dispersed-fiber composites follow the predictions of percolation theory

The control-case dispersed-fiber composites, made without acoustic focusing, are shown in Figure 3.2A. These unpatterned composites are insulating at fiber volume fractions $\phi < 3.3$v%, resulting in an open-circuit measurement (Figure 3.2D). Above 3.3v%, these composites have low conductivity (< 1 S/m), with around 1% of the fibers contributing to the conductive network. This transition from insulating to conductive is termed the percolation threshold ϕ_c. The experimentally observed threshold coincides with the theoretically calculated value, $\phi_c = 1/(\pi/2a + 2a + 3 + \pi) = 3.3\%$, where $a = l/d$ is the aspect ratio of the fibers[6]. This calculation assumes monodispersity and random fiber orientation; considering the polydispersity of the fiber distribution makes <3% difference in this case[6]. Below this threshold, too few particles are in contact to form a continuous network, so that charge transport across the material is blocked by regions of insulating

matrix material. Above ϕ_c, however, a continuous conductive network is formed across the material. Percolation theory models the conductivity of two-phase composite materials like these as $\sigma = \sigma_0(\phi - \phi_c)^2$ for $\phi > \phi_c$[6], where σ_0 is a fitting parameter that gives the particle and contact resistance[131], and the exponent value of 2 describes a 3D network of low aspect-ratio ($a < 100$) fibers. Conductivity is expected to be overestimated by this model due to hydrodynamic alignment of fibers during loading of the channel[6], as is indeed observed in our data at higher loading values where higher viscosity increases the effect of shear flow particle alignment. The particle and contact resistance σ_0 for carbon fibers is 1000 S/m, two orders of magnitude lower than the nominal conductivity of the fibers alone, indicating that there is significant contact resistance between the carbon fibers (as expected).

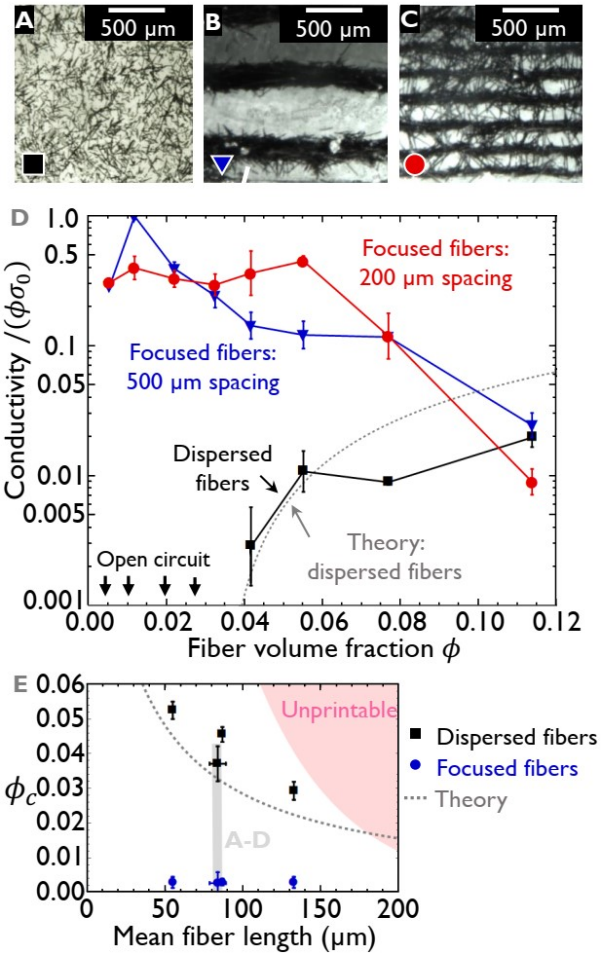

Figure 3.2: **A** Micrograph of a 0.5v% composite made without acoustic focusing. **B** Micrographs of 2.6v% composites made with acoustic focusing with 500 µm focused bundle spacing and **C** 200 µm spacing. **D** Electrical conductivity normalized by the conductivity of the fibers σ_0 and the volume fraction ϕ, which gives the volume fraction of fibers in the composite that contribute to the conductive network. Error bars represent standard deviation, and the dashed line represents a theoretical model. Fiber alignment by shear flow, a factor especially apparent in the higher-viscosity inks with high ϕ is expected to decrease conductivity below this model[6]. **E** The percolation threshold ϕ_c at which electrical behavior of composites transitions from insulating to conductive. Fiber alignment is expected to increase ϕ_c compared to the theoretical model shown here, and high spread in the fiber length distribution is expected to decrease ϕ_c[6]. Composites in **A-D** have the fiber length distributions with high standard deviation highlighted in grey in **E**. The "unprintable" region indicates approximately which volume fractions and fiber lengths clog the devices.

Acoustically patterned composites have high conductivity at low fiber loading

Patterned composites formed with acoustophoresis (Figure 3.2B-C) have dramatically higher conductivity than the unpatterned composites, as shown in Figure 3.2D. This is due to efficient use of particles, forcing fillers into percolated bundles instead of relying on random contacts in a stochastic network. Below the percolation threshold for dispersed-fiber composites ϕ_c, where the unpatterned composites are insulating, the patterned composites have high conductivity. Up to 97% of the fibers by volume contribute to the conductive network at $\phi = 1.2$v% because fibers preferentially stack end-on-end due to scattering forces in the x-direction[53], a configuration which optimizes filler utilization for 1D transport. Thus, as opposed to the high concentration of fibers required to form robust percolating networks in dispersed-fiber materials, forcing fibers into efficient configurations allows high conductivity even at low loading. At volume fractions up to 8v%, the conductivity of the acoustically patterned composites is at least an order of magnitude higher than that of unpatterned percolated composites made with the same precursor ink due to efficient particle distribution.

At the lowest loading value investigated, 0.4v%, focused lines break continuity due to particle scarcity, so that conductivity drops. At volume fractions above 1.2v%, the contact efficiency decreases somewhat as some fibers are oriented radially outward from the bundles (not contributing to the network) but remains an order of magnitude higher than the unpatterned composites until 12v%. At 12v%, the maximum printable loading before channels clog, the normalized conductivity decreases to 1-5% because such high solid content produces scattered-wave interactions[41] and distorted pressure fields which disrupt assembly. In contrast to the strong scaling in dispersed-fiber composites, conductivity in acoustically patterned composites is invariant from 1-10v%. This insensitivity to loading provides freedom to orthogonally control other material properties like stiffness, strength,

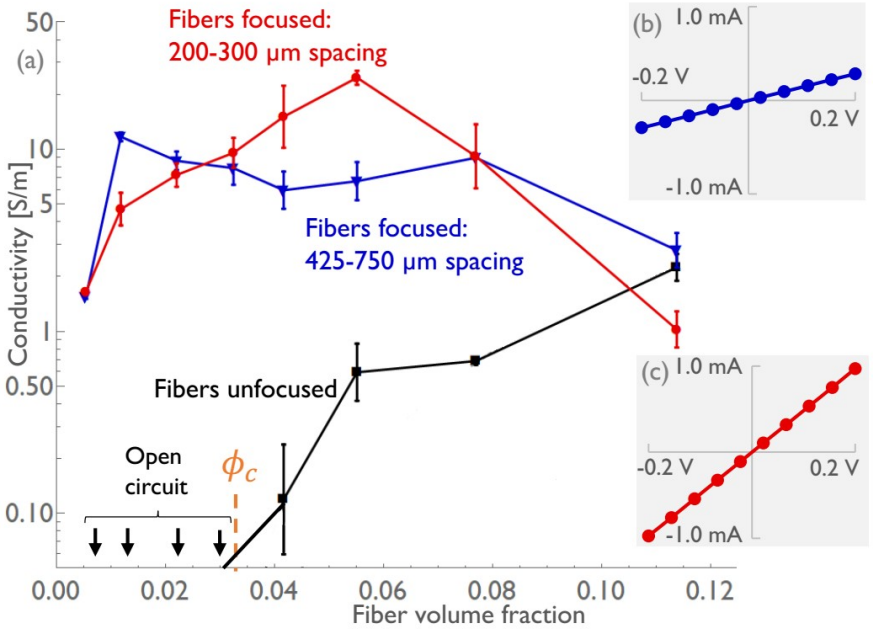

Figure 3.3: Conductivity versus fiber volume fraction. (Inset b) Current-voltage curve for 2.6v% composite with 500 µm spacing (5.3 S/m). (Inset c) Curve for 2.6v% 200 µm spacing composite (18.0 S/m in parallel direction).

or thermal conductivity by tuning the filler loading while maintaining high electrical conductivity.

Additionally, the critical volume fraction for conductivity in patterned composites is an order of magnitude lower at (0.36v%) than that of the dispersed-fiber composites, as shown in Figure 3.2E. For unpatterned composites the percolation threshold is strongly dependent on fiber length, such that long fibers are better for conductivity (but worse for clogging)[6]. For patterned composites, the critical loading for conductivity is independent of fiber length because fibers are stacked end-on-end, although conductivity decreases for short fibers because of the added contact resistance. This further adds opportunities to control mechanical or other properties via fiber length while maintaining conductivity.

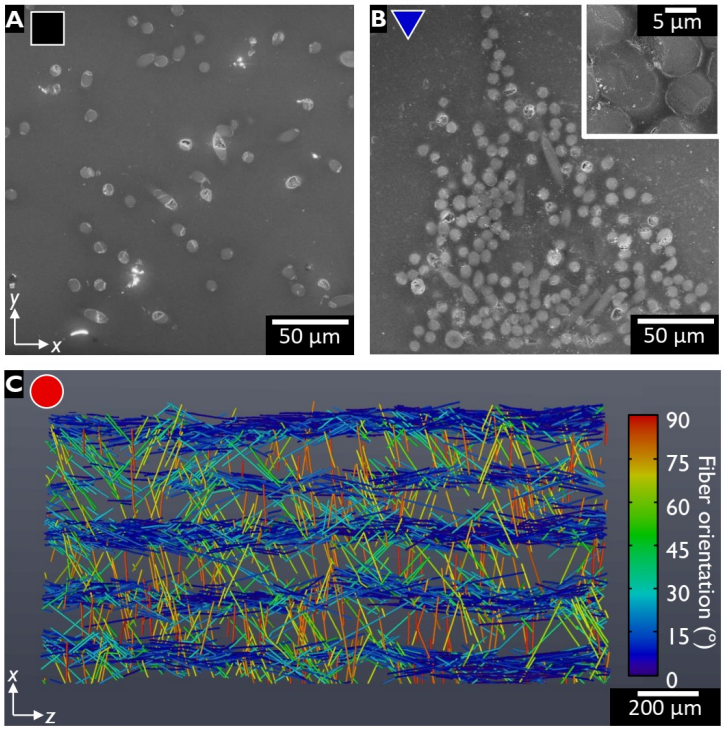

Figure 3.4: SEM images of cross-sections of 2.6v% carbon-fiber composites with **A** no focusing (insulating) and **B** 500 µm focused bundle spacing (anisotropic conductive). **C** X-ray computed tomography image with cylinders fit to fibers of a 2.6v% carbon-fiber composite with 200 µm focused line spacing (conductive), with fibers colored by their angle with the z axis.

Within the focused bundles themselves this high conductivity is due to high density of contacts between fibers, as revealed by cross-sectional SEM images and X-ray CT scans of focused fiber bundles, as shown in Figure 3.4. The (non-normalized) conductivity of composites is roughly constant at 10 S/m for 1-10v% loading, and is Ohmic (Figure 3.3), compared to < 1 S/m for unpatterned composites.

Electrical anisotropy is controlled by focusing wavelength

The conductivity reported above is one dimensional, running parallel to the focused bundles of carbon fibers, where bundles are insulated from each other. Control over conductivity in the perpendicular direction, however, is possible by tuning the applied pressure field. Modulating the focusing wavelength controls the bundle spacing $\lambda/2$,

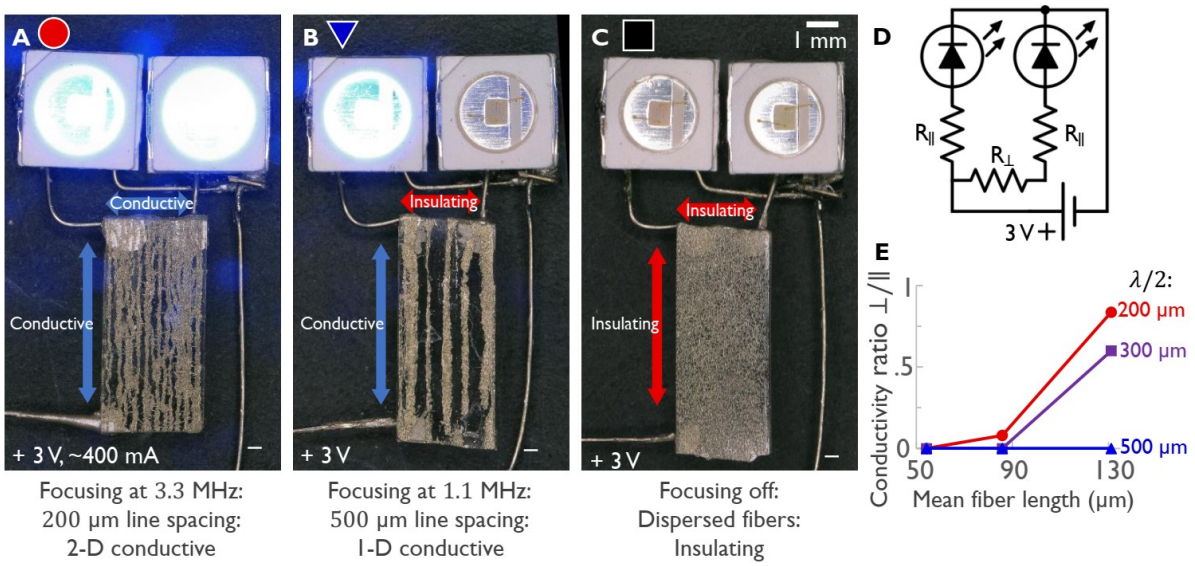

Figure 3.5: Three composites made using the same precursor ink, 2.6v% silver-coated glass fiber in acrylate resin: **A** An isotropic conductive composite with focused bundle spacing $\sim$ 200 µm completing a 3 V circuit to illuminate two 100 mA LEDs. Differences in LED brightness are due to tilt of the metallic reflector with respect to the camera. **B** An anisotropic conductive composite with bundle spacing $\sim$ 500 µm completing a 3 V circuit to illuminate only one LED. **C** An insulating composite made with acoustic focusing turned off. **D** Schematic of the circuit in **A-C**. **E** Dependence of transport anisotropy in 2.6v% composites on mean fiber length and bundle spacing, given as the ratio of conductivity measured in the direction perpendicular to the focused lines to that measured parallel.

which in turn controls the number of fibers bridging between bundles: fibers longer than $\lambda/4$ are acoustically stable perpendicular to the focused bundles, bridging between bundles[112]. This in turn controls the density of transport pathways between bundles in the perpendicular direction and anisotropy in conductivity in the material. The focused bundle spacing is equal to the half-wavelength of the pressure field: focusing at $f = 1.1$ MHz yields spacing $\lambda/2 = 200$ µm; focusing at $f = 3.3$ MHz yields $\lambda/2 = 500$ µm, and so on (Figure 3.7). As shown in Figure 3.5E, composites made with long fibers and close bundle spacing (mean length 130 µm, $\lambda/2 = 200$ µm, shown in Figure 3.4C) have a high density of bridging fibers and, as a result, nearly-isotropic conductivity. Conductivity

measured in the direction perpendicular to the focused lines (denoted $\perp$) is 84% that measured in the parallel direction ($\parallel$). At the widest spacing (500 µm) even using the longest fibers, bundles are insulated from each other in the perpendicular direction and the material is totally anisotropic (i.e. insulating in the perpendicular direction). An intermediate wavelength of 300 µm has 60% anisotropy, providing a smooth transition between the totally anisotropic and nearly-isotropic values. Other wavelengths outside of this transition range, shown in Figure 3.7, remain anisotropic (600, 750, 1000 µm) or nearly-isotropic (<200 µm), although their conductivity values are less consistent since the device design did not target these wavelengths. It is straightforward to modify the device to target other wavelengths using channel widths and piezo resonances with the corresponding values. By controlling the focused line spacing, the electrical conductivity of the patterned composites can be modulated between anisotropic or nearly isotropic. This could be accomplished on-the-fly during 3D printing to allow programmable spatial control of electrical interconnects embedded in printed components.

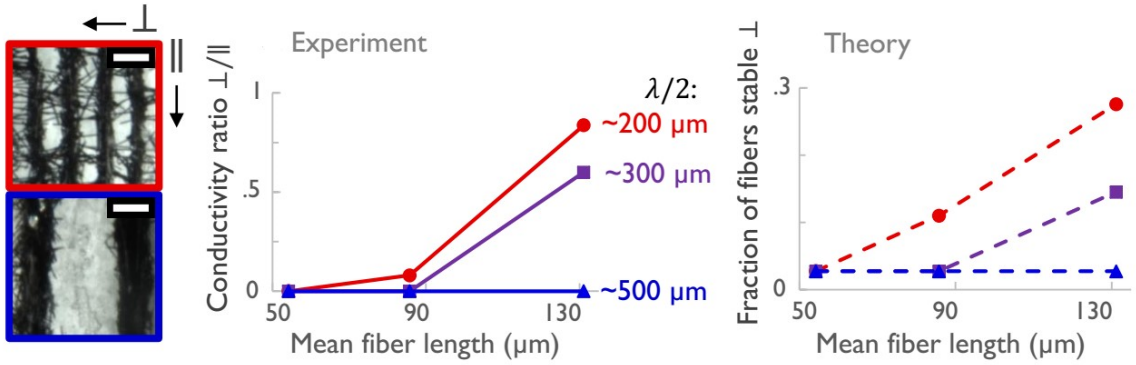

Figure 3.6: Conductivity anisotropy for various bundle spacing and fiber lengths, compared to theoretical modeling (Section 2.2) of the fraction of fibers that are stable in bridging configurations at equilibrium (perpendicular to focused bundles).

Theoretical models of fiber bridging behavior (the projected-area model given in Section 2.2) qualitatively agree with our data (Figure 3.6). Note that for these longer fibers with length approaching a quarter-wavelength, the projected-area is appropriate[112],

whereas it is inaccurate for shorter rods. The equations of motion given by balancing the force and torque on fibers with drag (with $E_0 \approx 5$ J/m^3 from a fit to experimentally recorded particle trajectories), demonstrate that at equilibrium 28% of fibers are stably oriented perpendicular to the focused bundles when starting from a uniform dispersion in the case of long fibers focused to narrowly-spaced (200 µm) bundles, as shown in Fig. 3.4D. In contrast, in more widely-spaced bundles, very few fibers are stable in the perpendicular orientation: at $\lambda/2 \approx 500$ µm, 3%, and at $\lambda/2 \approx 300$ µm, 8%. For fiber lengths below a quarter-wavelength, finite element models are more accurate, but predict even lower stability in the bridging configuration, which would not significantly change the results here (Section 2.3). Indeed, few perpendicularly-oriented fibers are observed experimentally in composites with wide line spacing according to elliptical fits of fiber cross-sections (Fig. 3.4A). This agreement indicates that fiber stability in pressure fields dictates fiber bridging behavior. Near-field forces arising from pressure waves scattering off adjacent particles[53] and particle collisions may also play a role in explaining fiber-bridging behavior.

Patterning silver-based composites

In terms of non-normalized conductivity, silver-coated glass fibers (Potters Conduct-o-fil AGCLAD12, 150×10 µm) impart conductivity of >5000 S/m to patterned composites, or 48% of the conductivity of bulk silver normalizing to the volume of silver in the composites, which indicates a low contact resistance and high particle utilization. This normalized value compares well to conventional inks, which typically only reach values >30% after polymer burn-off and particle sintering steps (>200° C)[132]. The non-normalized conductivity is lower because of the low volume of silver in the silver-coated fibers, but is nonetheless on the same order of magnitude as the highest-conductivity long-CNT composites with $\phi > 10$wt%[67]. These materials have ample conductance for mm-scale soft-robotics applications, which typically require <100 mA for 1 N actuators[133,134]. As a demonstration,

a 2.6v% composite completes a circuit to supply ∼400 mA to 3 V LEDs in Figure 3.5. Anisotropy is modulated by choosing focusing frequencies that either result in close spacing and fiber bridging, and therefore nearly isotropic conductivity as in Figure 3.5A, or wide spacing and therefore anisotropic conductivity as in Figure 3.5B. The unpatterned composites made with the same precursor ink but without acoustic focusing, Figure 3.5C, are sub-percolation and thus insulating. Thus, during printing one can define where conductive or insulating material is patterned all while printing using a single nozzle and ink to define simple circuits and interconnects in components.

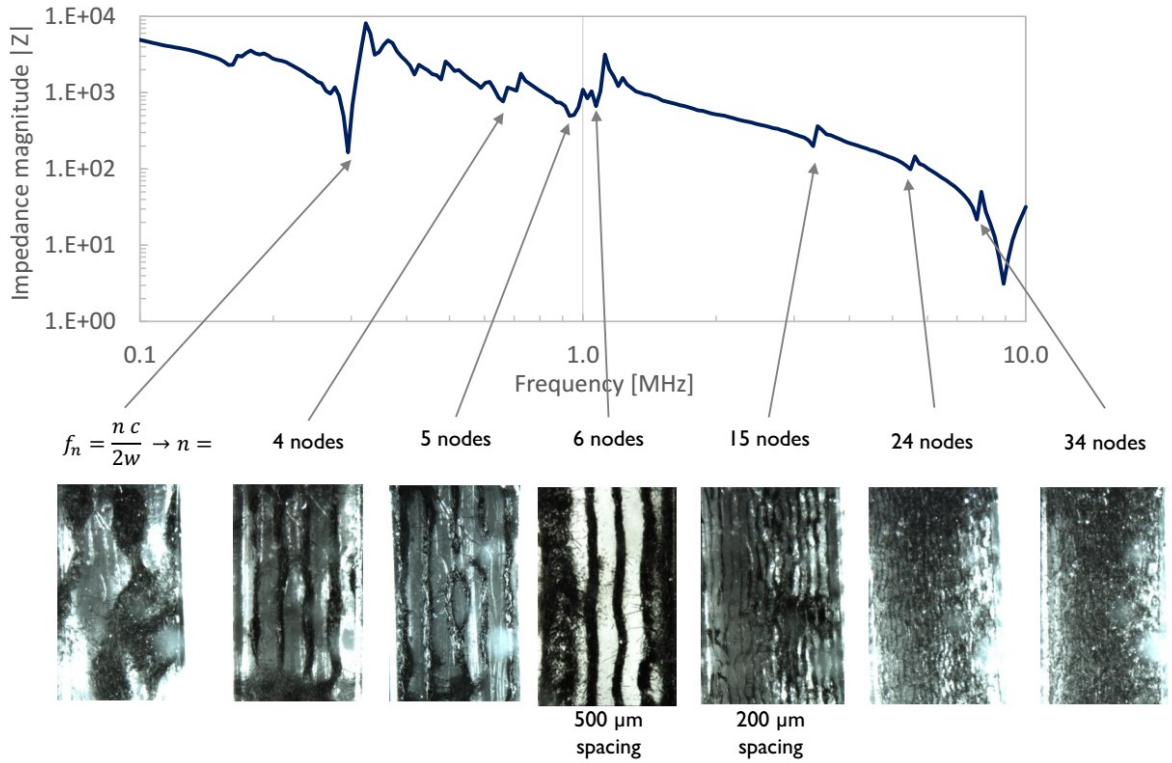

Figure 3.7: Impedance magnitude spectrum of a piezo coupled to a focusing nozzle loaded with 2.6v% carbon fiber in HDDA monomer ink. Resonant frequencies are located at the sharp troughs in the impedance spectrum. Micrographs are shown of the patterns that result from focusing the same device at exactly those resonant frequencies.

3.1.4 Conclusions

In summary, acoustically patterning filler particles into highly efficient percolated networks in composites increases their conductivity by an order of magnitude over conventional dispersed-fiber composites made with the same ink, due to much higher particle utilization efficiency in the percolated networks. Conductivity reaches 48% that of bulk silver within the conductive networks, a value that typically requires sintering (a high-temperature step which is not compatible with many printable or flexible polymers). The composites require an order of magnitude lower particle loading to be conductive compared to dispersed-fiber composites, and have high conductivity values relatively insensitive to changes in particle loading. This allows orthogonal control of other material properties, like mechanical flexibility, whereas conventional composites have strongly coupled conductivity and brittleness. As a result, other properties like mechanical flexibility can be simultaneously introduced to these materials, as discussed in Section 4. This technique is compatible with 3D printing of a wide variety of particle and matrix materials whereas the current alternatives for optimizing conductivity are not. Finally, we demonstrate that modulating assembly parameters allows patterning of either 2-D conductive, 1-D conductive, or insulating material, all using the same nozzle and ink. This technique is a novel approach to manipulating microstructure to enhance and modulate material properties during printing, paving the way for printing soft components with embedded electrical interconnects or other functional elements.

3.2 Thermal conductivity

This section investigates thermal functionalities, which operate under similar transport mechanisms to electrical conductivity but have a smaller disparity between the conductivity of the particle and matrix phases and have a higher sensitivity to interfacial resistance. As a

result, this section more closely characterizes the contacts between particles, finding certain particle shapes stack and pack more densely, minimizing contact resistance and increasing conductivity. This knowledge is used to develop materials that address major challenges in the thermal composite application space in increasing conductivity at the lower particle loading necessary for mechanical stability and low viscosity during processing.

3.2.1 Introduction

As electronics miniaturize and the power density of components increases in devices like smartphones, light emitting diode (LED) arrays, and laser diodes, heat dissipation increasingly becomes a limiting factor to improving device performance, necessitating new materials and strategies for heat management [65,68,69]. In the computer chip manufacturing industry, for example, new polymer composite infill materials with high thermal conductivity are needed to cool the next generation of stacked chips [68], and in LED, battery, laser diode, and other electronics packaging, 3D printed polymer composites have become a leading candidate for lowering the processing cost of heat sinks, heat spreaders, and printed components with integrated electronics [69,73]. For these applications, developing composite materials with higher conductivity that retain processability is a difficult problem. The material must have high enough thermal conductivity to transport heat from hot spots to heatsinks without buildup, but this generally requires a high loading of conductive filler particles that creates processing challenges because highly loaded materials become viscous during processing and brittle after solidification [71,73]. Such properties result in poor mechanical integrity during thermal cycling and prohibit wetting and infiltration around small components and chip stacks for good thermal coupling [68]. This processing problem is limiting the performance, longevity, and design flexibility of electronics and driving demand for higher conductivity without excessive viscosity and embrittlement.

Developing these processable, highly-conductive materials requires utilizing the heat transport capabilities of the filler material as efficiently as possible so that global filler loading can be kept low. Efficiently utilizing filler particles requires controlling their spatial distribution within the composite, orienting them so that heat flows through their most conductive axes and in the desired directions in the material, and assembling them into continuous networks. Contact density between conductive particles must be maximized to form extensive percolated pathways (continuous networks of contacting conductive particles) throughout the composite to maximize heat flow through the conductive filler and minimize the contribution of the highly resistive matrix (and its interfaces with the filler) [70]. Current approaches rely on hydrodynamic [71–73] or magnetic [135–137] alignment of particles, which increase conductivity by aligning the conductive axes of particles with the heat flow, but rotation of particles alone does not form efficient percolated networks (and indeed is often detrimental) [6,138–140]. Concentrating particles into continuous networks to increase particle contact density requires translation of particle in addition to rotation, necessitating programmable assembly forces and torques on particles. In addition, assembly techniques with high versatility in material choice, high degrees of control over particle placement, and fast assembly rates allow further optimization of properties and compatibility with processing applications.

One promising method to pattern filler particles into such networks is with pressure field directed assembly. During this assembly process, pressure fields exert forces and torques to manipulate filler particles in a process called acoustophoresis or acoustic focusing, both aligning and translating them within a photopolymer before curing. The pressure fields are induced in fluidic channels by oscillating the channel walls with a piezoelectric transducer, and forces on particle arise if they have a contrast in density or compressibility with the surrounding fluid, as is the case for nearly all solids in liquids, allowing uncontrained choice in particle and matrix material [44]. In a one-dimensional

standing pressure wave, acoustic forces pushes particles to the low-pressure nodes of the field, forming stripes across the material as illustrated in Figure 3.8. This force scales with the particle volume and can generally overcome drag for particles with diameter larger than one micron in low-viscosity matrices[44]. In two-dimensional fields, grid patterns can readily be formed, and more complex, user-defined patterns are possible via field shaping methods[42,43]. Using this method, patterned areas can span centimeters, and assembly times are on the order of one second[34], readily compatible with 3D printing and other processing methods.

3D printing these patterned composites is particularly promising for improving thermal management in electronics because of the potential for engineering cooling networks that direct heat along optimized paths through components. Materials with anisotropic thermal conductivity, e.g. via aligned filler particles, further optimize heat flow along engineered paths, maximizing heat dissipation performance[71]. In particular, these engineered heat paths allow heat spreaders and thermal interface materials to direct heat more efficiently to heat sinks or pipes and enable more optimized heat sink designs, which for conventional aluminum components can incur large processing costs (up to 80% of the total packaging cost in some applications[68]). In addition, 3D printing composites offers the benefits of reducing device weight, tuning thermal expansion anisotropy via filler orientation, and lowering electromagnetic interference noise in circuits with nonmetallic filler[72]. Finally, trends toward 3D printing of parts with integrated electrical components, as well as microelectronics themselves in some applications[63], reinforce the value in integrating thermal management systems into the 3D printing process rather than during post-processing. Here, microstructure control via acoustic patterning is implemented into 3D printing by coupling piezoelectric transducers to the liquid photopolymer bath of a stereolithographic printer and subsequently projecting light patterns into the photopolymer (here, hexanediol diacrylate [HDDA]) to cure a layer of the print onto a movable substrate (Figure 3.8A-C).

Cross-plane continuity is achieved by tuning the thickness of the concentrated particle stripes[34,51] to ensure contact between layers (Figure 3.8D).

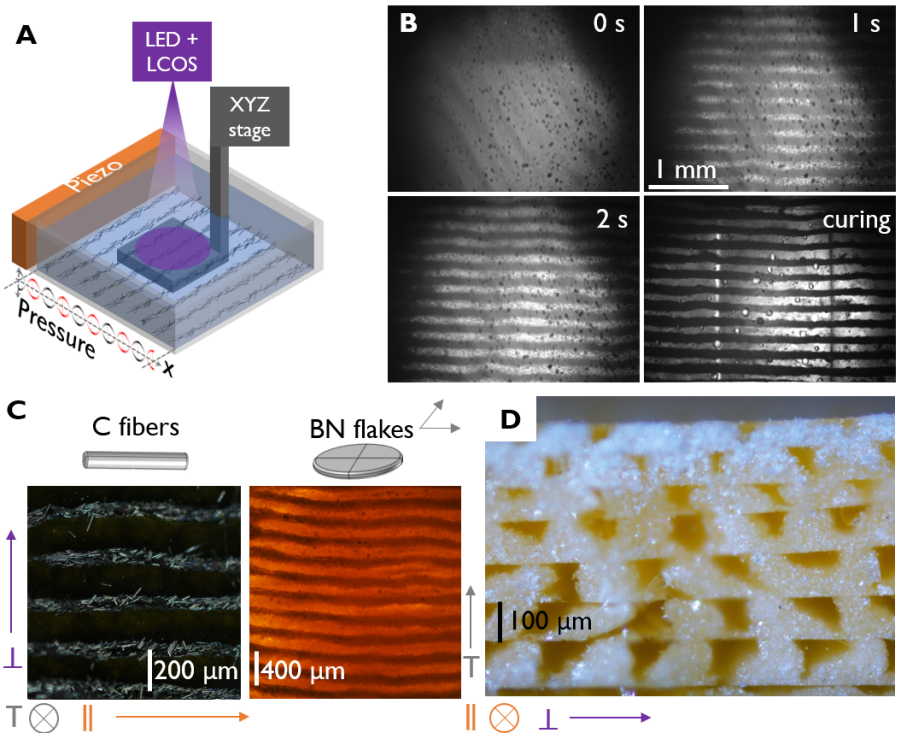

Figure 3.8: **A** Schematic of the micro projection stereolithography printing setup. **B** Time-lapse of the focusing process for boron nitride flakes at 12v% in HDDA, and micrograph of the curing process. **C** plan-view and **D** cross-section of printed 1 mm thick 12v% boron nitride flake and carbon fiber samples with ten 100 µm-thick layers.

This acoustic patterning method, integrated into stereolithography, aligns and compacts carbon fibers and boron nitride flakes into conductive stripes embedded in polymer, forming efficient heat transport pathways through composite materials. The thermal conductivity of these patterned materials reaches 75-95% of the parallel conduction upper limit parallel to the lines (and only 25% perpendicular), with enhancement over unpatterned materials up to 300% and the anisotropy up to 350% for carbon fiber composites. Conductivity of 2.5 W/m.K is nearly identical to recent filament deposition modeling studies that use aligned graphene at similar loading levels[71,73], but whereas the filament-extruded materials are

brittle when cured (failing at <10% strain) and highly viscous during processing (>10^5 Pa s), acoustic patterning fully encapsulates conductive particle networks in sheathes of polymer with low viscosity (<10^{-3} Pa s), absorbing strain and preventing particle delamination (withstanding over 500 cycles to 22% strain without loss in conductivity when using flexible polymers, as demonstrated in previous studies[28]). This low viscosity allows wetting of circuit components for efficient thermal coupling, important especially in stacked computer chips, and the strain tolerance improves mechanical performance of components, especially during thermal cycling. To find routes to further increase thermal conductivity, we characterize the packing of filler particles and relate results to finite element analysis of driving forces for assembly, illuminating opportunities to optimize particle geometry for efficient packing and heat transport across particle interfaces.

3.2.2 Experimental Methods

Resins were prepared with hexanediol diacrylate monomer with 1.6wt% IRGACURE 819 as photoiniator and 0.38wt% SUDAN 1 as absorber. Carbon fibers were filtered with 25 and 53 micron sieves and images were processed in ImageJ to determine mean fiber lengths. The carbon fibers (Granoc XN-100-15M) or boron nitride flakes (CoolFlow CF500) were then weighed with a microbalance and vortexed into the resin.

The resin was poured into a stereolithography bath measuring 1×2 inches made from glass slides glued with silicone adhesive. Two piezoelectric transducers (StemInc SMPL20W15T21R111) were glued inside the bath and wired in parallel, driven by a function generator (Tektronix AFG3052C) and 45 dB amplifier (ENI 510L).

The UV light is projected via a UV LED and liquid crystal on silicon display into the bath. This top-down strategy necessitated a floating polydimethylsiloxane damping layer to reduce distortions due to surface waves at the free surface, which also eliminated

streaming motion of the fluid in the fluid confined between the printing substrate and the floating membrane. This method successfully printed 1 mm thick components with 100 µm layers, with feature sizes limited by scattering in the resin to approximately 10 µm. Lateral component dimensions are limited to the bath size and travel range of the build plate controlled by 3D motion stages.

The bath vertical position was also controlled with a motion stage, and the top surface of the resin was set at the focal plane of the the projected image. The printing substrate, a silicon wafer functionalized for optimal wetting with the monomer, was also placed at this focal plane with 3-dimensional motion stages, and confirmed to be level by reflecting a laser pointer off the resin surface and substrate onto a nearby surface.

The filler particles in the resin were dispersed using a stir bar and rare earth magnet mounted below the bath on a direct current motor, as well as occasional manual stirring in the corners of the bath. The entire bath was enclosed in an acrylic chamber fed with nitrogen (1 liter per minute) and oxygen (5 milliliters per minute) to maintain an oxygen concentration between 3.5 and 4%, as measured by an oxygen sensor. The pressure wave was actuated with wavelength 400 µm at 11 V. The desired layer's pattern was then projected at 5 amps for 5 seconds, and the substrate was lowered to repeat the process on subsequent layers.

Thermal conductivity was measured using an infrared camera (FLIR SC660). The sample to be measured was bonded (with AquaDag E colloidal graphite) on opposite sides to reference samples cut from a standard material (304 stainless steel) to the same dimensions as the sample to be measured. The stack of three samples was then bonded between an aluminum cold plate and an aluminum hot plate embedded with cartridge heaters driven by PID controller (Omega). The surfaces of this stack facing the camera were sprayed with a light coat of boron nitride aerosol (ZYP Lubricoat), measured to be less than 5 µm in thickness, to ensure a uniform emissivity. The temperature gradient

across the two reference materials (excluding the edges where nonlinearity was evident) was then calculated and heat losses to radiation and convection were quantified following the ISTM standard[141]. 304 stainless, borosilicate glass, and polystyrene reference samples were measured using this method to within 1% of known conductivity values. In the composite samples, trials on multiple printed samples resulted in a standard deviation of less than 5% of the mean.

X-Ray computed tomography scans were performed on a 12v% patterned boron nitride sample using a Zeiss Versa 510 with a voxel size of 0.5 µm cubed. The scans were reconstructed using Livermore Tomography Tools[142] and segmented in Fiji[143] using the XLib Disconnect particles plugin[144], and then an ellipsoid fit was performed using the MorphoLibJ package. Contacting particles were analyzed using Blob3D[145].

3.2.3 Results and Discussion

Thermal conductivity anisotropy

he acoustic patterning method successfully compacts filler particles into locally dense stripes during the 3D printing process. As shown in Figure 3.8B, patterning is rapid, reaching equilibrium particle positions in <3 seconds, and photocuring lock patterns into place without loss of structure. 100 µm thick layers of material ensure contact between stripes in the cross-plane direction (as predicted by previous simulations[34]), shown in Figure 3.8C-D. The thermal properties of these materials are measured using infrared thermography (Figure 3.9A) incorporating two reference samples with known conductivity to account for losses to convection and radiation[141], as detailed in the Experimental Methods section.

To begin, we measure thermal conductivity along different directions in the patterned composites and find high anisotropy. The thermal conductivity, k, of carbon fiber samples

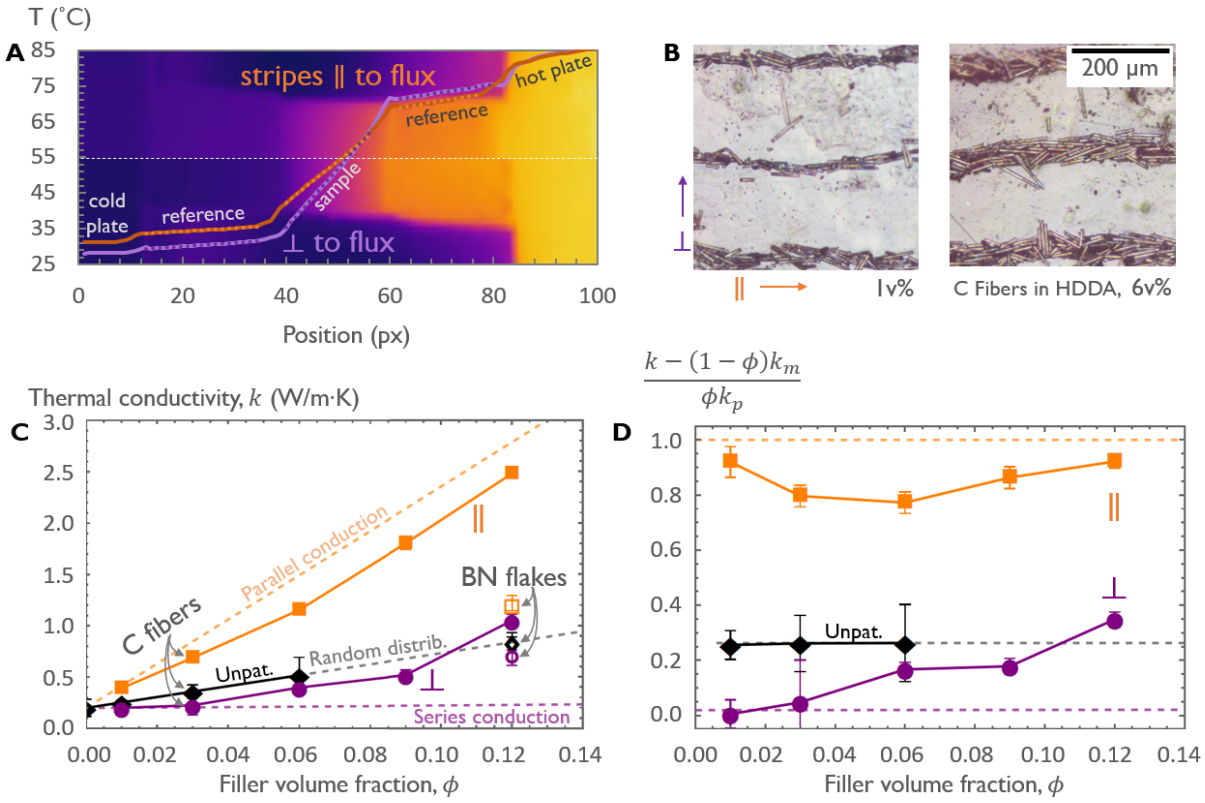

Figure 3.9: **A** Thermal profiles overlaid on infrared images of the measurement setup. Samples oriented with focused stripes parallel (top image, orange curve) and perpendicular (bottom image, purple curve) to the heat flow are sandwiched between two stainless steel reference materials with the same cross-section, allowing quantification of thermal losses. **B** Micrographs of patterned carbon fiber samples. **C** Thermal conductivity of patterned and unpatterned carbon fiber samples plotted along with a fit to a model for thermal conductivity in composites with random fiber distribution (Mori-Tanaka model), and the parallel and series conduction models using the fitted parameters for effective particle and matrix conductivity. **D** Thermal conductivity normalized to give the volume fraction of filler particles that contribute to the conductive network.

(Figure 3.9B) is plotted as a function of particle loading, ϕ, in Figure 3.9C. The thermal conductivity with focused stripes oriented parallel to the heat flux (labeled || in Figure 3.9) is up to 350% higher than with the stripes oriented perpendicular ($\perp$) to the flux, reaching 2.5 W/m.K at $\phi = 12$v%. Conductivity is up to 300% higher than unpatterned composites at the same filler loading (made with the same ink and method but with the pressure field turned off), which have isotropic conductivity.

We compare these results to theoretical conduction models to analyze the particle utilization efficiency relative to theoretical ideal networks. To do this, we fit the thermal conductivity of unpatterned composites to the Mori-Tanaka model[146] for conductivity of randomly oriented fiber composites (which has been found to be the best fitting model in similar composites[70,147]). This fit provides a value for the effective filler conductivity, $k_p = 21 \pm 1$ W/m.K, in close agreement with other studies on similar materials[70]. This value is much lower than the in-plane bulk value for graphite because it includes the effects of cross-plane conduction and interfacial resistance between particles and with the matrix[70]. The conductivity of the polymer matrix is $k_m = 0.202 \pm 0.001$ W/m.K, in agreement with literature values for poly(HDDA)[148]. The aspect ratio of the fibers, measured via image analysis and input into the model, is 41 µm mean length by 7.5 µm mean diameter. This model takes the settling of the fibers into account by adding the randomly oriented[111] settled layer with the remaining pure polymer matrix layer in parallel. Note that unpatterned samples with volume fraction higher than 6v% could not be printed because the thicker mat of settled fibers compromised adhesion to the substrate and allowed warping stresses (caused by ∼10% shrinkage of the polymer) to delaminate layers from each other or from the build plate, whereas patterned materials could be printed at higher loading because the light penetration and polymer adhesion to the substrate is unimpeded in the region between focused stripes.

Next, these fitted values are used to construct parallel and series conduction models,

which give the upper and lower bounds for conductivity as a function of filler particle distribution, i.e. the limits given the filler particle material and fiber geometry. The conductivity measured along the focused stripes approaches the parallel conduction upper bound, $\phi k_p + (1-\phi)k_m$. The normalized conductivity plotted in Figure 3.9D is calculated by subtracting the expected conduction through the matrix (assuming parallel conduction) and dividing by the expected conduction due to the particle phase. In the acoustically patterned materials, these values indicate that 75-95v% of the carbon fiber contributes to such a parallel conduction network when the heat flux aligned with the patterned stripes. A similar analysis, wherein the measured conductivity is fit using an effective volume fraction, $\phi' k_p + (1-\phi')k_m$, yields $\phi'/\phi = 82\% \pm 15\%$, i.e. that 67-97v% of particle material contributes to the parallel network. Fitting to $(\phi k_p^n + [1-\phi]k_m^n)^{1/n}$ yields an exponent of $n = 0.92 \pm 0.01$, where $n = 1$ models parallel conduction, $n \to 0$ indicates ideally dispersed particles, and $n = -1$ is series conduction[149], reinforcing the conclusion that the patterned composites have a close-to-ideal parallel conduction geometry. Because some lines break continuity and some fibers have one or zero contacts with the rest of the network, not contributing efficiently to heat transport, these values do not reach 100% of parallel conduction. Nonetheless, this is much more efficient particle utilization than that of unpatterned composites, in which only ∼25v% of fibers contribute to the network because of the random fiber orientation and poor contact density between fibers.

The normalized conductivity in the perpendicular direction increases above the series conduction lower bound, $(\phi k_p^{-1} + (1-\phi)k_m^{-1})^{-1}$, because of overlap between stripes on adjacent printed layers (see Figure 3.8D), which increases as the volume fraction increases, forming a (partial) network across the perpendicular direction in the material. This misalignment between layers is likely caused by a quarter-wavelength shift due to scattering off the build substrate, slightly distorting the standing pressure wave, and the sheared cross sections may be caused by movement of the photopolymer or pressure field during

curing. These imperfections may be eliminated by using a bottom-up stereolithography method in which the build plate can be removed from the bath during the initial curing [41].

Because conductivity nearly reaches the upper bound in the parallel direction, further increasing thermal conductivity requires raising the upper conduction limit via higher k_p, either by using materials with higher intrinsic conductivity (e.g. single-crystal hexagonal boron nitride, preferred in many applications because it is electrically insulating) or improving the thermal coupling between particles (e.g. increasing the particle contact surface area to minimize interfacial resistances). Since thermal conduction is dominated by interfacial resistance [68,70], particles that pack more densely and with higher contact surface area, e.g. flakes or whiskers (elongated rectangular prisms), minimize this resistance and significantly increase conductivity. Close-packing of boron nitride (BN) flakes, at local volume fraction >90v% within assembled stripes, would allow overall conductivity $k > 10$ W/m.K (a target for thermal interface and heatsink materials [68]) at global particle loading $\phi < 20$v%, preserving mechanical flexibility and low viscosity [69].

In experiment, however, acoustically patterned boron nitride flake samples have lower than expected conductivity (open symbols in Figure 3.9C): at 12v% loading, patterned samples have conductivity of 1.22 W/m.K in the parallel direction and 0.69 W/m.K in the perpendicular direction, and unpatterned samples have 0.91 W/m.K. While the unpatterned samples have very similar conductivity to the carbon fiber composites, the patterned composites have much lower enhancement due to patterning and a much lower anisotropy ratio. The cause for this lower-than-expected conductivity for BN flakes is poor alignment, inefficient packing, and low contact surface area density of flake-shaped particles in standing pressure waves (whereas rods align and stack efficiently), as demonstrated in the following sections. To understand the mechanisms causing this poor alignment and stacking, we develop models of the acoustic driving forces on particles with differing geometries to compare to experimentally observed microstructure. These insights guide

strategies for leveraging acoustic forces and torques to improve packing and to further improve conductivity.

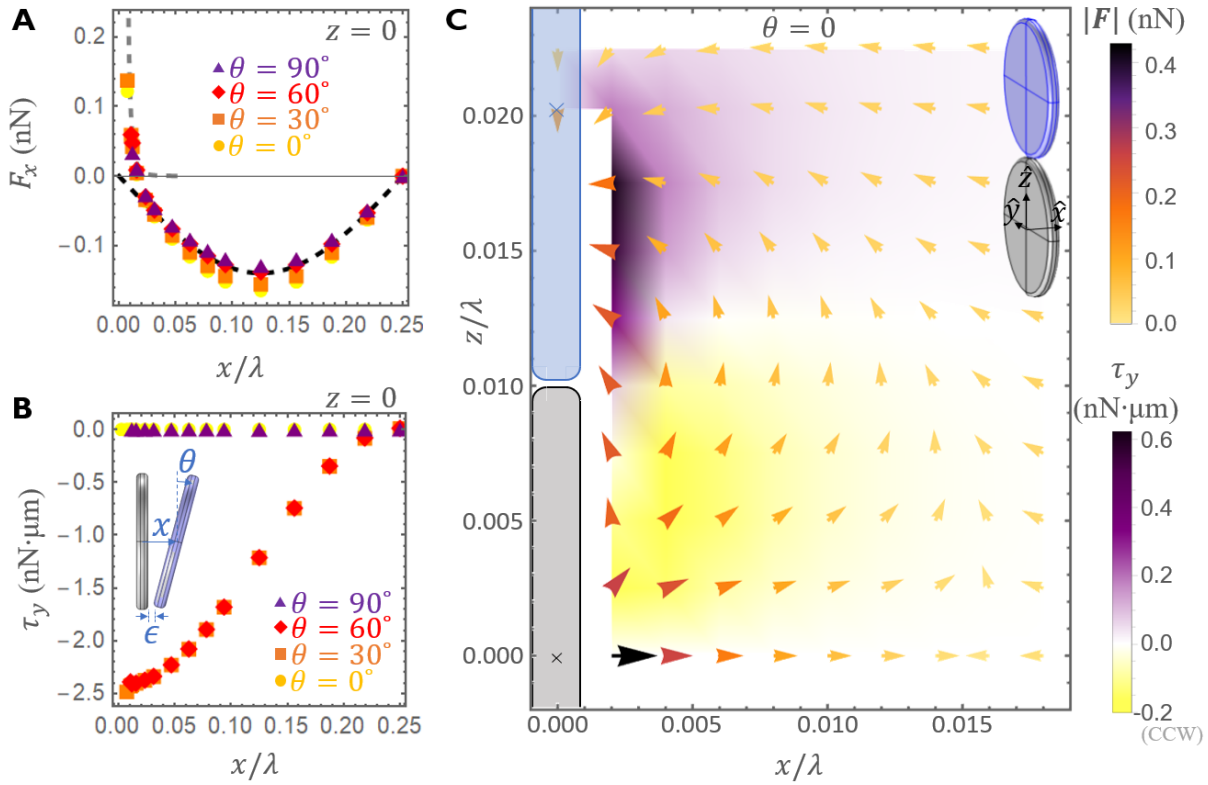

Figure 3.10: **A** Total force and **B** torque on a disk-shaped probe particle (colored blue in inset) due to the background pressure field as well as the field scattered by a source (gray) particle located at the origin at various in-plane angles θ from the nodal plane, spanning the distance between the low-pressure node ($x = 0$) and the antinode ($x = \lambda/4$). For reference, King's formula[34,84] for the primary radiation force (black dashed line) and the secondary force[34] (gray dashed line) on a sphere with equivalent volume are plotted. The minimum clearance ϵ between particle surfaces is 0.5 μm. Torques for $90° < \theta < 180°$ have opposite sign, and are symmetric about $x = 0$ and $x = \lambda/4$. **C** Total acoustic force (arrows) and torque (colormap; positive torques are clockwise), with both particles oriented parallel to the nodal plane ($\theta = 0$). The stable equilibrium configuration is illustrated as an inset. Disks have diameter 10 μm and thickness 0.833 μm to model BN flakes.

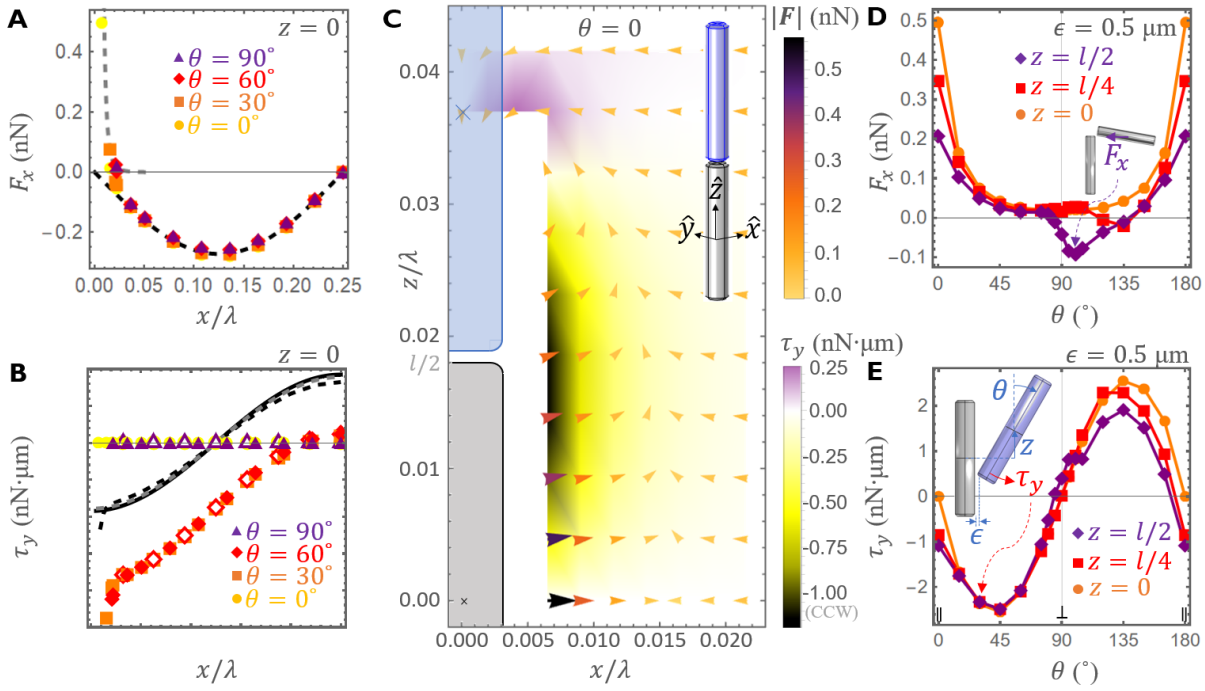

Figure 3.11: **A** Total force on a probe rod (colored blue in insets) due to the background field and scattered field due to a source (gray) rod at the origin, compared to King's formula for a sphere with equivalent volume (black dashed line) and the secondary force for spheres (gray dashed line). **B** Total torque (open markers for a single, isolated probe particle) compared to Lima's 2020 analytical expression (gray dashed line) for a spheroid with the same dimensions[113] with $\theta = 30°$, a projected-area analytical model[112] (black line), a constrained-sphere model comprising six 3 μm diameter spheres[53] (black dot-dashed line). Torques for $90° < \theta < 180°$ have opposite sign. **C** Total acoustic force (arrows) and torque (colormap; positive torques clockwise). Rods have diameter 3 μm and length 18 μm to model carbon fibers used in experiment. **D** Total force and **E** torque on particles constrained to have surface clearance $\epsilon = 0.5$ μm, at various particle offsets z, as a function of in-plane angle θ.

Acoustic driving forces for alignment and stacking of flakes and rods

To determine the driving forces for alignment and stacking of flake-shaped versus fiber-shaped particles, we perform finite element analysis (FEA) to model acoustic forces on particles during acoustic patterning. The force and torque on particles in a standing pressure wave, $p_0 \sin(2\pi x/\lambda)$ with $p_0 = 100$ kPa and wavelength $\lambda = 500$ µm where x is the particle's position, are calculated by modeling flakes as disks with diameter 10 µm and thickness 0.83 µm and fibers as rods with diameter $d = 3$ µm and length $l = 18$ µm (corresponding to the measured aspect ratio of the boron nitride flakes and carbon fibers used in experiment). The particle's properties are matched to boron nitride and the fluid is matched to the photopolymer. These material parameters and the details of the theory and calculations are given in Section 2.3. One particle is kept fixed at the low pressure node (defined as $x = 0$, with the antinode at $x = \lambda/4$), which is the equilibrium position of a single particle, with major axis parallel to the nodal plane ($\theta = 0$, i.e. aligned along the focused stripes in the z direction), the equilibrium orientation. This stationary particle is referred to as the source particle and is colored gray in Figures 3.10 (for disks) and 3.11 (for rods). A second particle, called the probe particle and colored blue, is placed at various positions (x, z) (with fixed $y = 0$ because y is equivalent to z by symmetry) and orientations θ (measured from the z-axis); the forces on this probe particle in these configurations are calculated and plotted in Figures 3.10 and 3.11.

The two contributions to the total force and torque on particles are those due to the background standing pressure wave and the pressure field that arises from scattering between particles. To guide this discussion, these two forces are also plotted for spherical particles (with the same volume as the disks or rods), for which accurate analytical expressions exist, in Figures 3.10A and 3.11A. The force due to the background pressure field, called the primary radiation force, is very similar for spheres (black dashed line[84])

and the rods and disks, aside from a minor dependence on orientation θ (higher force for higher projected area in the wave propagation direction). This force pushes the particles to the low-pressure node (i.e. $F_x \leq 0$). Note that the field and the force are periodic, anti-symmetric about the low-pressure node $x = 0$ and antinode $x = 0.25\lambda$.

Close to the node, $x < 0.04\lambda$, the force due the field scattered off the source particle at the origin becomes significant, and again the force on disks and rods closely follows the analytical form for spheres[34], plotted as gray dashed lines in Figures 3.10A and 3.11A. This scattering force is short-ranged and repulsive between particles aligned along the wave-propagation direction, leading to a positive force that is asymptotic as the particles approach each other along x (as the clearance ϵ between particle surfaces vanishes) As a result, there is an equilibrium probe particle position where the total force crosses zero at $x \approx 0.015\lambda$ for $z = 0$ and $\theta = 0$ (and at slightly larger x for $\theta \neq 0$). This equilibrium spacing between particles in the x-direction is readily observed in experiment under dilute conditions[53] and is a major driver of anisotropy in acoustic particle packing of denser suspensions[34]. This separation is an unstable equilibrium configuration, however, and if the probe particle is displaced vertically ($z \neq 0$) it will be pushed away from this position. Figures 3.10C and 3.11C illustrate the total force on the probe particle when located at various (x, z) positions near the source particle at the origin, plotted as arrows with their bases located at the centroid of the probe particle. The particle is pushed along the contour of the forces to a stable equilibrium position stacked vertically with the source particle in the low-pressure node, as illustrated in the insets of Figures 3.10C and 3.11C. Fibers stack along their axis, whereas disks stack along their edges (both along their major axes). As illustrated in Figure 3.11D-E, if particles become misaligned ($\theta \neq 0$), the total acoustic force and torque push the particle back into alignment (towards $\theta = 0° = 180°$, or to a slight misalignment $165° < \theta < 180°$ for rod centroid offsets of $0 < z < l/2$; for disks this maximum equilibrium misalignment is $0° < \theta < 7.5°$; counter-alignment at

$\theta \approx 90°$ is an unstable equilibrium) before being pushed into the stacked configuration. This scattering interparticle force is thus similar to that on spheres, which is repulsive in the x-direction but attractive in the z-direction[34,87], preferentially forming chains of particles parallel to the focused stripes[34,53].

This driving force for stacking rods along their ends and flakes along their edges, however, drives denser packing of rods compared to flakes. Close-packing of rods and maximal contact surface area requires stacking along along their ends[111], which is encouraged by these acoustic forces. Flakes also require stacking along their faces for the densest packing and contact surface area[150], but the scattering forces drive the opposite behavior, encouraging stacking along edges instead. This is likely a main cause of the lower conductivity of flakes compared to carbon fibers observed in Figure 3.9C — this hypothesis will be examined by characterizing the microstructure within focused stripes in the next section.

A second important determinant of particle alignment and packing (and thus conductivity) is the timescale for particle alignment within the context of assembly dynamics. As shown in Figures 3.10B and 3.11B, the acoustic torque serves to align both rods and disks along the nodal plane ($\theta \to 0$ i.e. parallel to the focused stripes) unless the particle is very close to the pressure antinode ($x/\lambda \gtrsim 0.22$). (Theoretical models for the acoustic torque on fibers[53,112,113], plotted as black and gray curves in Figure 3.11B, predict similar alignment behavior, but there are inaccuracies in the onset of alignment of short rods in these analytical models; the causes and consequences of this discrepancy, as well as experimental validation of the present FEA results, are detailed in Section 3.2.5.) As a result, both disks and rods will align with $\theta \to 0$ — the timescale for this rotation, however, must be considered to determine if this alignment occurs quickly enough to order dense suspensions of particles before they collide and become pinned and jammed during concentration at the node.

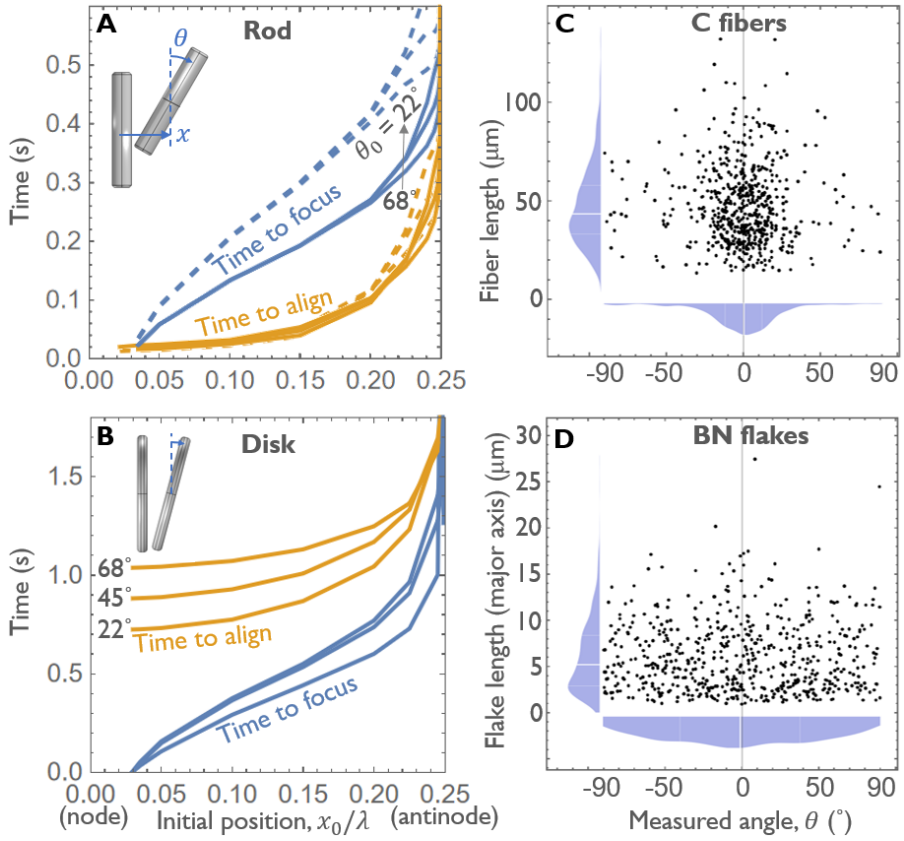

Figure 3.12: **A-B** Simulated time for rods (solid lines: dia. 3 µm, length 18 µm, matched to experiment; dashed lines: dia. 2.4 µm, length 14.4 µm, matched to volume of disks below) and disks (dia. 10 µm, thickness 0.83 µm) with initial positions x_0 and initial orientations θ_0 to focus to the low-pressure node ($x = 0 + 0.03\lambda$), and the time for the particle to align along the nodal line ($\theta = 0.99 \times 90°$), illustrating that rods align before reaching the pressure node whereas disks reach the node before aligning. **C-D** Measured lengths and angles of acoustically focused carbon fibers (dia. 7.5 µm, length 40 µm) and boron nitride flakes (dia. 12 µm, thickness 1 µm), both at 12v% in HDDA (measured with image analysis for fibers and CT scans for flakes, with plotted points downsampled randomly for clarity), illustrating poor alignment of flakes compared to rods. Quartiles are marked as white lines on the histograms.

Simulated particle trajectories which balance these calculated forces with drag and inertia (as detailed in Section 2.3) reveal that disks reach the equilibrium x position before rotating into alignment and are thus misaligned when they collide with the assembled stripe, in contrast to rods which align quickly, much before reaching the equilibrium position. This discrepancy holds true over the entire range of initial positions and orientations, as plotted in Figure 3.12A-B[112]. The drag forces are stronger relative to the acoustic torque for disks because of their higher projected area in the focusing direction. To decouple the effect of the smaller flake size, rods with equivalent volume to the flakes are plotted as dashed lines in Figure 3.12A-B, demonstrating that particle geometry, not size, differentiates the behavior of the flakes and fibers. For longer rods with diameter 3 µm and length 36 µm, this gap narrows such that the time to align is approximately 0.05 s slower for all x_0, and the time to focus is approximately 0.01 s faster. This discrepancy in rotation versus translation time is a second major driving force for poor alignment and packing of flake-like particles, which likely explains the lower conductivity of patterned BN flake assemblies versus carbon fibers observed in experiment. The next section investigates this alignment discrepancy in experimental materials.

In summary for this section, the acoustic driving force aligns the major axis of rods and flakes along the focused stripes, though the flakes rotate slowly and are still misaligned by the time they reach the low pressure node whereas rods align much quicker. When approaching another particle near the low pressure node, the scattering forces will stack the particles within the low pressure node such that rods stack along their axes while flakes stack along their edges. How this driving force impacts the structure of experimentally patterned composites, and the consequences this has for conductivity, is investigated in the next section.

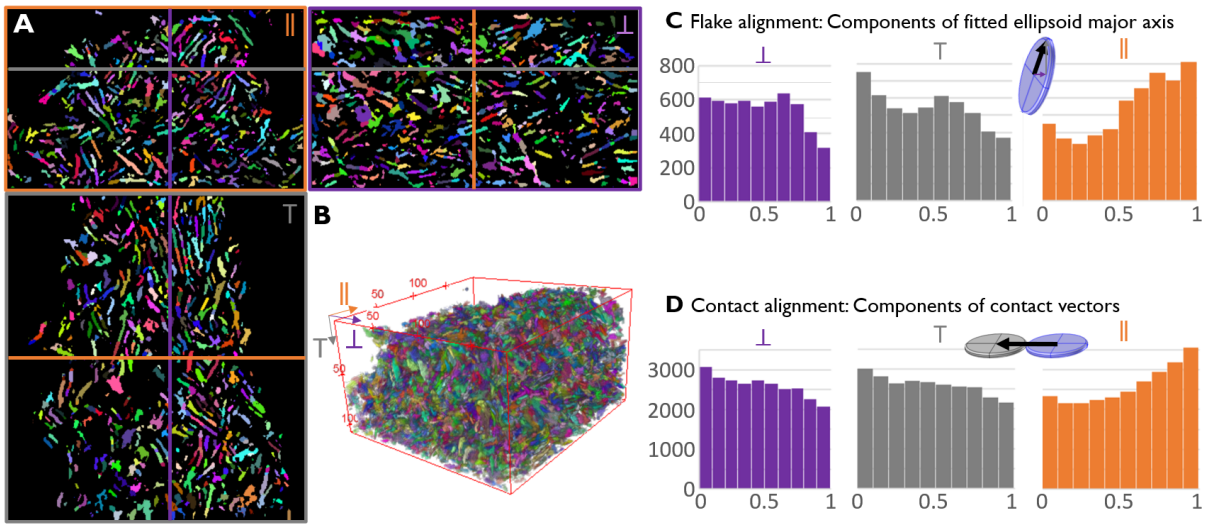

Figure 3.13: **A** Orthogonal views and **B** 3D view (units of µm) of X-Ray computed tomography scan of a 12v% BN focused line, with flakes segmented and labeled with random colors. **C** Histograms of the components along each direction of the flakes' orientation, measured as a unit vector along the major axis of a fitted ellipsoid, showing preferential alignment along the direction parallel to the focused stripes. **D** Histograms of the components of center-to-center vectors for contacting flakes, showing preferential stacking of flakes along the parallel direction.

Microstructure

To determine if the calculated acoustic forces on rods and disks indeed drive differences in the alignment and stacking of filler particles, we now characterize the microstructure of experimentally patterned materials. First, we measure the in-plane alignment of both C fibers and BN flakes within assembled stripes, as shown in Figure 3.12C-D. BN flakes indeed have poor alignment, with a wide distribution of angles, $\theta = 0 \pm 50°$, with respect to the focused stripes, whereas C fibers align relatively well, $\theta = 0 \pm 25°$. These results are determined by fitting ellipsoids to particles in micrographs and CT scans as detailed in the Experimental Methods.

Second, to determine if rods and flakes stack differently, we more thoroughly analyze the 3D configuration of particles. By segmenting the particles in the CT scans (Figure 3.13A-B) and fitting an ellipse to each particle, the orientation of each flake is calculated using the direction in which its major axis points. A histogram of these normalized direction vectors is plotted in Figure 3.13C, finding that a large proportion of flakes have their largest components parallel to the focused stripe, indicating preferential alignment along the stripe, though this alignment is weak, as noted above, because a large minority of flakes do not point along the parallel direction at all (46% have 3D polar angle >90° with respect to the parallel direction, and only 15% have angle <30°). Similarly, a histogram of the vectors between contacting flakes reveals preferential stacking along the parallel direction as well. This alignment and stacking is opposite to that expected in a uniaxially compressed assembly of anisotropic particles without external (i.e. acoustic) body forces, which instead tend to contact along the compression direction[103] (here the $\perp$ direction), indicating that the acoustic scattering forces dominate interparticle interactions and give rise to the observed alignment behavior. As a result of this weak alignment, the volume fraction within a focused stripe is measured to be 25v%, whereas the expected random

close packing limit for disks with this aspect ratio is 35v%[150]. The flake packing achieved here is less dense than random close packing because of the driving force for stacking along edges instead of the stacking along faces needed for high local packing fractions[150]. In sum, flake particles indeed align and pack poorly in standing waves because of low acoustic torque relative to drag and because of interparticle interactions that encourage stacking along edges instead of faces. This inefficient alignment and contact behavior explains the low measured conductivity of patterned BN flake composites.

Fibers, on the other hand, are driven to align and stack along their axes, which is reflected in their higher measured alignment and conductivity. To further improve thermal conductivity, the mechanisms detailed here can be leveraged for higher local packing fractions by optimizing particle geometry. Elongated particles, which align quickly and stack end-on-end are optimal for packing, and particles with flat faces that stack with high contact surface area will increase conductivity by minimizing contact resistance. Boron nitride whiskers (elongated fibers with rectangular cross-section) would be ideal for this application, and will be the subject of future studies. Using these particles, thermal conductivity surpassing 10 W/m.K is is predicted by the models developed above at particle loading below 20v% if close packing of flakes[69] is achieved within focused stripes.

3.2.4 Conclusions

We successfully demonstrated a material-agnostic approach to manufacture composite materials with patterned filler particles by integrating acoustophoresis into stereolithographic 3D printing. By controlling microstructure via alignment and concentration of conductive particles into efficient percolated networks, filler particle utilization in thermal transport networks increased from 25v% in unpatterned materials to 75-95v% along the stripes of patterned composites. This patterning process enables printing components

with anisotropic heat distribution networks for redirecting heat away from hot spots in electronics. Furthermore, simulations of the acoustic assembly of filler particles with varying geometry corroborated experimental findings of significantly more efficient alignment and packing of fibers versus flakes within assembled stripes (and, as a result, higher conductivity), providing a mechanistic understanding of the physics behind filler particle assembly using acoustic fields. This comparison of simulation and experiment revealed that the timescale for elongated particles like fibers to rotate into alignment, relative to translation during concentration at the low-pressure nodes, is conducive to dense packing of rods but not flakes. The interparticle forces arising from scattered pressure waves also promote stacking of fibers along their axes, the close-packed configuration, whereas they drive flakes to stack along their edges, when close-packing requires stacking along their faces. Using this knowledge, further improving conductivity in acoustically patterned materials requires optimizing the geometry of filler particles, with whisker-shaped particles being the most promising candidate.

3.2.5 Experimental Validation of FEA Torque

The strong acoustic alignment of rods is in agreement with previous finite element simulations on single 2-dimensional rods[116] but in disagreement with analytical solutions for cylinders[112] (plotted as the black line in Figure 3.11A) and spheroids[113] (gray dashed line). The analytical solutions predict strong counter-alignment (i.e. positive torque, rotating fibers clockwise into alignment along the x axis) instead of negative torque for $x/\lambda > 0.125$, as well as weaker torque for $x/\lambda < 0.125$. This discrepancy is likely due to the inclusion of bending modes of high aspect ratio particles in our finite element analysis method, as well as the inclusion of damping due to scattering from elastic solids. Another model with very similar behavior to the other analytical expressions constructs rods as

a chain of constrained spheres[53], which allows calculation of interparticle scattering effects[34] between rods (plotted as the black dashed line), showing similar short-range scattering to the finite element analysis but dissimilar sign change behavior (again at $x/\lambda = 0.125$ instead of 0.22). The sign change in torque at larger x in the finite element model indicates that acoustic patterning more strongly aligns fibers than previously understood (with higher torque magnitude and earlier onset of rotation), setting the stage for improving properties via particle alignment and close packing.

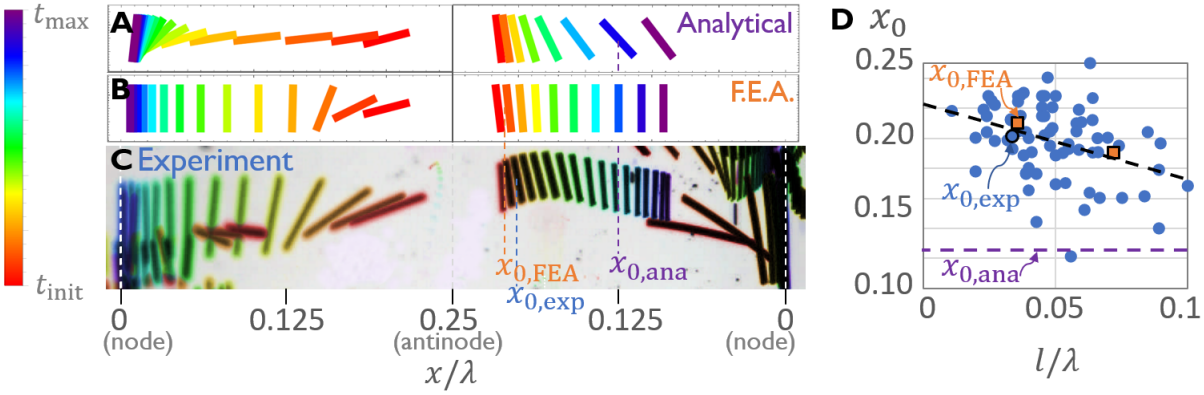

Figure 3.14: **A** Rod trajectories colored by time-step, for the finite element analysis compared to the **B** projected-area analytical model[112]. **C** Superposed image frames from a video recording of rod focusing in experiment, with carbon fibers colorized by time step (initial position in dark red), illustrating the estimated position x_0 where the torque becomes negative (aligning fibers along the z direction). Full image given below. **D** Scatter plot of x_0 values versus fiber length as measured in experiment (blue circles), with linear fit (black dashed line), compared to the finite element prediction (orange squares) and analytical prediction (purple dashed line). The error for experimental points, not shown for visual clarity, is less than 0.01 in both axes.

Because particle alignment is critical to maximizing contact surface area and, thereby, conductivity, we experimentally measure fiber rotation behavior to validate the finite element analysis as shown in Figure 3.14. Fiber trajectories illustrated by superimposed video frames of carbon fibers in a standing wave in HDDA are compared to modeled trajectories. Rods only slightly counter-align very near the antinode, as seen in both the finite element analysis and experimental trajectories plotted in Figure 3.14 (rod on

the right; full image provided in Figure 3.15), instead of rotating perpendicular for all $\lambda/8 < x < \lambda/4$ as predicted by the analytical models. To quantify this behavior, a scatter plot of the experimentally observed positions where the torque on fibers changes sign, x_0, is given in Figure 3.14D (blue circles), fitting a linear trend (black dashed line) that coincides with the x_0 predicted by the finite element analysis (orange squares), whereas the analytical models predict $x_0 = \lambda/8$ (purple dashed line), which is outside of two standard deviations of the mean of the experimental x_0. (The variation among experimentally observed x_0 is likely due to acoustic or hydrodynamic interparticle interactions.) Thus, the experiments validate the finite element analysis and suggest that the analytical models are inaccurate for short fibers. The experimental trend and finite element calculations suggest that x_0 approaches 0.125 as fiber length approaches $\lambda/4$, which is the experimentally observed threshold for fiber counter-alignment[28,112,117], suggesting that the analytical models may be more accurate for longer fibers. The FEA torque scales with $l^{3/2}$ and d, in agreement two-dimensional analysis[117].

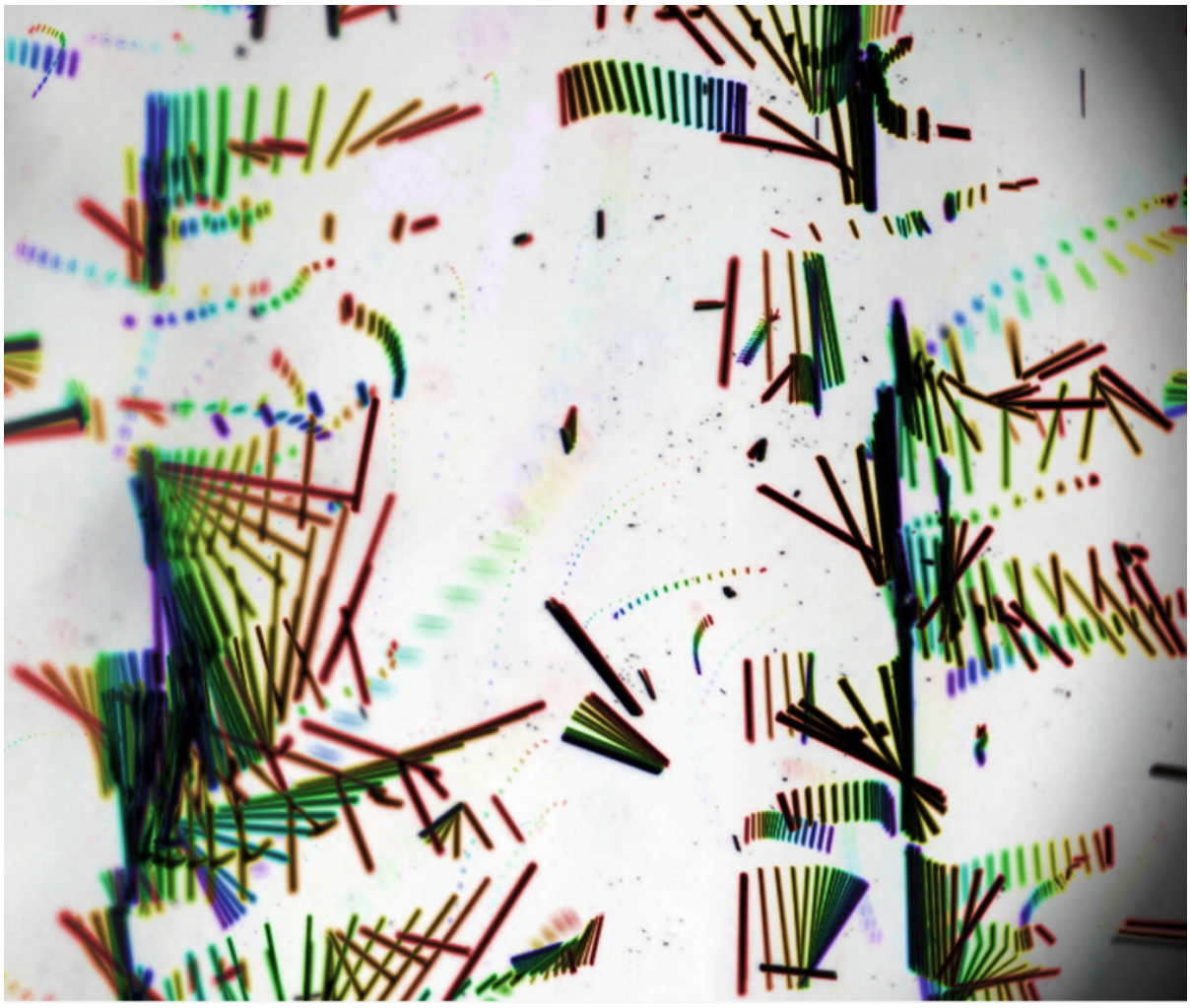

Figure 3.15: Full experimental rod trajectory image used in Figure 3.14, illustrating the positions of the low-pressure nodes.

Chapter 4

Engineering multifunctionality in composites

Using acoustic patterning to increase conductivity of composites at low filler volume fractions introduces an opportunity to make use of the remaining volume in the material to simultaneously improve other functionalities. Such materials with multiple functionalities are in high demand mainly because in many applications materials undergo mechanical deformation while serving electrical, thermal, or ionic functions, sensing, fluidic transport, energy storage, etc. In the applications investigated in this work, thermally conductive materials must be strain tolerant to avoid damage during thermal cycling (due to thermal expansion and contraction) and flexible electrically conductive composites (especially if 3D printable) fill a gap in emerging flexible electronics and soft robotics applications.

Acoustic patterning in particular is amenable to creating multifunctional materials because of its material agnostic nature, allowing novel combinations of composite phases, and because it creates anisotropic particle patterns that improve multiple functionalities in different regions of the material. In the first section of this chapter, the mechanical flexibility of patterned conductive materials is investigated by using flexible polymer matrix

materials. These soft matrices effectively encapsulate the conductive particle stripes and absorb stress during deformation, allowing high cyclic strain tolerance without damage or losses in conductivity compared to conventional unpatterned materials. In unpatterned materials, by contrast, high filler loading and random filler distribution leave the matrix phase with many broadly distributed inclusions and necked filaments between particles that are prone to rupture. In the patterned materials, however, continuous uninterrupted polymer regions absorb stress and encapsulate the highly included densely packed particle structures (where damage is likely but in many cases may screen stress and improve properties via favorable particle rearrangements), preventing widespread cracking and delamination of particles. In the second section, we investigate how the packed particle assemblies themselves respond mechanically to applied loads, and how this affects material properties.

Other, more exotic applications make use of particles or matrices that themselves are structured to have advanced functionalities, allowing access to new combinations of properties. A particularly promising application of acoustic patterning is assembly of multimaterial, nano- or micro-structured particles, because acoustic forces are relatively insensitive to heterogeneous particle compositions. Such hierarchical assembly is proved in concept in the third section of this chapter, using fabricated microdevices as the particle phase in a sacrificial matrix phase. Application of orthogonal fields is also demonstrated in the third section to expand the degrees of freedom of particle manipulation for enhanced control over structure and properties.

4.1 Mechanical flexibility and electrical conductivity

In flexible conductive composites there is a well-documented trade-off between electrical conductivity and mechanical flexibility that currently limits the viability of 3D printed

flexible conductors, especially in the complex geometries encountered in 3D printing demanding strain tolerance[5,74,75]. The conductivity of conventional percolated composites has a power law relationship with filler loading, increasing as more particle contacts are formed[6]. The strain tolerance of composites, however, decreases rapidly with the added inclusions in the binder matrix[6,74]. As a result, highly flexible unpatterned composites must sacrifice conductivity[76]. This constraint is particularly important in 3D printed materials without a supporting substrate to absorb stress. As a result, cost-effective flexible electronic devices are still out of reach.

Printed conductive composites are typically made with silver or carbon micro- or nano-particles. High conductivity requires a high volume fraction of conductive filler particles (typically 10-85% by volume), which decreases flexibility so that conventional conductive inks exhibit large (20-600%) changes in conductivity with bending strain, as well as approximately linear losses in conductivity with cyclic loading as particles separate or delaminate, even when supported by a flexible substrate[5,77–79]. For 2D printed inks, prestretching the substrate improves flexibility by forming serpentine buckled patterns when relaxed[5], but this approach is infeasible for integrating into 3D printed components. High filler loading also poses a problem for printability since higher volume fractions exacerbate clogging and increase viscosity[66,151,152]. One conventional solution to this filler loading problem is to print at low loading and then burn off the polymer binder after printing to increase particle contact density, which works for brittle materials but is incompatible with many soft matrix or substrate materials desirable for flexibility[132]. An extension to this solution is sintering conductive particles (at higher temperatures than polymer burn-off), which can improve flexibility as well as conductivity. The temperatures required ($> 200°C$), however, are incompatible with most soft materials of choice, so that this sintering approach is better suited for printing electrical circuits on rigid moving substrates rather than flexible substrates[66]. Localized sintering using laser or microwave

spot heating may be compatible with 3D printing soft materials, although these approaches would introduce complex post-printing steps to an already costly and complex process of printing conductive and support inks with multiple nozzles[56,153]. Another approach to printing flexible electronics is liquid eutectic metal infiltrated channels in soft materials, which have a promising combination of stretchability and conductivity, but $> 0^\circ$ C freezing temperatures, leaking, and safety concerns (e.g. Ga leaching), in addition to methods for integration into complex 3D printed geometries, need addressing[154]. Soft-substrate 2D lithographic techniques are successfully tackling flexible chips[5,155] but are infeasible for large-area electrodes or device-scale interconnects[74]. Thus there is a technology gap in materials with capabilities for orthogonal control over multiple functionalities and integrated electrical circuits, which would circumvent expensive and time-consuming wiring steps[64,66]. Filling this technology gap would substantially improve the cost effectiveness and design complexity of 3D printed soft electronic components, a major boon for applications including soft robotics[156] and wearable electronics[157].

Here we present an approach for bypassing the trade-off between conductivity and flexibility in composites by assembling filler particles into percolated networks within a flexible polymer matrix using acoustic fields. These patterned materials, in addition to having high conductivity (Section 3.1) are also flexible, withstanding at least 500 cycles without losses in conductivity and exhibiting small ($< 5\%$) fluctuations in conductivity when bent to submillimeter radii.

In patterned composites formed with flexible matrix material (UV-cured 1:1 methyl:cyclo hexyl acrylate + 2wt% butanediol diacrylate, glass transition temperature 14.5°C), conductivity values in the undeformed state are unchanged from the rigid HDDA composites (investigated in Sections 3.1 and 3.2), but the composites are flexible as shown in Figure 4.1. In a bending test, cycling between bending strains of $\epsilon = 22\%$ (mandrel radius 0.7 mm, with the particle pattern on the outer face so that it's in tension) and $\epsilon = 0\%$ at

a rate of 0.5 Hz yielded nearly constant conductivity over 500 cycles, with conductivity recovering to ∼90% of the pristine as-printed value (34 S/m) in each cycle. Additionally, conductivity changes only 5% on average within cycles. This strain tolerance is due to the confinement of stiff conductive particles joined by freely rotating and sliding contacts within a compliant, stress-absorbing matrix. In contrast, conventional silver conductive inks which rely on silver or graphene micro-flakes exhibit large (20-600%) changes in conductivity with bending strain and roughly linear conductivity loss with cycle number [77–79]. As shown in Figure 4.1E, because dispersed-fiber composites require much higher loading for conductivity, they have both lower conductivity and flexibility, cracking at low strains. Softer polymer formulations (with lower glass transition temperature or lower cross-linking density) resulted in slower recovery times and lower cyclic durability.

These patterned materials fill a research gap for flexible conductive composites that can be 3D printed into freestanding 3D shapes. In applications like soft robotics and wearable electronics, this method can be used to print the electrical interconnects in the regions of the component that must withstand high bending strain. Furthermore, driving particles into contact within assembled patterns and encapsulating them in a continuous soft polymer matrix provides a novel mechanism for high strain tolerance in conductive particle networks.

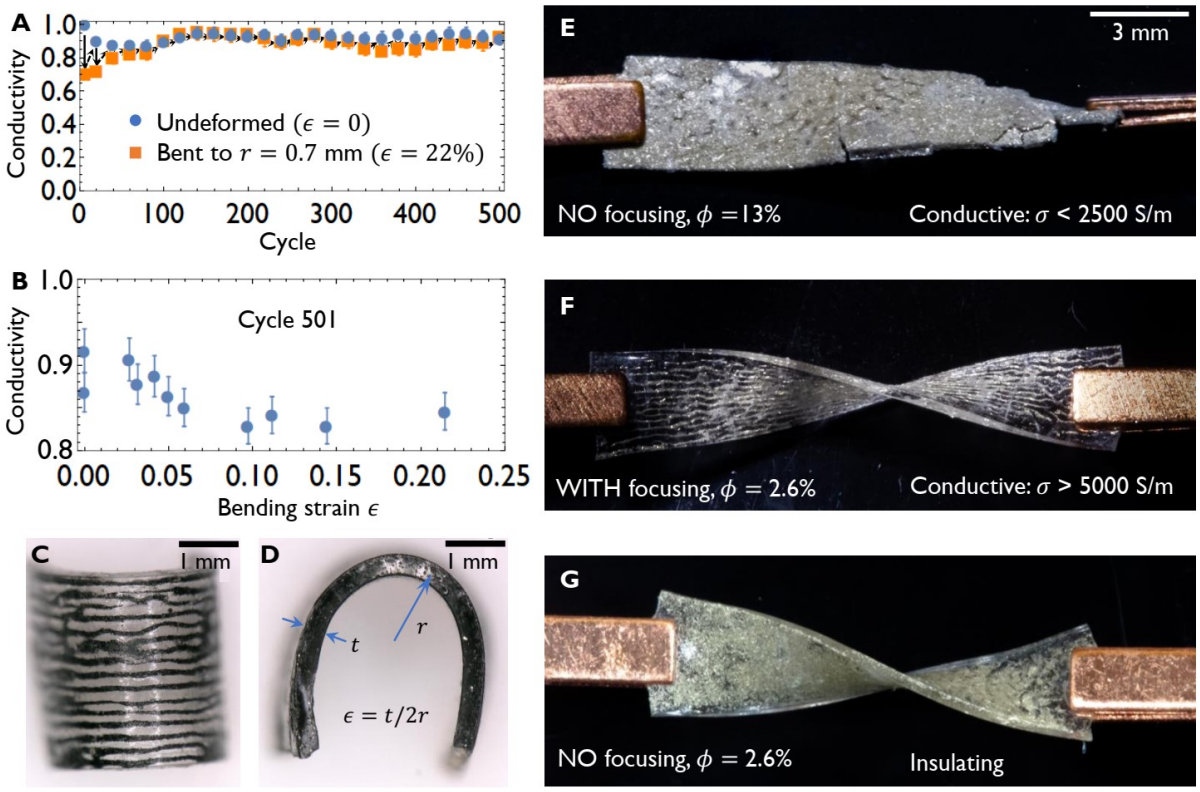

Figure 4.1: **A** Conductivity of elastomeric patterned composites after bending cycles to $\epsilon = t/2r = 22\%$, where $t = 300$ µm is the composite thickness, as a fraction of the pristine conductivity (34 S/m). **B** Conductivity within a single cycle (#501). **C,D** Micrographs of a 2.6v% carbon-fiber elastomeric composite. **E,F,G** Photographs of silver-coated fiber elastomeric composites, twisted to showcase the gains in flexibility and conductivity via acoustic patterning. In **E**, the left edge of the composite is a fractured edge, having failed completely at a 90 degree twist before being photographed.

Experimental Methods

Flexible composites are made using 1:1 methyl:cyclo-hexyl acrylate monomers (both Sigma Aldrich, >97%) with 2wt% butanediol diacrylate crosslinker (Sigma Aldrich, 90%) and 2.5wt% photoinitiator. Silver-coated fiber composites are made using silver-coated glass rods with 150 µm nominal mean length and 10 µm nominal diameter (Potters Conduct-o-fil AGCLAD12).

Bending tests were performed by clamping both ends of patterned fiber-elastomer composite samples with 2.5 mm clamps and cementing them in place with silver-filled

epoxy (Chemtronics). The clamps were held in place with micrograbbers on sliding tracks and wired to a multimeter. The elastomer composites were then bent around an insulating mandrel of known diameter and the resistance was recorded. The cycle frequency was 0.5 Hz, measuring resistance at the flat and bent states.

4.2 Mechanical response of packed particle assemblies

To better understand the evolution of particle contacts during deformation within the packed particle assemblies, particle-level in-situ characterization is needed. This section utilizes fluorescence confocal microscopy to track particles during deformation of packed particle assemblies, building an understanding of the structural evolution of patterned particles during deformation which can be used to optimize functional properties in multifunctional composites that undergo deformation. This section investigates how the particle packing density evolves when a pillar of close-packed spheres is compressed in a liquid matrix, approximating the response of spheres within acoustically assembled stripes in the limit of a compliant matrix (i.e. isolating the response of the particles and minimizing the contribution of the matrix).

The composites studied in the previous section (Section 4.1) utilize a matrix material 8-9°C above the glass transition temperature and, according to simulations on spheres (Figure 2.5 and 2.8), have a very similar packing fraction to the experiments in this section (near the random close-packing limit of 0.64). The particle assemblies are similarly unconfined, with free surfaces except where the loading piston or clamps contact the particle pillar, which allows particles to freely change volume fraction. Both systems are also athermal and employ quasistatic loading (with shear rate faster than the relaxation

rate, i.e. with negligible thermal activity so that annihilation of excess free volume via thermal rearrangements is much slower than the shear-driven generation of free volume). Thus the deformation mechanisms presented here provide useful insights into the behavior of the patterned composites, as will be discussed below.

Comparisons are limited, however, by the difference in particle and loading geometry, with the bending experiments in the previous section using fibers and the present compression experiments using spheres, and compliance of the matrix, with the soft polymer in the previous section close enough to the glass transition to be rubbery or highly viscous whereas the acrylic spheres are suspended in an index-matched liquid with low viscosity. Aligned fibers compared to spheres have anisotropic mechanical response where dilation is discouraged along the axis of the stripes and fibers, suggesting weak flexural strength off the axis of the stripes and confining rearrangements to perpendicular directions. The higher viscosity matrix slows and diminishes the magnitude of plastic deformation in shear bands, possibly limiting their extent and yield stress thresholds but likely not altering the underlying mechanism. On the interior of the bending neutral axis of the patterned composites, compression and shear banding are likely, but the mechanical response in other regions of the focused particle patterns are not modeled by the present pillar compression test. Further experiments are needed, using the experimental methods and characterization metrics presented in this section, to fully understand the structure evolution of patterned composites during deformation.

These methods may also be used to study structural evolution during acoustic assembly, before curing the photopolymer, since the details of packing fraction and particle contact anisotropy are critical to functionalities like thermal and electrical conduction (as discussed in the previous chapters). In particular, the particle tracking methods developed in this section will enable future studies of the pattern densification strategies discussed above in Section 3.2. A practical constraint on these future experiments is matching the refractive

index of the particles and matrix material (while maintaining low viscosity—silica beads in a glycerol-water-ethanol mixture titrated in a photospectrometer to quantify refraction minimization plus fluorescent dye is a promising candidate; matching cured polymers is more difficult but may be accomplished via tuning the degree of polymerization) and handling rapid 3D image stack acquisition. The results of this pillar compression test cannot be directly related to the simulations of acoustic assembly (Section 2.1), because that system utilizes body forces instead of external loading and involves inter-particle forces that induce rearrangements (i.e. free volume relaxation) approximately three orders of magnitude faster than the shear rate (Figure 2.8) whereas the present experiment is quasistatic. Thus while the methods developed in this section can potentially be used to investigate the acoustic assembly process itself for direct comparison to the simulations of Chapter 2.1, the present pillar compression experiments are not directly comparable to that process. As a final comparison, however, this system has close parallels to metallic glasses, wherein colloids approximate atoms in the amorphous structure of the glass, drawing parallels that help one understand the mechanistic behavior of both systems.

In this section, compression experiments of colloidal pillars are reported in which the evolution of a shear band is followed at the particle level during deformation. Quasi-static deformation results in dilation and anisotropic changes in coordination in a localized band of material. Additionally, a transition from solid- to liquid-like mechanical response accompanies the structural change in the band, as evidenced by saturation of the packing fraction at the glass transition point, a diminishing ability to host anelastic strains, and a rapid decay in the long-range strain correlations. These results suggest that shear banding quantitatively resembles a localized, driven glass transition.

Comparing this behavior to the bending tests performed on acoustically patterned composites in the previous section (Section 4.1) suggests that a concentrated region of particles dilates slightly under stress, possibly lowering particle contact density (and

thus conductivity), but that this dilation is bound by the glass transition and confined within shear bands spanning only ~ 10 particles, limiting losses in macroscopic network continuity. This limited breaking of particle contacts may correspond to the small observed drop in conductivity within the first cycles. Particle rearrangements, moreover, made possible in localized dilated regions like the fluidized shear bands found here, may result in slight variations in conductivity between loading cycles, as is observed in the subsequent recovery of conductivity (perhaps as particles rearrange into a better-aligned, lower-energy configuration) and minor variations between loading cycles.

The experimental measurement and a portion of the data analysis (namely, the coordination and initial strain correlation analyses) and writing in this section were performed by Daniel Strickland and collaborators at the University of Pennsylvania, and this work was previously published in *Physical Review E*[80]. The author's contribution and the focus of this work in the context of this dissertation is analysis of the particle motion, including detailed metrics of subtle structural changes and understanding of strain distribution in the context of deformed particle assemblies, and a portion of the writing.

4.2.1 Introduction

Shear banding—the irreversible localization of strain in thin bands of a solid driven beyond its yield stress—is a feature common to disordered solids. Shear bands are observed in both "hard" disordered solids, where atomic forces dictate the energy of the system[158,159], and in "soft" disordered solids, whose behavior is governed by weaker inter-particle forces[160–162]. Also common to both hard and soft disordered solids is a glass transition, whereby decreasing the temperature, increasing the particle number density, or some combination thereof, results in a dramatic slowing of the dynamics in comparison to the supercooled liquid[163–166]. The commonalities in plasticity and glassy dynamics

found in a diverse set of disordered solids have motivated a search for unifying physics. Specifically, the interpretation of shear banding as a localized, driven glass transition remains controversial.

Numerical and experimental studies support a connection between mechanical yield and the glass transition. Metallic glasses (MGs) exhibit shear bands and a temperature-dependent yield stress when deformed plastically at temperatures well below their glass transition temperature T_g [158,159,167]. Equating the mechanical work done in the formation of a shear band and the heat necessary to induce a glass transition [168] results in a scaling of the yield strength with temperature that agrees well with experimental data. Further support for a shear band or glass transition connection is found in the self-similarity of iso-viscosity curves with proximity to the glass transition and magnitude of applied stress [169–172], which is suggestive of an equivalence between the glass transition and stress required for flow. Some studies [169–171], however, do not specify whether plasticity is spatially homogeneous or localized in shear bands, while other studies draw a distinction between shear banding and the glass transition. In experiments on a sheared colloidal glass, Chikkadi et al. [173] find a discontinuity in a dynamical order parameter that distinguishes shear banding from a glass transition, in which the order parameter changes continuously [163]. Similarly, a structural order parameter that segregates pre- and post-yield glasses classifies mechanical yield as a first-order transition [174]. Others have delineated between the glass transition and mechanical yield by contrasting the microstates induced by strain and increased temperature [175] and anisotropy of dynamical correlations [176], which are different for the thermal and mechanical transitions.

While it appears that mechanical yielding in disordered solids shares some characteristics with the glass transition, the extent of the correlation is not agreed upon. Furthermore, the microscopic details of shear bands as they mature to macroscopic localization has yet to be elucidated. In this section, we report on uniaxial compression experiments

of colloidal pillars. Unlike other studies on deformed colloidal glasses, our specimens are free of confining boundaries that may alter the mechanism in which shear banding proceeds[160,161,173,177]. Moreover, the pillar geometry lends itself directly to comparison with compression experiments performed on MGs[178,179]. In the unconfined geometry, dilation is free to occur and any localized softening can proceed unhindered.

During compression, we observe strong localization of strain in a band of the pillar. As deformation proceeds, the sheared region continues to dilate until the packing fraction ϕ approaches the colloidal glass transition, $\phi_g \simeq 0.58$[180], at which point dilation terminates. While the transition in mechanical response bears some resemblance to a melting condition in thermal, atomic systems, we emphasize that our system of colloidal spheres is athermal. We quantify the extent of correlations in strain and find that it decreases as $\phi \to \phi_g$, and find evidence of a diminished capability to support anelastic strain from anisotropic pair distribution functions.

4.2.2 Experimental Methods

The micropillars, of diameter $D_{pillar} \approx 300$ µm, are composed of fluorescent poly(methyl methacrylate) (PMMA) particles of diameter $D_{part} = 3.3$ µm. The micropillars are formed by injecting a suspension of the particles into a capillary tube. Polydispersity of between 6 and 8% in the particle sizes suppresses crystallization, resulting in an amorphous packing. The suspension is dried and re-wetted using cyclohexylbromide (CXB, which matches the index of refraction of the particles) to increase the cohesion between the particles, holding the extruded specimen together. The pillar is then forced out of the capillary tube to form a free-standing compression specimen, which is secured in a fluid reservoir filled with CXB (see Figure 4.2), eliminating capillary forces. Opposing the pillar is a punch affixed to a piston. The top of the reservoir is sealed with a thin piece of coverglass

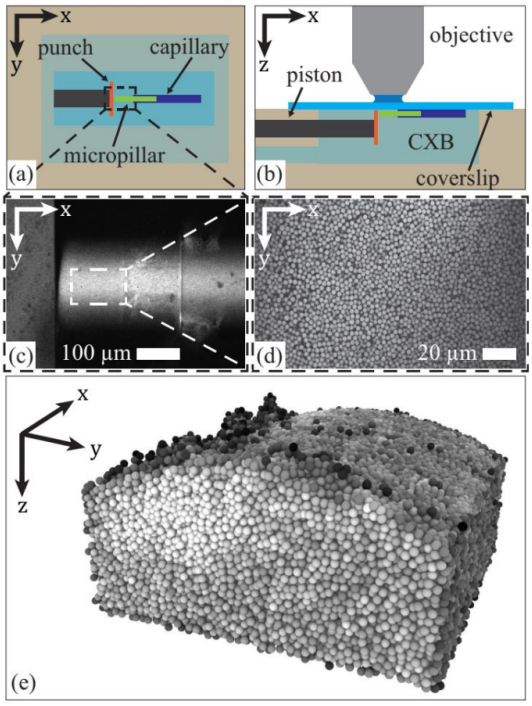

Figure 4.2: A (a) top-down and (b) side view of the experimental setup. The capillary tube containing the colloidal micropillar is secured to a glass coverslip, which is fixed above a fluid reservoir. A piston with a flat punch is used to compress the exposed micropillar. (c) A low-magnification image of an extruded micropillar and the punch. (d) A high-magnification image of the colloidal particles that compose the micropillar. (e) A 3D reconstruction of the pillar section imaged during the experiments using the identified particle positions. The particles are shaded by coordination number, highlighting the curved free surface.

to allow for imaging using a laser-scanning confocal microscope operating in fluorescence mode with an excitation wavelength of 488 nm. The compression experiment proceeds by displacing the punch using a piezoelectric actuator and then collecting a sequence of micrographs of the pillar. Typical displacement increments were 0.6 µm ($\sim 0.2D_{part}$). A computer algorithm identifies the centers of particles in each 3D volume with uncertainty in the particle positions of $\sim 0.03D_{part}$. The analysis proceeds by the same stages as the classic algorithm by Grier and Crocker:[181] image filtering, peak finding, and centroid finding. After particle centers are identified, the positions at each timestep are linked into

trajectories that span the duration of the compression experiment. Particles within three particle diameters of the punch are removed from the analysis, since shadowing during imaging resulted in high uncertainty in their positions.

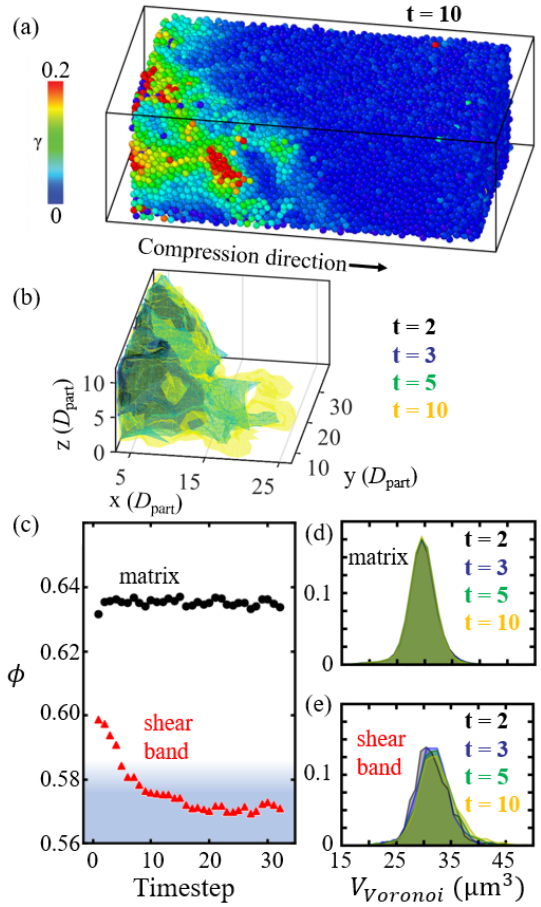

Figure 4.3: (a) The particles in this experiment, colored by shear strain. The shear band is defined as those particles with $\gamma > 0.07$ which have at least three neighbors also with $\gamma > 0.07$. (b) The evolution of the shear band shape over time, visualized as the alpha shape with the smallest alpha radius which encloses all particles in the shear band. (c) The volume fraction ϕ of the shear band and matrix regions, with glass transition indicated with a blue shaded region. (d-e) The distribution of Voronoi volumes in the shear band and matrix at various time steps.

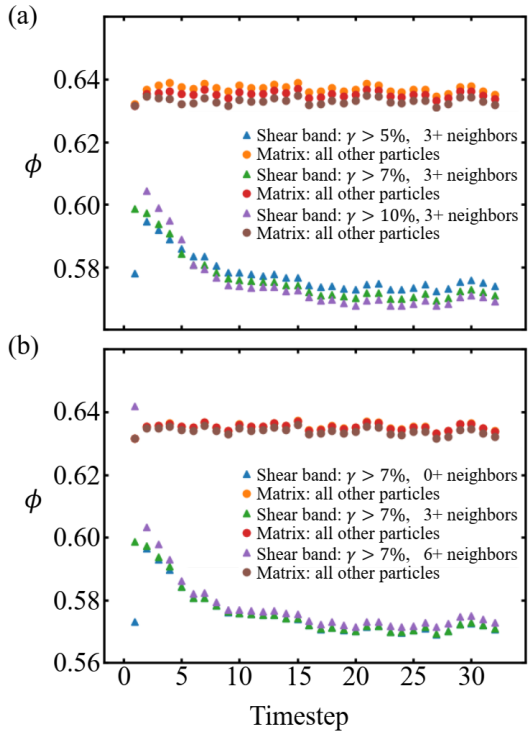

Figure 4.4: Saturation behavior of the volume fraction ϕ in the shear band and matrix using various parameter cutoffs in the shear band definition: (a) variation of the cutoff in shear strain γ, (b) variation of the requisite number of nearest neighbors which also meet the shear strain condition, which serves to filter out non-contiguous sheared particles. ϕ shows little sensitivity to these parameters in this range, except at the first time step where there are few particles in the shear band.

4.2.3 Results and Discussion

Volume fraction

During compression, we observe strain concentrated in a region near the interface with the punch. The shear band is defined here as those particles with shear strain $\gamma > 0.07$ (calculated from the affine deformation tensor as detailed below) that have at least three neighbors which also satisfy the strain threshold. This neighbor condition filters out non-contiguous particles. The effect of adjusting the parameters used in this definition is shown in Figure 4.4: the local volume fraction in the as-defined shear band shows little sensitivity to the shear strain threshold or neighbor filtering except at the first timesteps when the number of particles in the shear band is small. Those particles not in the shear band are termed "the matrix." A timestep t refers to a specific 3D volume with $t = 0$ corresponding to the first volume collected.

The initial packing fraction and Voronoi volume distribution indicate that the shear band was somewhat deformed before the first timestep, so that nascent nucleation of the shear band is not captured in this experiment. However, we are able to observe the evolution of this already-nucleated shear band as deformation proceeds (Figure 4.3b) and find, based on a number of metrics, that its maturation shows a striking resemblance to a localized, shear-driven colloidal glass transition. The first metric is the local packing fraction: the shear band region dilates such that the volume fraction $\phi = 4\pi r^3/(3\overline{V}_{Voronoi})$ decreases to approximately the colloidal glass transition value $\phi_g \approx 0.58$ (Figure 4.3c). We expect our nearly-athermal system to be in a glassy state between $0.58 < \phi < 0.64$, below which it fluidizes and above which it is jammed [182]. We note that the exact value of ϕ_g for hard-sphere colloids remains uncertain and may depend on the polydispersity of the system [180,183,184], thus the saturation point (where further compression does not significantly change ϕ) is either at the transition or in the supercooled colloidal liquid [185,186].

Dilation is also visible in the evolution of the distribution of Voronoi volumes $P(V_{Voronoi})$ (Figure 4.3d and e), which shifts to a higher mean value and develops a large-volume tail. The matrix, on the other hand, has constant ϕ near the random close-packing limit of 0.64 (indicating that our particles have RMS roughness < 0.05[187]).

It has long been recognized that shear transformations in amorphous solids result in an increase in the free volume in the region around the shear transformation[188–191]. In thermal systems, the competition between shear-induced generation and diffusion-driven annihilation of free volume results in temperature- and strain rate-dependent flow behavior[192–194]. At high temperatures and low strain rates, free volume diffusion and annihilation can suppress runaway free volume generation, resulting in homogeneous plastic flow. At lower temperatures and high strain rates, annihilation cannot keep up with free volume generation, and strain localization, or heterogeneous plastic flow, occurs. For our nearly-athermal, hard-sphere system, we expect that the annihilation of excess free volume is insignificant in comparison to the shear-driven generation, thereby resulting in overall dilation with increasing strain[190]. What is striking, however, is how abruptly the dilation process in our experiments terminates at the transition ϕ, at approximately ϕ_g.

Pair distribution function

The dilation and Voronoi statistics measured in the shear band clearly indicate that the structure in the shear band is evolving during deformation. To further describe this change, anisotropic pair distribution functions that discriminate between particle pairs coordinated in different directions, $g(\mathbf{r}) = g(r, \omega)$ where ω is the angle between the loading axis and a selected direction, detect structural changes when symmetry is broken by anisotropic loading[195,196]:

$$g(r,\omega) = \frac{1}{f(r,\omega)}\frac{V}{N^2 dV} \times 2\sum_{i=0}^{N-1}\sum_{j>i}^{N} \delta\left(r - \frac{dr}{2} < r_{ij} < r + \frac{dr}{2}\right) \times \delta\left(\omega - \frac{d\omega}{2} < \omega_{ij} < \omega + \frac{d\omega}{2}\right), \quad (4.1)$$

where V is the total volume and N is the number of particles in the shear band, $dV = 2r^2 dr d\omega$ is the volume element of a spherical shell (at r and with thickness dr) constrained by azimuthal angle ω between the x-axis and the vector separating a given i, j pair (always positive), and δ is the Kronecker delta. Here, $dr = 0.04 D_{part}$ and $d\omega = \pi/10$. $f(r,\omega)$ is the shape factor that normalizes the pair distribution function for a finite sample volume, calculated as the pair density for the continuum bounded by the the shear band (i.e. points spaced apart by a distance $r \ll D_{part}$) divided by the pair density for an unbounded, infinite sample. This shear band volume is calculated as the union of all shear band particle Voronoi volumes.

Examining the pair distribution functions along the loading axis and the perpendicular direction, $g(r,\|) \equiv g(r,\omega = 0)$ and $g(r,\perp) \equiv g(r,\omega = \pi/2)$ respectively, we identify peaks in $g(\mathbf{r})$, which mark the location of the nearest neighbor shells, as well as local minima (Figure 4.5a). In both directions, peak heights in $g(\mathbf{r})$ decrease in the shear band (relative to the matrix particles at the same time step), while the relative minima increase. This peak broadening indicates a less structured packing. The split second peak in the matrix, which reflects local icosahedral order[197], is also absent in the shear band, particularly at later timesteps and along the loading direction. The $g(\mathbf{r})$ difference plots in Figure 4.5b shows in more detail that the magnitude of the peaks in $g(\mathbf{r})$ decreases in the loading direction significantly more than in the transverse direction, while the

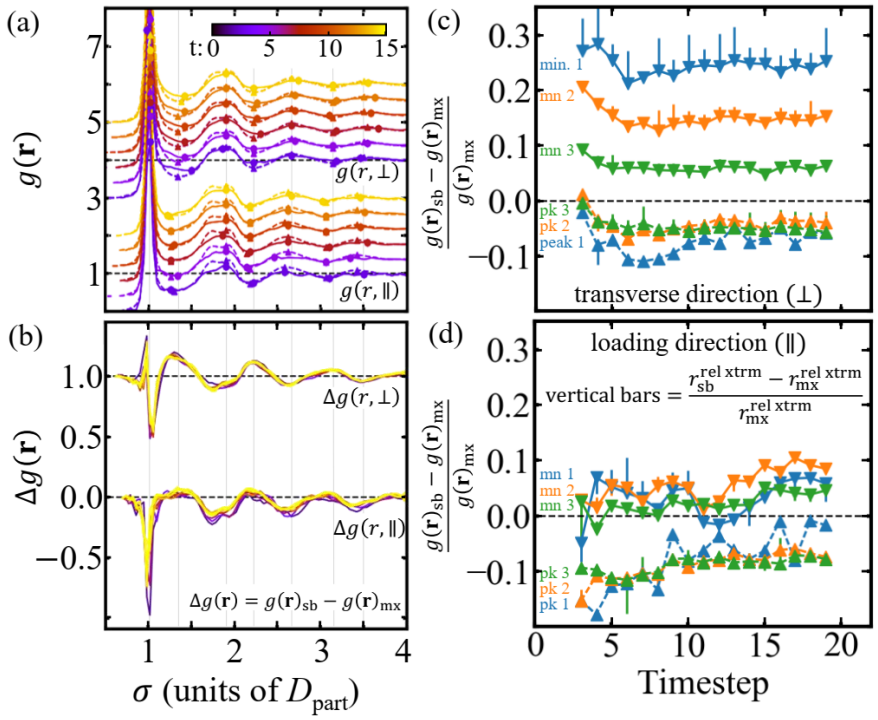

Figure 4.5: (a) Pair distribution function plots measured for the shear band particles (solid lines) and matrix particles (dashed lines), along the parallel and perpendicular directions to the loading. Local minima and maxima, calculated using a polynomial fit, are indicated with markers. Curves are offset for clarity. (b) Plots of the difference in $g(\mathbf{r})$ between shear band and matrix for each direction. (c) Fractional peak height differences between shear band and matrix for the transverse and (d) loading directions. Peak shifts are indicated by the vertical bars, where a positive (upwards) bar indicates a shift to greater r in the shear band relative to the matrix.

intensity at the minima in $g(\mathbf{r})$ increases more in the transverse directions. This indicates that nearest-neighbor "bonds" are broken primarily along the loading direction, and particles move to the spaces between nearest-neighbor shells in the transverse direction. See Suzuki et al. 1987[196] for schematic illustrations of such rearrangements. Based on percent changes in peak heights (Figure 4.5c-d) the nearest-neighbor shell within the shear band is ∼10% less populated in the loading direction compared to the matrix, while in the transverse direction the first local minimum (the space between the first two shells) is more populated by >20%, and the second minimum is ∼15% more populated. The higher-r local extrema (at $r > 4D_{part}$) have <6% change.

These changes in $g(\mathbf{r})$ suggest the presence of anelastic strain in the shear band which serves to screen the imposed stress, manifest as particle rearrangements from the loading direction to the transverse direction. This mechanism has been observed in X-ray scattering experiments on metallic glasses, as well as in molecular dynamics simulations on similar systems[195,198,199]. The peak height differences in the parallel direction and local minimum differences in the transverse direction decrease in magnitude and reach a stable value by $t = 10$ (i.e. during dilation), indicating a diminished capacity to support anelastic strains, as expected in a fluidized region. The short-range spatial extent of rearrangements (i.e. vanishing differences in $g(\mathbf{r})$ for $r > 4D_{part}$) is in good agreement with studies on crept metallic glasses and molecular dynamics glass models, which observe a cutoff in local (anelastic) strains at $r = 4D_{part}$[195,200].

To quantify this anelastic activity, we also compare $g_2^0(r)$, the $l = 2$ spherical harmonic of the anisotropic PDF, to the values expected to arise from affine deformation, where $g_2^0(r) \propto g(r_\parallel) - g(r_\perp)$ and $g_{2,affine}^0(r) \propto \epsilon r \frac{dg_0(r)}{dr}$ [196]. As shown in Figure 4.6, in the matrix this reveals short-range anelastic strains like those seen in MGs, which screen 20-40% of the elastic strain for r under $2-4D_{part}$[195,199,200]. In the shear band, however, the observed $g_2^0(r)$ does not deviate symmetrically from the affine (elastic) assumption $g_{2,affine}^0(r)$,

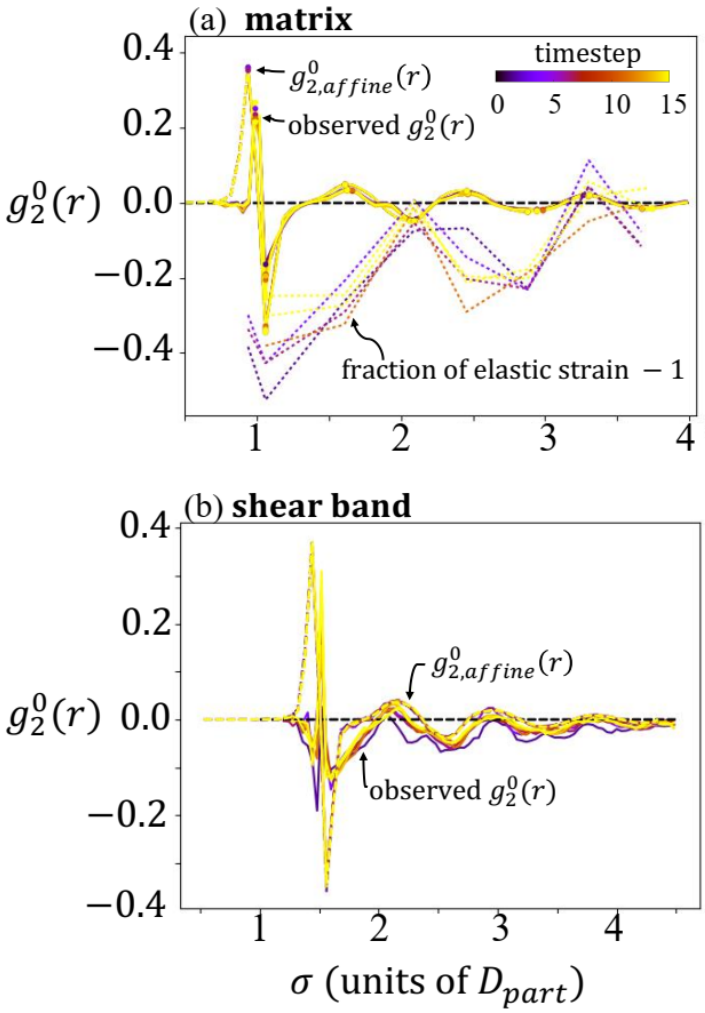

Figure 4.6: The anisotropic PDF decomposed by spherical harmonics. (a) In the unsheared matrix particles, the peaks of $g^0_{2,affine}(r)$, are fit to the observed $g^0_2(r)$, giving the fraction of the observed strain relative to the elastic (applied) strain ϵ[195,199,200]. This fraction is plotted and offset by 1, for ease of viewing. (b) In the shear band, such a fit is not possible, since the observed $g^0_2(r)$ does not deviate symmetrically from the affine curve. The first timestep plotted here, $t = 4$, is subject to sampling errors in the normalization since the particle number is small in the shear band at early timesteps.

indicating that the shear band does not support elastic strain but preventing quantification of anelastic strain.

Directional coordination

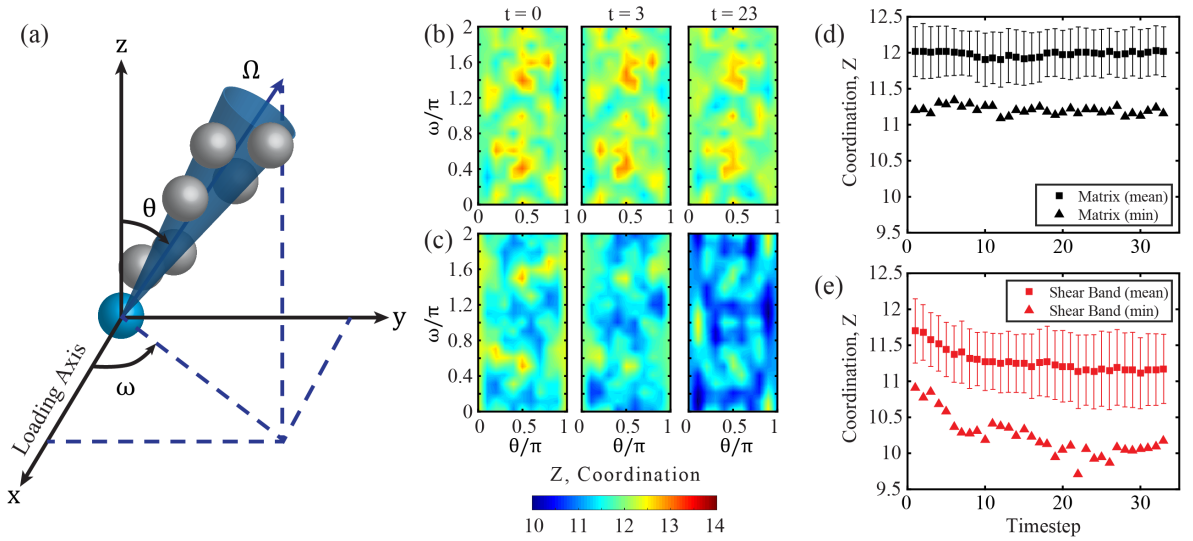

Figure 4.7: (a) The spherical coordinate conventions used to determine the average coordination along a given direction. The angular coordination in the matrix, row (b), and the shear band, row (c), at three timesteps. Little change in the coordination is observed in the matrix. The shear band, however, shows a decrease in the mean coordination and a decrease in the anisotropy of the coordination. The changes in Z in the matrix and shear band (here defined generously as a rectangular region) are quantified in (d) and (e), respectively, which show the evolution of the mean and minimum of Z with timestep. The error bars represent the standard deviation in Z.

Another detailed measure of the local structure is the directional coordination, which can be extracted from $g(\mathbf{r})$. A cone with its axis along a direction vector (with azimuthal angle ω and elevation angle θ) is defined so that the solid angle of the cone is given by Ω. All points within the cone are selected, and then the directionally dependent coordination $Z(\theta,\omega) = \int_0^{r_{min}} \eta g(\mathbf{r})\, d\mathbf{r}$ is calculated where r_{min} is the value of r at the first minimum in $g(r)$ and η is the particle number density N/V.

Figures 4.7b and c show the angular coordination in the matrix and shear band,

respectively, at three timesteps. It is apparent that the shear band , which was pre-deformed at $t = 0$, is on average under-coordinated with respect to the matrix, with particular under-coordination along $\{\theta \approx \pi/2, \omega \approx \pi\}$ (see Figures 4.7d and e). As deformation proceeds, Z in the shear band continues to decrease and becomes more anisotropic, which is reflected in the increasing standard deviation in Z (Figure 4.7e), with the most under-coordinated directions finally lying along $\{\theta \approx \pi, \omega \approx \pi\}$ and $\{\theta \approx 0, \omega \approx 0\}$. The closest-packed directions are along $\{\theta \approx \pi/4, \omega \approx \pi/2\}$ and $\{\theta \approx 3\pi/4, \omega \approx 3\pi/2\}$, which correspond to directions of minimum (deviatoric) shear for the uniaxial compression geometry. This result is in contrast to previous studies, which find more coordination along directions of high shear[201].

In stark contrast, Z in the matrix shows little change in both the mean and minimum coordination (see Figure 4.7d). On average, the shear band lacks one neighbor in comparison to the matrix, with the most under-coordinated directions having only ~ 10 neighbors in comparison to the matrix's mean value of 12. The evolution of Z in the shear band shows the same behavior as ϕ in that it remains static after $t = 10$.

Strain correlation function

These structural signatures collectively point to a solid- to liquid-like transition wherein the shear band prior to the transition can sustain elastic stress owing to anelastic rearrangements, whereas after the transition the rearrangements in the shear bad become fully plastic to relax the internal stresses. In metallic glasses, it has been shown that structural rejuvenation via thermal or mechanical processing can increase the material's capacity for plastic strain prior to catastrophic failure[202,203]. Our measurements of structural change directly in the shear band of a colloidal glass suggest an upper bound to the extent of rejuvenation possible in a finite volume of material. To establish a link between structure and local mechanical response, we analyze the spatial extent of local

shear deformation as measured by the shear strain correlation function χ_γ, calculated as follows.

We find the best affine deformation tensor $\boldsymbol{J_k}$ for particle k that maps particle k's neighbors at time t to their positions at time $t + \Delta t$ by minimizing the total non-affine displacement $D^2_{min,k} = 1/N \sum_{i=1}^{N} [\ \boldsymbol{r_i}(t + \Delta t) - \boldsymbol{J_k r_i}(t)]^{\ 2}$ [204]. A cut-off distance of $2D_{part}$ to identify a particle's neighbors was employed. The strain tensor $\boldsymbol{\epsilon_k}$ is found by extracting the symmetric part of $\boldsymbol{J_k}$ as $\boldsymbol{\epsilon_k} = \frac{1}{2}[\boldsymbol{J_k} + \boldsymbol{J_k^T}]$, which allows for the calculation of the shear strain $\gamma_k = \sqrt{\frac{1}{2}\,\mathrm{Tr}(\boldsymbol{\epsilon_k} - \Delta_k \boldsymbol{I})}$ where $\Delta_k = \frac{1}{3}\,\mathrm{Tr}(\boldsymbol{\epsilon_k})$ is the hydrostatic strain invariant. At each timestep, the spatial autocorrelation of $\gamma(\boldsymbol{r})$ is computed as:

$$\chi_\gamma(\boldsymbol{dr}) = \frac{\langle \gamma(\boldsymbol{r})\gamma(\boldsymbol{r} + \boldsymbol{dr})\rangle - \langle \gamma(\boldsymbol{r})\rangle^2}{\langle \gamma(\boldsymbol{r})^2\rangle - \langle \gamma(\boldsymbol{r})\rangle^2} \tag{4.2}$$

χ_γ is found to be quite anisotropic, but generally ellipsoidal, as shown in Figure 4.8, with particular directions exhibiting strong correlation at large distances, as expected in shear-dominated dynamics[205]. To quantify changes in the correlations as deformation proceeds, an ellipsoid is fit to an iso-intensity surface for each $\chi_\gamma(\boldsymbol{dr})$. The value of χ_γ as a function of distance $\sigma = r/D_{part}$ along the ellipsoid's major axis is a measure of the maximum extent of the correlation in strain, and is plotted in Figure 4.9a,b. At each timestep, we fit χ_γ to an exponential form $\chi_\gamma = \exp(-\sigma/\zeta)$ to extract the correlation length ζ, an approximate measure of rearrangement size[206].

These correlation lengths are plotted against the local volume fraction ϕ at the corresponding timestep in Figure 4.9c. In the matrix, the correlations are relatively unchanged throughout the experiment, with zero correlation beyond $\sigma = 4$, suggestive of minimal plastic activity and a shedding of any elastic stresses in favor of localized plastic deformation in the shear band. In the shear band, the spatial extent of the correlations decays as deformation proceeds. At $\phi > \phi_g$, the correlation at $\sigma = 10$ is significant

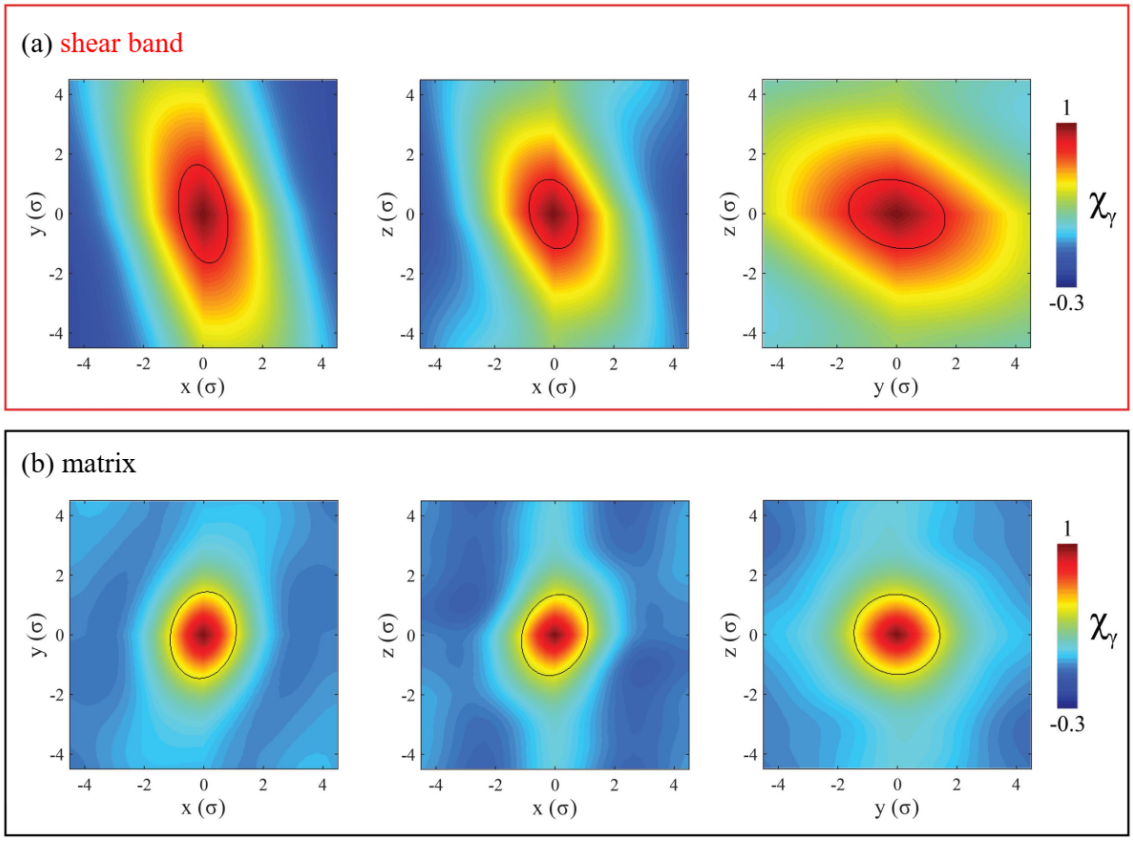

Figure 4.8: Slices along the x-y, x-z, and y-z planes of the strain correlation functions in both the a) shear band and b) the matrix. An ellipsoid is fit to an iso-intensity surface of the 3-D correlation. The anisotropy of the ellipsoid is quantified by the ratio of the major axis length to the minor axis length.

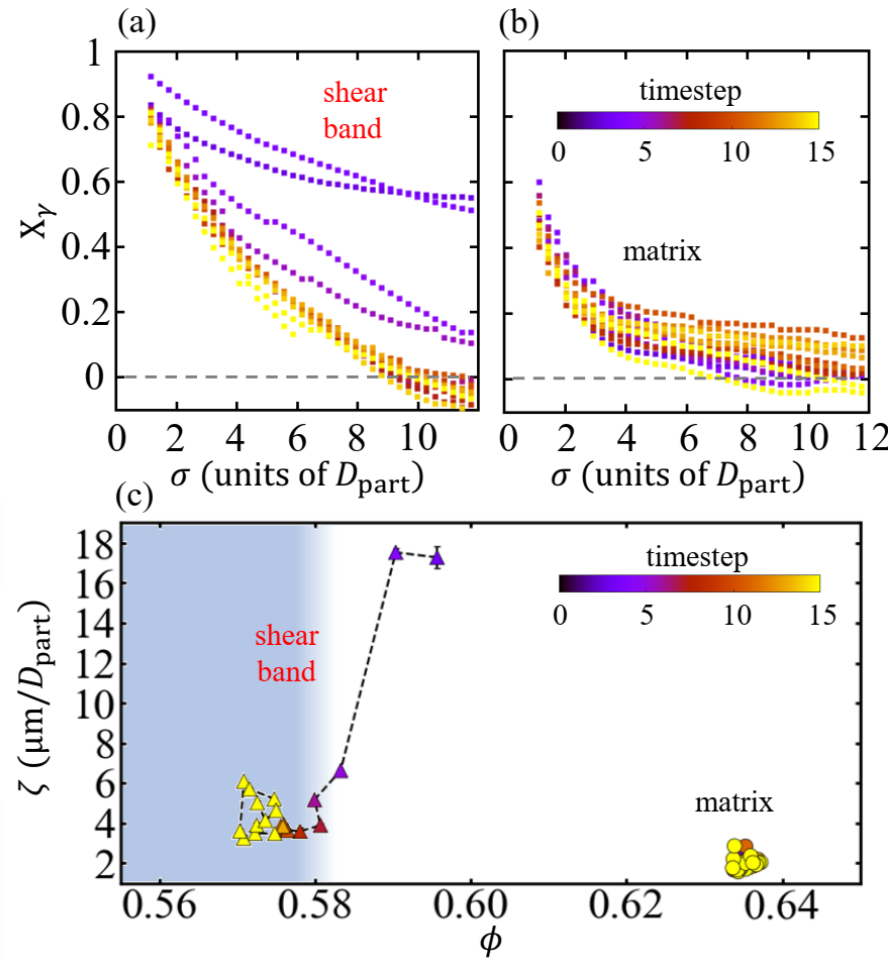

Figure 4.9: (a) Decay of the strain correlation χ_γ along the major ellipsoidal axis in the shear band and (b) matrix at different timesteps. (c) The correlation lengths ζ from a fit to exponential decay $\chi_\gamma = \exp(-\sigma/\zeta)$ plotted versus volume fraction. Data points for $t \geq 15$ (not shown in a and b) have the same coloring. Error bars mark the standard deviation of the errors of the fit, obscured by plot markers in most cases.

with $\chi_\gamma(\sigma = 10) \approx 0.2 - 0.6$, and correlation lengths are high, indicative of cooperative rearrangements system-spanning shear band, as has been observed in glass models at the yielding point[207]. Further dilation, however, reduces ζ. Notably, the timestep where ζ reaches a minimum corresponds to the same timestep, $t = 10$, where both ϕ and Z sharply saturate. This decay in the correlation lengths in shear strain signifies a transition from a solid-like to liquid-like response, which accompanies the changing structure within the shear band[207,208]. We also find that the anisotropy of the correlation, quantified by the ratio of the ellipsoid's major to minor axis, decays with dilation in the shear band from ∼3 to ∼1.5 (see Figure 4.8). The correlation in the matrix is isotropic, with anisotropy values ∼1.1 that persist throughout the experiment. We note that while the correlation lengths of the developing shear band tend to those of the matrix (Fig. 4.9c), they reflect different physics, as evident in the full dependence of the strain correlations with distance (Figs. 4.9a,b). In the shear band, the long-range correlation in strain at early timesteps is reminiscent of perfect slip along two planes. As the band fluidizes at later timesteps, the correlation length between plastic events decays to $\sim 5D_{part}$. In contrast, the matrix remains relatively undeformed once the shear band forms and only isolated plastic rearrangements occur in a manner that is relatively insensitive to the progression of the experiment, as has been observed in quiescent and deformed colloidal solids[209]. These results show the structural and mechanical transitions, as measured by ϕ, $g(r, \omega)$, and χ_γ, to be quite abrupt and consistent with a short range transition in structure.

4.2.4 Conclusions

Overall, our results quantitatively support the interpretation of shear banding as a driven, localized glass transition. Quasi-static deformation drives a reduction in ϕ in a thin band of the solid until ϕ approaches ϕ_g, at which point there is a sharp transition

and dilation ceases. Dilation is accompanied by a decay in the extent and anisotropy of spatial correlations in strain as well as a diminished capacity to support anelastic strains, which would give rise to memory effects before the onset of full plasticity, signifying a transition from solid-like to liquid-like response[190]. While we cannot rule out a first-order transition in the particle dynamics, the observed continuous changes in structure and mechanical response are consistent with the behavior of a glass as it approaches the glass transition from the solid phase. By definition, the spatial extent of the changes in structure and response is heterogeneous, and the resulting microstructure is clearly distinct from a microstructure that may be obtained from isotropic dilation, which is consistent with the conclusions drawn in[175,176]. Our results providing the microscopic origins of such driven transitions lend credence to an equivalency between mechanical shear banding and the glass transition provided that careful consideration of the spatial extent of the system is given.

4.3 Assembly of µLEDs via acoustic and magnetic fields

To explore further possibilities for multifunctional patterned materials, this section introduces hierarchical and orthogonal directed assembly methods. The material agnostic nature of acoustic assembly, wherein forces scale with the contrast in acoustic impedance (density and compressibility) and are otherwise independent of the chemical composition of both the particle and fluid phases, allows assembly of micro- or nano-structured building blocks with multiple constituents. Etched, coated, calcined, or templated particles, self-assembled aggregates of nanoparticle sub-units, or lithographically manufactured microcomponents can be used as building blocks and assembled with acoustic fields. Such

hierarchical structure opens pathways for powerful properties like further optimized transport via hierarchical (macro- and micro-) porosity or, here, arrayed functional microdevices for facile integration into electronic circuits. In this section, microdevices are fabricated lithographically and then assembled with acoustic fields. In addition to demonstrating the feasibility of hierarchical assembly with acoustophoresis, this also introduces possibilities for high-throughput fluidic handling of microdevices (here, micro light emitting diodes), which will dramatically reduce the cost of such devices.

Orthogonal assembly methods can also be combined with acoustic patterning, because of the non-contact and low-footprint nature of acoustic instrumentation. This combination of external fields allows additional degrees of freedom in structure assembly. Here, magnetic fields are combined with pressure fields to rotate the microdevices (which have integrated paramagnetic nickel electrodes), allowing manipulation along a additional axes than those possible with acoustics alone. The lithography of microdevices and a portion of the writing in this section was performed by Matthew Wong and collaborators from UC Santa Barbara, and this work was published in *Light-Emitting Devices, Materials, and Applications XXV* [81].

4.3.1 Introduction

Mass transfer of inorganic semiconductor devices has been an attractive research topic, since it gives the possibility of flexible electronics while maintaining device performance [210]. In recent years, because of their long operating lifespan, chemical robustness, and high luminous efficiency, micro-light-emitting diodes (µLEDs) have been studied thoroughly for next-generation display applications [211–216]. Moreover, extensive µLED demonstrations for displays, visible light-communication, and optogenetics have been reported [217–221]. However, especially in µLED displays, the mass transfer of µLEDs remains a critical

challenge, because millions of devices are required to transfer with extremely high yield and selectivity[222].

Compared to organic-light-emitting diodes (OLEDs) and self-emissive quantum dot light-emitting diodes (QLEDs), where solution-based inkjet printing is viable, µLEDs lack practical methods that provide rapid transfer rate[223–226]. As a result, the transfer of µLEDs is a cost- and time-intensive manufacturing process that results in expensive µLED displays[222]. Although various transfer approaches using elastomeric stamps have been developed, their transfer performance is hindered by challenges to precise placement and alignment and by the reliability of the plastic stamps[227,228]. On the other hand, fluidic assembly techniques using surface chemistry, gravity, or heat have been realized, and many of them have shown fast transfer rates[229–232]. Most of the demonstrated fluidic assembly approaches depend on a pre-patterned display panel for device alignment, where the movement control of devices is minimal and usually disorganized during the transfer process. This disordered characteristic is non-ideal for transfer in high volume, particularly in transferring three color devices for µLED displays, because this random nature can be material-costly and time-consuming and could introduce reliability issues.

In this work, a fluidic assembly method of InGaN µLEDs employing acoustic focusing and magnetic alignment is demonstrated. This transfer method not only gives precise control in all three translational and rotational degrees of freedom but also is material- and geometry-agnostic. The device alignment and orientation are modulated by two components, where acoustic focusing controls translational and rotational degrees of freedom, and the magnetic forces provide decoupled control over angular rotation, allowing uniform device orientation for reliable electrical contact. This transfer method can be utilized for display and functional fabric applications, where high throughput rate and roll-to-roll manufacturing are desired[222,233].

4.3.2 Experimental Methods

The c-plane (0001) InGaN/GaN III-nitride blue LED structures were grown on 2-inch single-side polished sapphire substrates by metalorganic chemical vapor deposition (MOCVD), and conventional device fabrication was performed to yield devices in 28×28 μm^2 with spacing of 3.5 µm between devices. After device fabrication, a silicon wafer coated with crystal bond was used to mount with the devices. Laser liftoff (LLO) was employed by using a Nd:YAG laser at 266 nm to remove µLEDs from the sapphire substrates[234–236]. After performing LLO, the devices were then rinsed in acetone multiple times for cleaning and transferred to isopropanol for fluidic assembly.

To demonstrate the control of device orientation using magnetic field, a rectangular device design with lateral metal contact characteristic was employed, since rectangular device shape has the optimal alignment characteristic. The device dimensions were 20×100 μm^2 with a light-emitting area of 20×40 μm^2, as efficient sidewall passivation methods have been developed for this device size range[236]. Figures 4.10(a,b) reveal the fabricated devices using confocal microscope and a diagram of the device structure. The devices used 500/100/500 nm of Al/Ni/Au common metal contacts with 100 nm indium-tin oxide (ITO) as the ohmic p-contact, where the Ni layer was used as the handle for magnetic field.

4.3.3 Results and Discussion

To examine the use of the external forces to the fluidic assembly performances, the role of acoustic focusing for device alignment is first analyzed. Figures 4.11(a,b) present the fluidic assembly of the square µLEDs without and with acoustic focusing. As shown in Figure 4.11a, the devices did not exhibit any ordering features without the use of acoustic focusing. However, by employing acoustic focusing, µLEDs assembled in lines with spacing

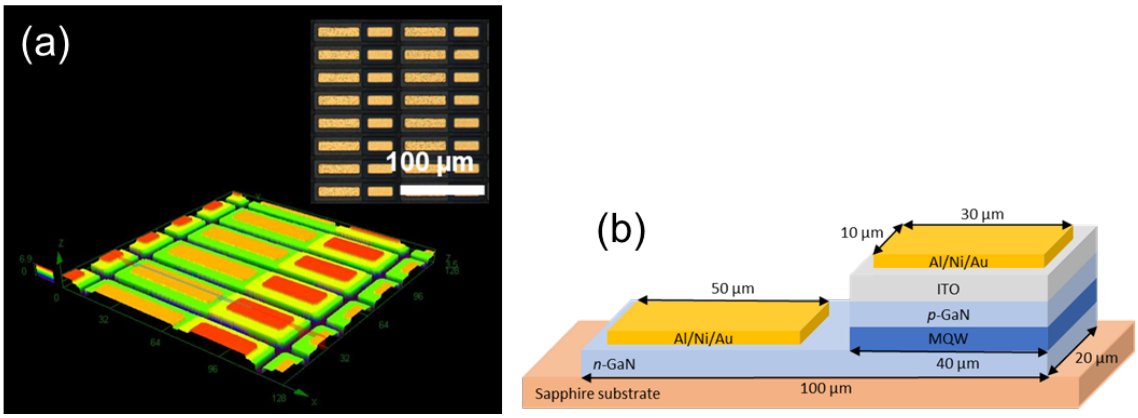

Figure 4.10: (a) Confocal microscope image of InGaN µLEDs with modified design after fabrication and (b) a diagram of device structure with dimensional information. The inset in Figure 1(a) is a micrograph of the fabricated devices.

of 200 µm. The spacing between lines and other assembly parameters is governed the wavelength of the acoustic wave, controlled by the frequency and voltage supplied to the vibrating piezoelectric actuator[28,53,54]. Figure 4.12 illustrates a schematic of the acoustic focusing channel design. When applying acoustic focusing, acoustic standing waves were induced within the microfluidic printing channel, which is 3 mm wide and 300 µm height. Depending on the acoustic wavelength, different numbers of node and anti-node were generated with their corresponding sinusoidal pressure forces, and lines of aligned devices were formed by the acoustic forces. Furthermore, since the acoustic forces rely merely on the contrasts in density and the compressibility between the device and the fluid medium, this process is largely material agnostic. Regardless of their chemical or electromagentic properties, semiconductor devices of nearly any solid material, including InGaN, AlGaN, or AlGaInP, can be manipulated.

In Figure 4.11b, the alignment was not perfect because of the creation of defective materials during LLO, in which the defective devices interfered the alignment. As a consequence of the fact that the LLO process was not optimized, LLO provided uniform and rapid sapphire removal process in most areas, but cracked and defective devices due

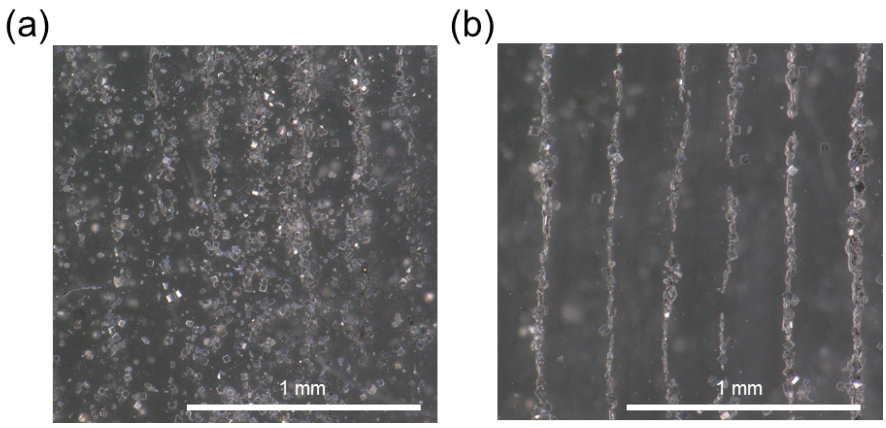

Figure 4.11: Micrographs of InGaN µLEDs (a) without and (b) with acoustic forces in isopropanol solution.

to the highpower LLO were observed from the silicon wafer. The defective devices could reduce or disrupt the ability to manipulate the ordering of devices within the focused lines. Therefore, optimizations on the LLO conditions or alternative liftoff methods or substrates, including photoelectrochemical (PEC) liftoff and epitaxial lateral overgrowth, could be considered to obtain damage-free substrate removal techniques[237,238].

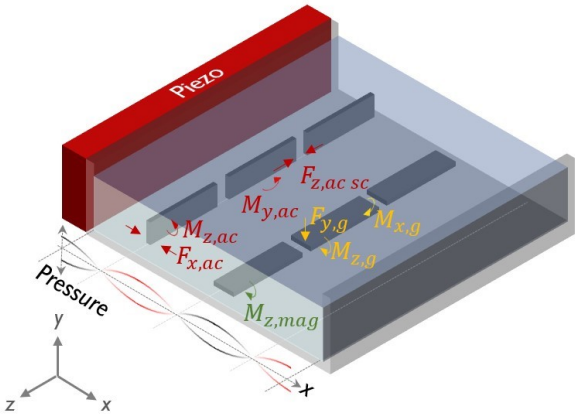

Figure 4.12: Schematic of the acoustic focusing channel design for device alignment in solution using acoustic induced pressure forces with labelled forces and moments from different fields.

A way to improve the ordering of the devices within the focused lines is to increase the

aspect ratio of the device geometry, where rectangular-shaped devices would yield better ordering performance[53]. From Figure 4.12, since the pressure field induces a moment, $M_{y,ac}$, on anisotropic devices, the rectangular devices are aligned within the focused lines. The axial assembly force, $F_{z,ac,sc}$, between devices, which results from scattered pressure waves, is also strengthened by the larger device dimensions[54].

Figures 4.13(a,b) present the microscope images of fluidic assembly of the µLEDs without and with an applied magnetic field while applying acoustic focusing, respectively. Without applying a magnetic field, the devices are ordered with an "edge-on" configuration, where the metal contacts are perpendicular to the printing surface. when applying magnetic field, in contrast, the devices are assembled with an "face-on" configuration, where the metal contacts are parallel to the printing surface. This orientation is controlled by the magnitude of the applied acoustic and magnetic fields. Using the standing pressure wave alone, the devices are oriented "edge-on", because the pressure amplitude (p_0) was high enough that the torque caused by the pressure differential across the width of the device overcomes the gravitational torque. Thus, magnetic field is required to rotate the devices into the "face-on" configuration for proper electrical contact via an underlying substrate circuit.

Decreasing the magnitude of the torque on the devices, even if the pressure amplitude is reduced, the devices that have initial orientations close to vertical in the channel before focusing will remain "edge-on" after focusing, so an applied magnetic field is required for uniform device orientation. This is demonstrated using acoustics theory, which provides well-established expressions for the time-averaged acoustic forces on spherical particles in viscous media[53]. The rectangular devices are simulated as clusters of spheres, as shown in Figure 4.14, which have the same shape and size as the µLEDs ($5\times20\times100$ µm^3) with the long direction taken to be already aligned in the z-direction (e.g. by hydrodynamic shear forces during flow through the channel)[4,36,37]. The acoustic radiation force $F_{f,x}$ acts

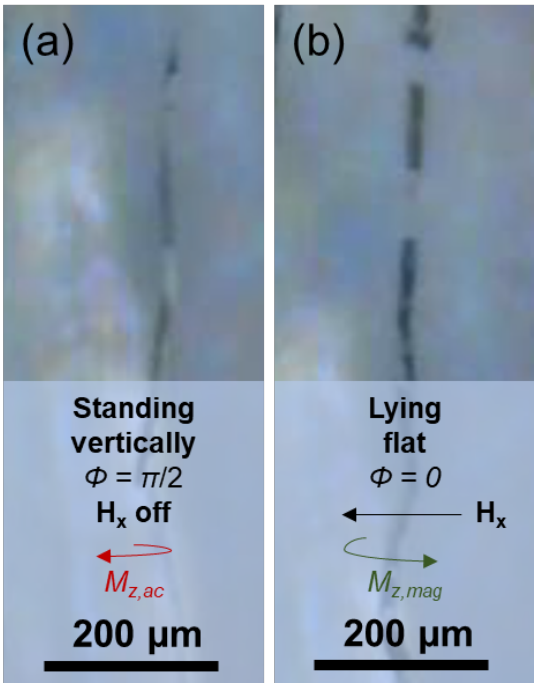

Figure 4.13: Micrographs of InGaN µLEDs (a) without and (b) with magnetic field when applying acoustic focusing in solution.

only in the wave-propagation (x) direction and is calculated with the constrained-sphere model described in Section 2.

This focusing force is balanced with drag and the buoyancy force acting in the y-direction that solved numerically to give trajectories of the devices under focusing, and the torque $F_{tot,y}x - F_{tot,x}y$ is balanced to find their orientation. An additional y^8 repulsive hard wall force is added at $y = 0$ to support the particle on the substrate. The resulting equations are solved numerically up to a normalized time $\tau_{max} = 0.001$ in rescaled units of $\tau = tf_0/(3\pi\mu a\lambda)$ (with time t in seconds) with $a = 2.5/400$ the normalized radius of each sphere, $\mu = 0.89$ mPa s the viscosity of the fluid, and wavelength $\lambda = 400$ µm.

The equilibrium orientation of the devices is shown in Figure 4.14b as a contour plot for various initial orientation angles ϕ_0 measured from the x-axis and pressure amplitudes p_0. While hydrodynamic shear forces during flow align the devices along their long direction

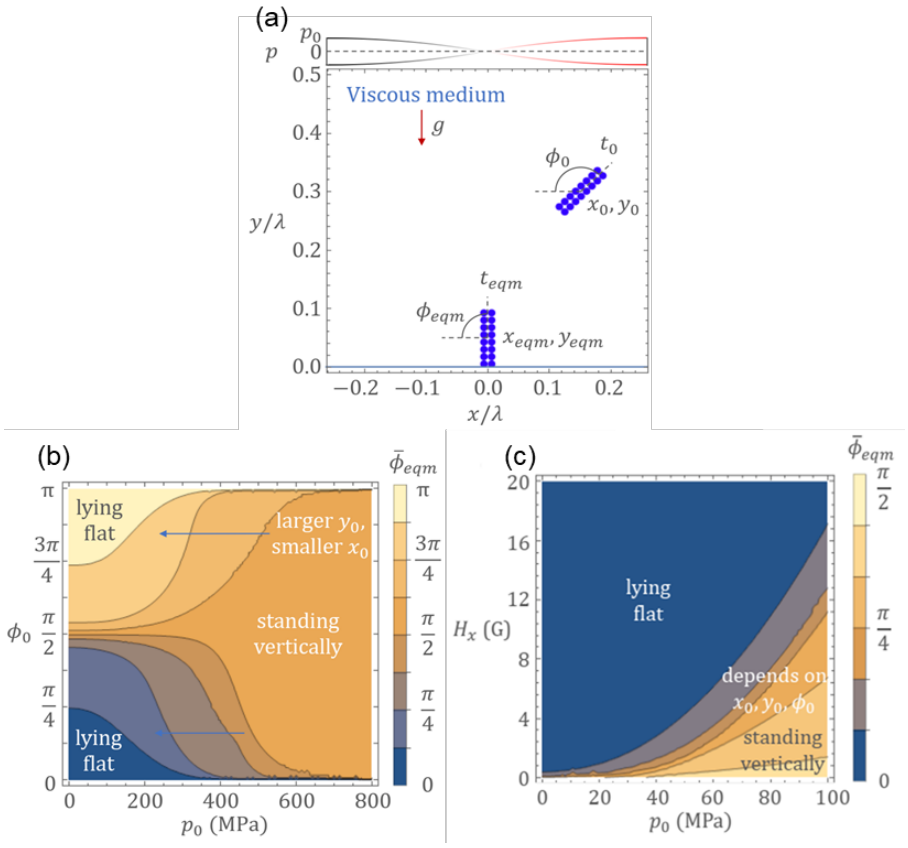

Figure 4.14: (a) Schematic of the µLEDs modeled as groups of spheres, (b) a counter plot of the equilibrium angle ϕ_{eqm} averaged over an array of possible initial positions, for given pressure amplitudes and initial orientations without an applied magnetic field, and (c) a contour plot of equilibrium angle, averaged over an array of initial positions and orientations for given magnetic field strengths and pressure amplitudes.

with the flow in the flow-focusing plane, the angle ϕ_0 in the gravity-focusing plane was not affected by these forces, so a uniform distribution of ϕ_0 is expected. The orientation angle at equilibrium, ϕ_{eqm}, is $\pi/2$ when the device is standing vertically in the "edge-on" configuration, and is 0 or π when the device is lying flat in the "face-on" configuration. This equilibrium orientation is averaged over fourteen initial positions regularly spaced throughout the channel of length $\lambda/2$ and height 300 µm, so ϕ_{eqm} has intermediate values only when the equilibrium orientation depends on the initial position. Because this constrained sphere model of the rectangular devices predicts a sign change in torque at

$|x| = \lambda/8$ whereas the more accurate finite element models predict a sign change closer to $\lambda/4$ (Section 2.3), the "standing vertically" conditions are likely expanded to lower p_0, further from $\phi_0 = \pi/2$, and require higher H_x to lie flat.

As shown in Figure 4.14b, even for small $p_0 < 50$ MPa, devices that started out with initial angle close to $\pi/2$ resulted in the "edge-on" configuration, while some devices could be modulated into the "face-on" configuration with appropriate initial angle range. Because utilizing small p_0 could introduce inhomogenous equilibrium configurations and longer assembly time, it is advantageous to focus quickly using high p_0 to achieve "edge-on" configuration, Figure 4.13(a), and then apply magnetic field to align all devices to achieve the "face-on" configuration for electrical contact, Figure 4.13(b). The magnetic field strength required to rotate the device to the "face-on" configuration is shown in Figure 4.14(c). The acoustic pressure amplitude and magnetic field used in the experiment were 60 MPa and 10 Gauss, respectively, to ensure the equilibrium is found on the order of milliseconds.

Finally, the optical enhancement after substrate removal was analyzed using photoluminescence (PL). Figure 4.15 demonstrates the difference in PL intensity for devices with metal contacts before and after LLO using optimized laser power conditions. The peak wavelength remained identical at 447 nm after LLO, while the PL intensity increased by more than 50%. It is expected that the improvement in PL intensity was attributed from better light extraction efficiency due to the removal of the sapphire substrate [239,240].

4.3.4 Conclusions

In conclusion, a fluidic assembly approach of InGaN µLEDs using external forces was demonstrated. This fluidic assembly approach employed acoustic focusing and magnetic fields to give precise control over device alignment and orientation, so that the orientation

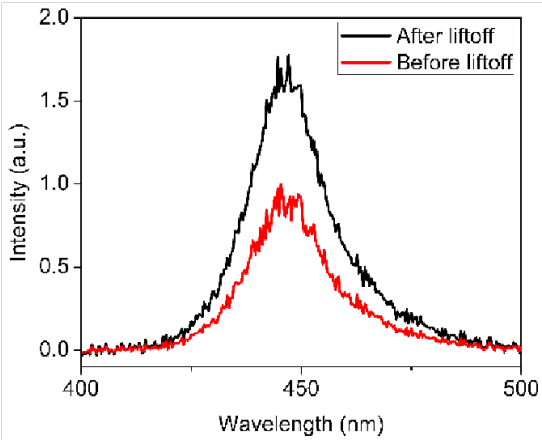

Figure 4.15: PL intensity of µLEDs before and after LLO sapphire substrate removal.

of the assembled devices is tuned by modulating the parameters of the external forces. This time-efficient fluidic assembly approach will serve as a high throughput mass transfer method to make products such as µLED displays at a reduced manufacturing cost and time.

Chapter 5

Conclusion

5.1 Summary

This thesis commences by applying the theory of acoustic forces on particles to model large numbers of interacting particles in pressure fields. Analytical models for acoustic forces on spheres in pressure fields are simplified to a point that allows efficient computational modeling of thousands of suspended particles while still being accurate in the regimes of interest, as validated by experimental observations. These models map the geometry of acoustically patterned composites, guiding process engineers to the parameters needed for desired pattern features. A systematic sweep of the parameter space demonstrates that particles can be assembled into stripes with features such as height, width, and spacing that can be controlled reliably over a broad range by modulating input parameters such as pressure wave frequency and amplitude, particle volume fraction, and degree of initial settling by gravity.

Microstructural features are found to be less readily modulated via input parameters, but well-suited for various functional properties in composite materials. Packing density nears the random close packing limit of 64v% and particle contact density shows moderate

anisotropy favoring particle contacts along the assembled stripes, useful for creating highly conductive pathways or interlocking particle structures. These results guide process design for controlling the properties of patterned materials, and outline the property ranges accessible via acoustic patterning. In particular, these structural features are especially amenable to fast electrical, thermal, and ionic transport along certain directions in composites.

This theoretical framework is then extended to the case of non-spherical particles in pressure fields. In many applications, fibers or flakes are preferred over spheres because when aligned they can redistribute stress more efficiently or pack more closely, reducing electrical and thermal resistance. Finite-element models are developed to calculate acoustic forces on rods and disks, since analytical expressions as-yet inaccurately predict scattering forces on non-spherical particles and torque on short fibers. These models are compared to experimental observations, explaining the mechanisms behind alignment and packing differences between particle geometries and guiding discussion of further property improvements.

Next, processing methods for acoustically patterning 3D printed composites are developed experimentally. Concentrating filler particles into stripes using pressure fields is particularly useful for improving electrical conductivity, which relies on continuous networks of contacting conductive filler particles across a material. Acoustic assembly aligns and patterns ceramic or metallic fibers into highly efficient percolated networks which utilize up to 97% of the conductive material in the composite, whereas the inefficient stochastic networks of conventional unpatterned composites utilize <5%. As a result, these patterned materials become conductive at several times lower particle loading than unpatterned materials. The materials also have conductivity an order of magnitude higher than conventional composites made with the same ink, and reach 48% the conductivity of bulk silver within assembled silver-particle networks (at 2.6v% loading). The combination

of high conductivity at low filler loading allows 3D printing of electrical interconnects without clogging, lowers costs, and introduces the possibility of multiple simultaneous functionalities in the same material (discussed below).

Furthermore, modulating the shape of the applied acoustic fields (via parameters like the wavelength to fiber length ratio) controls the bridging of fibers between focused lines and, thereby, the anisotropy of assembled conductive networks, producing materials which are either 2-D conductive, 1-D conductive, or insulating, all using the same nozzle and ink. This fiber orientation behavior is supported by models, which accurately predict thresholds for bridging between stripes. Applications like (soft) robotics, wearable electronics, and medical diagnostic devices see significant cost savings and design opportunities in integrating electrical interconnects and bulk conductive material into 3D printed components.

Another promising application of patterned composites is cooling of electronics, because currently a main limiting factor to the power density of electronic devices is thermal dissipation. Acoustic patterning to align and compact filler particles into stripes during stereolithographic 3D printing creates efficient heat transport pathways through polymer-based composite materials. The thermal conductivity is highly anisotropic, up to 350% higher parallel to patterned stripes than perpendicular, and up to 300% higher than unpatterned materials. Conductivity approaches the upper bound for the particles used, reaching 95v% of the particle utilization of parallel conduction. Patterned carbon fiber composites reach conductivity of 2.5 W/m.K at 12v% loading carbon fiber, nearly identical to recent aligned-fiber filament deposition modeling studies with similar filler loading, but acoustophoretic 3D printing allows much lower viscosity (enabling e.g. solution processing and wetting of small components) and much higher strain tolerance (especially important during thermal cycling).

To investigate routes for further improving conductivity via a higher degree of filler

alignment and denser local packing packing, finite element models of acoustic forces on particles with different geometries are compared to experiment, finding that the acoustic driving forces align fibers quickly and stack them end-on-end, whereas flakes stack along their edges (as confirmed with X-Ray computed tomography scans) and align more slowly, still misaligned by the time they reach the low pressure node. This is confirmed in the microstructure of patterned materials, where the measured degree of alignment is much higher in patterned carbon fiber materials than in boron nitride flake materials. This structure controls the thermal conductivity of the materials, which is significantly higher in carbon fiber materials. This information is used to discuss optimal particle geometries and strategies for further improving the conductivity of acoustically patterned materials.

Finally, patterning composites presents a promising opportunity to tailor the structure of materials for multiple functional properties simultaneously, optimizing each function for given applications. As an example case, conventional conductive composites require high filler particle loading to reach high conductivity, which renders them brittle under deformation. To circumvent this tradeoff, patterning locally dense stripes of particles encapsulated with polymer sheathes encourages strain absorption in the polymer without breaking contacts between particles, allowing mechanical flexibility simultaneously with the improved conductivity due to the formation of percolated networks. Acoustically patterned materials withstand >500 bending cycles without significant losses in conductivity and change conductivity only 5% within cycles on average (for 2.6v% composites). In contrast, conventional unpatterned composites with similar conductivity require such high loading that they are prohibitively brittle, cracking at low strains during the first cycle.

Further investigation of the mechanical response of packed particle assemblies is undertaken by analyzing the 3D trajectories of particles during compression of a colloidal pillar using confocal microscopy. This experiment mimics the conditions of the flexible patterned composites but in the limit of a low-viscosity matrix. Deformation upon loading

is found to be localized to a narrow band of particles within the material, which shears and dilates until it reaches the glass transition. A transition from solid- to liquid-like mechanical response accompanies the structural change in the band, as evidenced by the packing fraction reaching and saturating at the glass transition point, a diminishing ability to host anelastic strains, and a rapid decay in the long-range strain correlations. In sum, these results suggest that compressed colloidal solids fail by highly localized shear banding, which quantitatively resembles a localized, driven glass transition, and help to explain the changes in conductivity observed in acoustically patterned composites during cyclic loading. These results also pioneer methods for detailed analysis of particle movement in packed particle assemblies during deformation of patterned composite materials, and potentially for tracking assembly during acoustic patterning (e.g. for comparison to the above-mentioned molecular dynamics simulations, or for tuning packing fraction and contact anisotropy).

Additional multifunctional materials are investigated by assembling micro-structured particles into hierarchically structured patterns and combining acoustics with magnetic particle manipulation. Lithographically fabricated microparticles with functional features including InGaN light-emitting diodes and paramagnetic handles are acoustically patterned into stripes and simultaneously rotated with magnetic fields, expanding particle manipulation capabilities via additional degrees of freedom. The interaction between the acoustic and magnetic torques is mapped to guide patterning of the microdevices into arrays for integration into electrical circuits. Additionally, we employ sacrificial phases and explore additional printing strategies to expand the application space of patterned materials into high-throughput processing methods for microdevices and, in future work, battery electrodes.

5.2 Outlook and future work

5.2.1 Thermally conductive composites

Though the thermal conductivity of acoustically patterned composites reported in Section 3.2 is competitive with filament deposition printing at similar particle loading (illustrated in Figure 5.1) while dramatically lowering viscosity during processing (useful e.g. for solution processing and inflow around small components) and increasing mechanical flexibility, the thermal conductivity is not high enough to be directly applicable in the most highly demanded applications like 3D printing of heatsinks for electronic devices[68,69].

In the computer chip manufacturing industry, for example, new polymer composite infill materials with high thermal conductivity (>10 W/m.K) are needed to cool the next generation of stacked chips[68] and in LED, laser diode, and other electronics packaging, 3D printed polymer composites have become a leading candidate for lowering the processing cost of heat sinks, heat spreaders, and components with integrated electronics[69]. For these applications, developing composite materials with high conductivity that can still be processed during packaging is a difficult problem. As discussed in Section 3.2 the main challenge is that the material must have high enough thermal conductivity to transport heat away from hot spots, which requires high filler particle loading, while simultaneously being processable or printable, which requires low filler loading. This problem is limiting the performance, longevity, and geometry of new electronics and driving demand for creative solutions[68,69].

Target packing fractions suggested by hot-pressing studies are 50v% to reach 10 W/m.K within the assembled patterns (using boron nitride flakes in a polymer matrix). This requires a high degree of alignment of filler particles, as well as particle geometry amenable to stacking with maximal contact area. For comparison, the packing limit for randomly-oriented disks (with similar aspect ratio to the BN flakes in the Section 3.2)

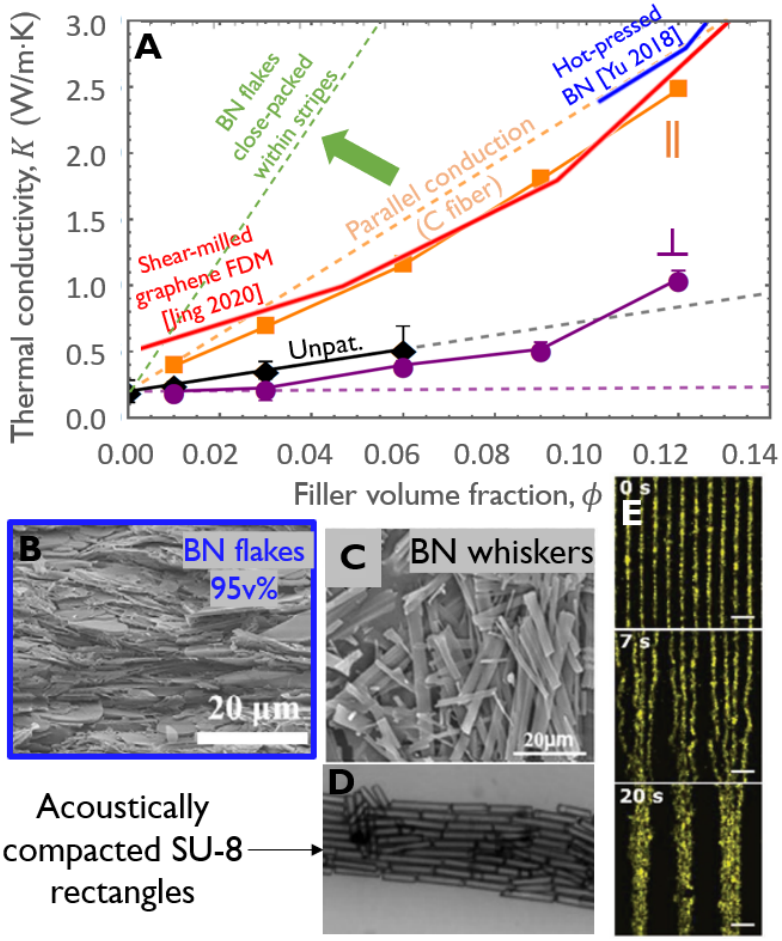

Figure 5.1: **A** Plot of the thermal conductivity of patterned carbon fiber composites developed in Section 3.2 (labeled || for conductivity parallel to patterned stripes), compared to filament deposition printed materials and hot-pressed boron nitride[69,71]. The expected conductivity when BN flakes are close-packed within patterned stripes ($\phi_{\text{local}} > 90$v%, using pressed BN conductivity from literature, reproduced in **B**[69]) is plotted as the green line, indicating that conductivity > 10 W/m.K is possible below $\phi = 20$v%. **C** Electron microscopy image of BN whisker particles, illustrating elongated aspect ratio for acoustic alignment and flat faces for lower interfacial resistance. **D** Acoustically patterned rectangular particles functionalized to weakly adhere to one another, reproduced from[53] with permission. **E** Images of the acoustic stripe merging process accomplished by switching between resonant frequencies, reproduced with permission from[52].

is 30v%. To accomplish this denser packing, it is necessary to (1) choose the optimal particles for acoustic alignment and dense packing, (2) implement pressure-field frequency modulation methods to mimic the vibration commonly used to densify granular packings, and (3) implement frequency switching methods to sequentially split and merge assembled lines to break pinning contacts, re-align particles, and compact them back together.

Printing patterned composites with packing fractions above 50v% (for thermal conductivity above 10 W/m.K) requires several steps: improving the integration of acoustic patterning into 3D printing, choosing suitable particles, and implementing field switching and modulation techniques. Further, methods for creating user-defined particle patterns will be proposed and computer modeling of pressure fields and particle packing will be outlined.

The first step is integrating acoustic patterning into 3D printing. Stereolithographic printers can be modified by adding low-profile piezoelectric transducers into the photopolymer bath without disruption of the optics or build plate positioning stages[42,51], as demonstrated in Section 3.2. Furthermore, the resolution and build size is similar for both stereolithography and acoustic patterning (feature size >1 µm and build size on the order of centimeters) and is ideal for electronics applications, which entail hot spots on the order of hundreds of microns[28,51]. Uniformity of the assembled pattern during printing must be improved over these previous results, however, for alignment of particles and optimal packing. Bottom-up printing is the ideal configuration because the build plate and previously cured layers can be removed from the bath when printing new layers, removing scattering interfaces which distort the pressure field. This requires an additional step during the printing process of lowering the build plate and previous layers back into contact with the new layer and a brief curing to bond the two pieces, which in turn requires careful tuning of the cure depth and bonding with the bath floor (controlled by curing dose, photoabsorber content in the photopolymer, and oxygen content)[241]. This

setup also avoids exciting surface acoustic waves at the free surface of the liquid, which causes significant pattern distortion[242].

Next, improved packing of filler particles within the assembled patterns is critical to achieving high thermal conductivity. The first consideration is particle material and geometry. Boron nitride is a top material candidate because it has high thermal conductivity while being electrically insulating and having low thermal expansion, which prevents shorting or damaging electrical components. Particle shape is a strong determinant of packing efficiency, which is critical to achieving high conductivity because locally dense packing is required to ensure high surface contact area between particles, ensuring the maximum utilization efficiency of the conductive filler in continuous networks and minimizing interfacial resistance. As shown in Section 2.1, simulations of spherical microparticles in acoustic fields have shown that the acoustic interactions are sufficient to overcome drag, gravity, and interparticle hydrodynamic interactions and approach the random close-packing limit of 64v%. Since this limit is relatively low for spheres, and since spheres can only form point contacts, flakes and whiskers (rod-like particles with rectangular cross-section, illustrated in Figure 5.1C) are a better particle shape because they pack more tightly (>90v%) when aligned and have high contact surface area along their flat faces.

As shown in Figure 5.1A, however, experiments on acoustically assembled boron nitride flakes only reached 25v% packing, which is below the random close-packing limit and thus indicates counter-productive alignment. Calculations of the acoustic torque and force on different particle shapes indicate that while the acoustic forces do exert driving forces for alignment and stacking of anisotropic particles, flakes (modeled as disks) have a relatively weaker torque and rotate into alignment much slower than whiskers or fibers (modeled as rods) when overcoming drag. As a result, flakes are still misaligned by the time they reach the low-pressure node and become pinned on other particles. This was confirmed

in measurements of experimentally patterned materials, which have angle distributions of 0±25° for carbon fibers and a much wider distribution of 0±50° for BN flakes. As such, particles with whisker geometry combine the necessary attributes of flat faces for dense packing and elongated shape for improved alignment (Figure 5.1C). This tighter alignment and packing has been observed in acoustic patterning (Figure 5.1D)[53] when using rectangular polymeric particles, proving the concept that rectangular particles stack well.

Despite the acoustic driving forces for fiber alignment and stacking (Section 3.2), collisions between particles pin them on each other during assembly, preventing total alignment and resulting in relatively loose packing, as observed in experiment. In granular materials engineering this is overcome by vibrating the assembly[136], breaking contacts between particles and allowing rearrangements so that it approaches the close packing limit (>90v% for aligned fibers or whiskers). Within the acoustically assembled patterns this can be mimicked by modulating the frequency of the applied pressure field (at modulation rates of Hz to kHz and bandwidth of 1-100 kHz, a common capability of signal generators), effectively vibrating the low pressure nodes back and forth while still applying the packing forces. This is expected to allow subtle rearrangements, but for highly misaligned, high-aspect-ratio particles, longer-range rearrangement may be necessary. These larger-scale rearrangements will be accomplished by splitting the assembly into smaller parts by switching between resonant frequencies during assembly, as illustrated in Figure 5.1E. Higher-frequency pressure fields (∼7 MHz) split assembled stripes into smaller equally-spaced stripes but still exert a high aligning torque on whiskers, which allows rotation without pinning against as many other particles. After this initial step, returning to a lower frequency (∼3 MHz) merges the stripes back into contact, compacting the particles together. This process can be repeated, breaking the pinning of any misaligned whiskers and, in conjunction with frequency modulation, allowing packing to approach 90v% within

stripes. At 90v% packing within stripes, the overall loading of the patterning area (including the pure polymer between stripes) must be at least 18v% for overall conductivity of 10 W/m.K (illustrated with the green line in Figure 5.1A), readily accomplished by adjusting the layer thickness under the build plate after particles have settled. This approach will achieve high conductivity in printed composites while encapsulating patterns in pure polymer to retain mechanical integrity (Section 4.1) and maintaining low viscosity in the feedstock material.

Molecular dynamics-style simulations like those in Section 2.1 combined with the forces and torques determined by finite element analysis on non-spherical particles (Sections 2.3 and 3.2) are within reach to model packing of non-spherical particles and inform optimization of the particle geometry, assembly parameters, and frequency modulation and switching techniques.

Finally, experiments have shown that the addition of nanofillers to microfiber composites significantly increases conductivity via transport between microparticle surfaces[243]. While not necessary in whisker composites if the contact surface area is already high, this approach may provide alternate routes for increased conductivity in the fiber composites studied previously. Since the acoustic force scales with particle volume, nanofillers with high surface area (like nanofibers and platelets) focus much more slowly than microrods (or not at all, if velocity currents are present in the fluid[100,110]). This suggests that the microrods will focus quickly to the low-pressure nodes, sweeping up nanofiller in the process, and, if the nanofiller size is optimized so that the acoustic force overcomes drag while still being small enough to fill the gaps between microrods, pack around the microrods and effectively increase contact surface area.

5.2.2 User-defined patterns during stereolithography

More complex patterns which can curve around obstacles to form electrical interconnects or optimize heat flow paths are also within reach and provide an opportunity for novel material patterning capabilities. To accomplish this, it's necessary to modify the boundary conditions of the pressure field in the printing bath. This can be accomplished by placing a phase plate near the piezo to locally slow down the field in engineered positions[43]. The phase shift is controlled by the thickness of the phase plate at a given position, $\Delta T\left(x,y\right)$, such that $\Delta\phi\left(x,y\right)=\left(k_l-k_s\right)\Delta T(x,y)$ on the transmission face of the reservoir and $\Delta\phi\left(x,y\right)=2k_l\Delta T(x,y)$ on the reflecting faces, where $\Delta\phi$ is the required phase change (calculated in an optimization problem to form the desired particle pattern[43]) and $k_{l,s}$ are the wavenumbers in the liquid and solid (cured) polymer. This approach can be incorporated into stereolithography by curing the photopolymer in the bath near the walls of the container. Finite element modeling will be necessary to determine whether phase plates printed on one layer affect the field in subsequent layers. If they do, an additional build plate will need to be built into the printer to allow removal of printed phase plates between layer prints.

5.2.3 Hierarchical porosity in battery cathodes

The improvements and modulation of anisotropic thermal and electrical transport accomplished in Section 3.1 and 3.2 suggest that ionic transport may be improved in similar ways. Fast ionic transport through preferred directions in composite materials would be particularly useful in lithium-ion battery electrodes, in which electronic capacity is limited by slow lithium ion transport through the cathode. Standard cathodes in these batteries consist of micron-sized particles of active cathode material (e.g. $LiPO_4$) randomly packed with carbon black (for electrical transport to the current collector) in a matrix

of liquid electrolyte. Patterning stripes or grids of alternating electrolyte and packed cathode particles in these cathodes would decrease the transport distance through the cathode to the particles, increasing rate performance or capacity[12,15]. Acoustophoresis is well-suited to this patterning task, though tuning of packing density, stripe width and spacing, and cathode thickness will be needed to maximize rates and cathode material utilization efficiency.

Cathodes and anodes for Lithium-ion batteries, when architected to concentrate active intercalation material into periodic line features on the scale of hundreds of microns, demonstrate increases in gravimetric and volumetric energy density, rate performance, and fast charging performance[15–17]. These structures have been fabricated previously using co-extrusion printing whereby alternating rows of electrode material and electrolyte material enable fast ion transport in thick electrodes. While these co-extrusion and other co-deposition studies[18] have shown compatibility with large scale manufacturing, an unexplored area is fabricating features over comparable areas with feature sizes less than 100 µm and higher degrees of control over pattern morphology and microstructure.

Fabrication of these materials using acoustophoresis would be convenient using extrusion-based printing instead of vat-based stereolithography, allowing facile integration into high-throughput roll-to-roll processing. To do this, form holding after extrusion presents a significant challenge. The conventional method, increasing viscosity and utilizing shear-thinning additives like fumed silica, restricts acoustic assembly times and prevents assembly of tightly focused structures[45,55]. Alternative approaches like using support material[126] or otherwise confining the printed beads are promising approaches but still result in significant loss of structure upon extrusion. Another approach is ultraviolet-assisted curing instead of shear-thinning rheology for form holding, which allows low viscosity during acoustic assembly in the nozzle and increases viscosity only at the nozzle outlet during extrusion[129]. Such an approach combines the form-holding advantages

of light-based printing methods like stereolithography with the scalability of direct-ink writing.

Bibliography

[1] C. Mattheck, I. Tesari, *Design & Nature II* **2004**, 10.

[2] X. Zheng, H. Lee, T. H. Weisgraber, M. Shusteff, J. DeOtte, E. B. Duoss, J. D. Kuntz, M. M. Biener, Q. Ge, J. A. Jackson, S. O. Kucheyev, N. X. Fang, C. M. Spadaccini, *Science* **2014**, *344*, 1373–1377.

[3] Z. Jia, Y. Yu, L. Wang, *Materials & Design* **2019**, *168*, 107650.

[4] B. G. Compton, J. A. Lewis, *Advanced Materials* **2014**, *26*, 5930–5935.

[5] T. R. Ray, J. Choi, A. J. Bandodkar, S. Krishnan, P. Gutruf, L. Tian, R. Ghaffari, J. A. Rogers, *Chemical Reviews* **2019**, *119*, 5461–5533.

[6] R. M. Mutiso, K. I. Winey, *Progress in Polymer Science* **2015**, *40*, 63–84.

[7] N. A. M. Radzuan, A. B. Sulong, J. Sahari, *International Journal of Hydrogen Energy* **2017**, *42*, 9262–9273.

[8] M.-S. Cao, X.-X. Wang, M. Zhang, J.-C. Shu, W.-Q. Cao, H.-J. Yang, X.-Y. Fang, J. Yuan, *Advanced Functional Materials* **2019**, *29*, 1807398.

[9] B. Liao, G. Chen, *MRS Bulletin* **2015**, *40*, 746–752.

[10] T. Gao, Z. Yang, C. Chen, Y. Li, K. Fu, J. Dai, E. M. Hitz, H. Xie, B. Liu, J. Song, B. Yang, L. Hu, *ACS Nano* **2017**.

[11] J. Chen, X. Huang, Y. Zhu, P. Jiang, *Advanced Functional Materials* **2017**, *27*, 1604754.

[12] C. L. Cobb, M. Blanco, *Journal of Power Sources* **2014**, *249*, 357–366.

[13] J. H. Pikul, J. W. Long, *MRS Bulletin* **2019**, *44*, 789–795.

[14] J. W. Long, B. Dunn, D. R. Rolison, H. S. White, *Chemical Reviews* **2004**, *104*, 4463–4492.

[15] C. L. Cobb, S. E. Solberg, *Journal of The Electrochemical Society* **2017**, *164*, A1339.

[16] V. P. Nemani, S. J. Harris, K. C. Smith, *Journal of The Electrochemical Society* **2015**, *162*, A1415.

[17] U. Gulzar, C. Glynn, C. O'Dwyer, *Current Opinion in Electrochemistry* **2020**, 46–53.

[18] A. W. Parsekian, T. A. Harris, *ACS Applied Materials & Interfaces* **2019**, *12*, 3736–3745.

[19] C. Zhu, A. J. Pascall, N. Dudukovic, M. A. Worsley, J. D. Kuntz, E. B. Duoss, C. M. Spadaccini, *Annual Review of Chemical and Biomolecular Engineering* **2019**, *10*, annurev–chembioeng–060718–030133.

[20] M. R. Begley, D. S. Gianola, T. R. Ray, *Science* **2019**, *364*, 4299.

[21] A. T. L. Tan, J. Beroz, M. Kolle, A. J. Hart, *Advanced Materials* **2018**, *30*, 1803620.

[22] Y. Sha, L. Jiani, C. Haoyu, R. O. Ritchie, X. Jun, *International Journal of Mechanical Sciences* **2018**, *149*, 150–163.

[23] C. M. Spadaccini, *MRS Bulletin* **2019**, *44*, 782–788.

[24] B. Delattre, R. Amin, J. Sander, J. De Coninck, A. P. Tomsia, Y.-M. Chiang, *Journal of the Electrochemical Society* **2018**, *165*, A388.

[25] W. Xiong, Y. Liu, L. J. Jiang, Y. S. Zhou, D. W. Li, L. Jiang, J.-F. Silvain, Y. F. Lu, *Advanced Materials* **2016**, *28*, 2002–2009.

[26] S. Shabaniverki, J. J. Juárez, *Micromachines* **2021**, *12*, 935.

[27] J. Liu, A. Kim, L. Wang, B. Palmer, Y. Chen, P. Bruinsma, B. Bunker, G. Exarhos, G. Graff, P. Rieke *et al.*, *Advances in colloid and interface science* **1996**, *69*, 131–180.

[28] D. S. Melchert, R. R. Collino, T. R. Ray, N. D. Dolinski, L. Friedrich, M. R. Begley, D. S. Gianola, *Advanced Materials Technologies* **2019**, 1900586.

[29] D. Kokkinis, M. Schaffner, A. R. Studart, *Nature Communications* **2015**, *6*,.

[30] J. J. Martin, B. E. Fiore, R. M. Erb, *Nature Communications* **2015**, *6*,.

[31] E. Loth, S. Baumann, C. P. Lutz, D. M. Eigler, S. Heinrich, *Science* **2012**, *335*, 196–199.

[32] A.-I. Bunea, N. del Castillo Iniesta, A. Droumpali, A. E. Wetzel, E. Engay, R. Taboryski, *Micro*, **2021**, pp. 164–180.

[33] K. Thorkelsson, P. Bai, T. Xu, *Nano Today* **2015**, *10*, 48–66.

[34] D. S. Melchert, K. Johnson, B. Giera, E. J. Fong, M. Shusteff, J. Mancini, J. J. Karnes, C. L. Cobb, C. Spadaccini, D. S. Gianola, M. R. Begley, *Materials & Design* **2021**, *202*, 109512.

[35] Z. Liu, P. Peng, Z. Liu, W. Fang, Q. Zhou, X. Liu, J. Liu, *Composites Science and Technology* **2018**, *165*, 39–47.

[36] H. L. Tekinalp, V. Kunc, G. M. Velez-Garcia, C. E. Duty, L. J. Love, A. K. Naskar, C. A. Blue, S. Ozcan, *Composites Science and Technology* **2014**, *105*, 144–150.

[37] J. P. Lewicki, J. N. Rodriguez, C. Zhu, M. A. Worsley, A. S. Wu, Y. Kanarska, J. D. Horn, E. B. Duoss, J. M. Ortega, W. Elmer, R. Hensleigh, R. A. Fellini, M. J. King, *Scientific Reports* **2017**, *7*,.

[38] Y.-F. Zhu, C. Ma, W. Zhang, R.-P. Zhang, N. Koratkar, J. Liang, *Journal of Applied Physics* **2009**, *105*, 054319.

[39] C. Ma, W. Zhang, Y. Zhu, L. Ji, R. Zhang, N. Koratkar, J. Liang, *Carbon* **2008**, *46*, 706–710.

[40] E. C. Sengezer, G. D. Seidel, R. J. Bodnar, *Polymer Composites* **2015**, *36*, 1266–1279.

[41] J. Greenhall, B. Raeymaekers, *Advanced Materials Technologies* **2017**, *2*, 1700122.

[42] J. Greenhall, F. Guevara Vasquez, B. Raeymaekers, *Applied Physics Letters* **2016**, *108*, 103103.

[43] K. Melde, A. G. Mark, T. Qiu, P. Fischer, *Nature* **2016**, *537*, 518–522.

[44] H. Bruus, *Lab on a Chip* **2012**, *12*, 1578.

[45] R. R. Collino, T. R. Ray, L. M. Friedrich, J. D. Cornell, C. D. Meinhart, M. R. Begley, *Materials Research Letters* **2018**, *6*, 191–198.

[46] J. Greenhall, F. Guevara Vasquez, B. Raeymaekers, *Applied Physics Letters* **2014**, *105*, 144105.

[47] C. Reyes, L. Fu, P. P. A. Suthanthiraraj, C. E. Owens, C. W. Shields, G. P. López, P. Charbonneau, B. J. Wiley, *Particle & Particle Systems Characterization* **2018**, *35*, 1700470.

[48] S. M. Hagsäter, T. G. Jensen, H. Bruus, J. P. Kutter, *Lab on a Chip* **2007**, *7*, 1336.

[49] P. Wadsworth, I. Nelson, D. L. Porter, B. Raeymaekers, S. E. Naleway, *Materials & Design* **2019**, 108243.

[50] K. Niendorf, B. Raeymaekers, *Composites Part B: Engineering* **2021**, *223*, 109096.

[51] D. E. Yunus, S. Sohrabi, R. He, W. Shi, Y. Liu, *Journal of Micromechanics and Microengineering* **2017**, *27*, 045016.

[52] J. P. K. Armstrong, J. L. Puetzer, A. Serio, A. G. Guex, M. Kapnisi, A. Breant, Y. Zong, V. Assal, S. C. Skaalure, O. King, T. Murty, C. Meinert, A. C. Franklin, P. G. Bassindale, M. K. Nichols, C. M. Terracciano, D. W. Hutmacher, B. W. Drinkwater, T. J. Klein, A. W. Perriman, M. M. Stevens, *Advanced Materials* **2018**, *30*, 1802649.

[53] R. R. Collino, T. R. Ray, R. C. Fleming, C. H. Sasaki, H. Haj-Hariri, M. R. Begley, *Extreme Mechanics Letters* **2015**, *5*, 37–46.

[54] R. R. Collino, T. R. Ray, R. C. Fleming, J. D. Cornell, B. G. Compton, M. R. Begley, *Extreme Mechanics Letters* **2016**, *8*, 96–106.

[55] L. Friedrich, R. Collino, T. Ray, M. Begley, *Sensors and Actuators A: Physical* **2017**, *268*, 213–221.

[56] R. L. Truby, J. A. Lewis, *Nature* **2016**, *540*, 371–378.

[57] B. Derby, *Annual Review of Materials Research* **2010**, *40*, 395–414.

[58] M. L. Shofner, K. Lozano, F. J. Rodríguez-Macías, E. V. Barrera, *Journal of Applied Polymer Science* **2003**, *89*, 3081–3090.

[59] F. Ning, W. Cong, J. Qiu, J. Wei, S. Wang, *Composites Part B: Engineering* **2015**, *80*, 369–378.

[60] T. Baasch, J. Dual, *The Journal of the Acoustical Society of America* **2018**, *143*, 509–519.

[61] E. J. Ekoi, A. N. Dickson, D. P. Dowling, *Composites Part B: Engineering* **2021**, *212*, 108704.

[62] Y. Chen, L. Ye, *Composites Science and Technology* **2021**, *204*, 108644.

[63] R. D. Sochol, E. Sweet, C. C. Glick, S.-Y. Wu, C. Yang, M. Restaino, L. Lin, *Microelectronic Engineering* **2018**, *189*, 52–68.

[64] E. MacDonald, R. Wicker, *Science* **2016**, *353*, aaf2093–aaf2093.

[65] T. Tilford, S. Stoyanov, J. Braun, J. C. Janhsen, M. Burgard, R. Birch, C. Bailey, *Microelectronics Reliability* **2018**, *85*, 109–117.

[66] B. Y. Ahn, E. B. Duoss, M. J. Motala, X. Guo, S.-I. Park, Y. Xiong, J. Yoon, R. G. Nuzzo, J. A. Rogers, J. A. Lewis, *Science* **2009**, *323*, 1590–1593.

[67] W. Bauhofer, J. Z. Kovacs, *Composites Science and Technology* **2009**, *69*, 1486–1498.

[68] H. Chen, V. V. Ginzburg, J. Yang, Y. Yang, W. Liu, Y. Huang, L. Du, B. Chen, *Progress in Polymer Science* **2016**, *59*, 41–85.

[69] C. Yu, W. Gong, W. Tian, Q. Zhang, Y. Xu, Z. Lin, M. Hu, X. Fan, Y. Yao, *Composites Science and Technology* **2018**, *160*, 199–207.

[70] F. Kargar, Z. Barani, R. Salgado, B. Debnath, J. S. Lewis, E. Aytan, R. K. Lake, A. A. Balandin, *ACS Applied Materials & Interfaces* **2018**, *10*, 37555–37565.

[71] J. Jing, Y. Chen, S. Shi, L. Yang, P. Lambin, *Chemical Engineering Journal* **2020**, *402*, 126218.

[72] J. Wang, S. Mubarak, D. Dhamodharan, N. Divakaran, L. Wu, X. Zhang, *Composites Communications* **2020**, *19*, 142–146.

[73] H. Guo, H. Zhao, H. Niu, Y. Ren, H. Fang, X. Fang, R. Lv, M. Maqbool, S. Bai, *ACS Nano* **2021**, *15*, 6917–6928.

[74] T. Sekitani, T. Someya, *Advanced Materials* **2010**, *22*, 2228–2246.

[75] J. A. Rogers, T. Someya, Y. Huang, *Science* **2010**, *327*, 1603.

[76] T. Sekitani, H. Nakajima, H. Maeda, T. Fukushima, T. Aida, K. Hata, T. Someya, *Nature Materials* **2009**, *8*, 494–499.

[77] X. Z. Niu, S. L. Peng, L. Y. Liu, W. J. Wen, P. Sheng, *Advanced Materials* **2007**, *19*, 2682–2686.

[78] K. S. Kim, Y. Zhao, H. Jang, S. Y. Lee, J. M. Kim, K. S. Kim, J.-H. Ahn, P. Kim, J.-Y. Choi, B. H. Hong, *Nature* **2009**, *457*, 706–710.

[79] S. Merilampi, T. Björninen, V. Haukka, P. Ruuskanen, L. Ukkonen, L. Sydänheimo, *Microelectronics Reliability* **2010**, *50*, 2001–2011.

[80] D. J. Strickland, D. S. Melchert, J. L. Hor, C. P. Ortiz, D. Lee, D. S. Gianola, *Physical Review E* **2020**, *102*, 032605.

[81] M. S. Wong, D. Melchert, M. Haggmark, D. J. Myers, S. Grandrothula, M. de Vries, D. Gianola, M. Begley, T. Magarlith, J. S. Speck, S. P. DenBaars, S. Nakamura, *Light-Emitting Devices, Materials, and Applications XXV*, **2021**, p. 1170607.

[82] K. Melde, E. Choi, Z. Wu, S. Palagi, T. Qiu, P. Fischer, *Advanced Materials* **2018**, *30*, 1704507.

[83] L. Lu, X. Tang, S. Hu, Y. Pan, *3D Printing and Additive Manufacturing* **2018**, *5*, 151–159.

[84] L. V. King, *Proceedings of the Royal Society A: Mathematical Physical and Engineering Sciences* **1934**, *147*, 212–240.

[85] L. P. GOR'KOV, *Sov. Phys. Dokl.* **1962**, *6*, 773–775.

[86] H. Bruus, *Lab on a Chip* **2012**, *12*, 1014.

[87] S. Sepehrirahnama, K.-M. Lim, F. S. Chau, *The Journal of the Acoustical Society of America* **2015**, *137*, 2614–2622.

[88] T. Baasch, I. Leibacher, J. Dual, *The Journal of the Acoustical Society of America* **2017**, *141*, 1664–1674.

[89] G. T. Silva, H. Bruus, *PHYSICAL REVIEW E* **2014**, 11.

[90] L. Verlet, *Phys. Rev* **1967**, *159*, 98–103.

[91] J. A. Simeonov, J. Calantoni, *International Journal of Multiphase Flow* **2012**, *46*, 38–53.

[92] M. D. A. Cooley, M. E. O'Neill, *Mathematika* **1969**, *16*, 37–49.

[93] Z. Jiang, P. Haff, *Water resources research* **1993**, *29*, 399–412.

[94] T. Laurell, F. Petersson, A. Nilsson, *Chem. Soc. Rev.* **2007**, *36*, 492–506.

[95] M. Weiser, R. Apfel, E. Neppiras, *Acta Acustica united with Acustica* **1984**, *56*, 114–119.

[96] A. Tahmasebipour, L. Friedrich, M. Begley, H. Bruus, C. Meinhart, *The Journal of the Acoustical Society of America* **2020**, *148*, 359–373.

[97] S. Sepehrirhnama, K.-M. Lim, *Physical Review E* **2020**, *102*, 043307.

[98] R. Barnkob, P. Augustsson, T. Laurell, H. Bruus, *Lab on a Chip* **2010**, *10*, 563.

[99] I. Iranmanesh, R. Barnkob, H. Bruus, M. Wiklund, *17th International Conference on Miniaturized Systems for Chemistry and Life Sciences, MicroTAS 2013; Freiburg; Germany*, **2013**, pp. 1400–1402.

[100] P. B. Muller, R. Barnkob, M. J. H. Jensen, H. Bruus, *Lab on a Chip* **2012**, *12*, 4617.

[101] P. Hahn, J. Dual, *Physics of Fluids* **2015**, *27*, 062005.

[102] R. Barnkob, P. Augustsson, T. Laurell, H. Bruus, *Physical Review E* **2012**, *86*, 056307.

[103] M. R. Kuhn, W. Sun, Q. Wang, *Acta Geotechnica* **2015**, *10*, 399–419.

[104] Q. Niu, A. Revil, Z. Li, Y.-H. Wang, *Geophysical Journal International* **2017**, *210*, 1–17.

[105] D. J. Strickland, D. S. Melchert, J. L. Hor, C. P. Ortiz, D. Lee, D. S. Gianola, *Physical Review E* **2020**, *102*, 032605.

[106] Q. Niu, A. Revil, Z. Li, Y.-H. Wang, *Geophysical Journal International* **2017**, *210*, 1–17.

[107] Y.-J. Li, S.-L. Li, P. Gong, Y.-L. Li, X.-Y. Fang, Y.-H. Jia, M.-S. Cao, *Physica E: Low-dimensional Systems and Nanostructures* **2018**, *104*, 247–253.

[108] Y.-H. Jia, P. Gong, S.-L. Li, W.-D. Ma, X.-Y. Fang, Y.-Y. Yang, M.-S. Cao, *Physics Letters A* **2020**, *384*, 126106.

[109] F. Jiang, D. Drummer, *Polymers* **2020**, *12*, 1080.

[110] R. Barnkob, I. Iranmanesh, M. Wiklund, H. Bruus, *Lab on a Chip* **2012**, *12*, 2337.

[111] K. Pietrak, T. S. Wisniewski, *Journal of Power Technologies* **2015**, *95*, 14–24.

[112] S. Yamahira, S.-i. Hatanaka, M. Kuwabara, S. Asai, *Japanese Journal of Applied Physics* **2000**, *39*, 3683–3687.

[113] E. B. Lima, J. P. Leão-Neto, A. S. Marques, G. C. Silva, J. H. Lopes, G. T. Silva, *Physical Review Applied* **2020**, *13*, 064048.

[114] W. L. Nyborg, *The Journal of the Acoustical Society of America* **1967**, *42*, 947–952.

[115] F. Petersson, L. Åberg, A.-M. Swärd-Nilsson, T. Laurell, *Analytical Chemistry* **2007**, *79*, 5117–5123.

[116] T. Schwarz, *PhD Thesis*, ETH Zurich, **2013**.

[117] T. Schwarz, P. Hahn, G. Petit-Pierre, J. Dual, *Microfluidics and Nanofluidics* **2015**, *18*, 65–79.

[118] S. Sepehrirhnama, K.-M. Lim, *Physical Review E* **2020**, *102*, 043307.

[119] J. T. Karlsen, H. Bruus, *Physical Review E* **2015**, *92*, 043010.

[120] J. Dual, T. Schwarz, *Lab Chip* **2012**, *12*, 244–252.

[121] J. P. Leão-Neto, J. H. Lopes, G. T. Silva, *The Journal of the Acoustical Society of America* **2020**, *147*, 2177–2183.

[122] S. M. Hasheminejad, R. Sanaei, *Journal of Computational Acoustics* **2007**, *15*, 377–399.

[123] A. Tahmasebipour, L. Friedrich, M. Begley, H. Bruus, C. Meinhart, *The Journal of the Acoustical Society of America* **2020**, *148*, 359–373.

[124] L. Friedrich, M. Begley, *Journal of Colloid and Interface Science* **2018**, *529*, 599–609.

[125] L. Friedrich, M. Begley in *Polymer-Based Additive Manufacturing: Recent Developments*, ACS Publications, **2019**, pp. 131–149.

[126] L. Friedrich, M. Begley, *ACS Applied Polymer Materials* **2020**, *2*, 2528–2540.

[127] L. Friedrich, M. Begley, *Additive Manufacturing* **2020**, *34*, 101192.

[128] L. Friedrich, *Tailored Composite Microstructures via Direct Ink Writing with Acoustophoresis*, University of California, Santa Barbara, **2020**.

[129] R. D. Farahani, L. L. Lebel, D. Therriault, *Journal of Micromechanics and Microengineering* **2014**, *24*, 055020.

[130] E. Han, N. Van Ha, H. M. Jaeger, *Soft Matter* **2017**, *13*, 3506–3513.

[131] M. Foygel, R. D. Morris, D. Anez, S. French, V. L. Sobolev, *Physical Review B* **2005**, *71*,.

[132] J. Perelaer, P. J. Smith, D. Mager, D. Soltman, S. K. Volkman, V. Subramanian, J. G. Korvink, U. S. Schubert, *Journal of Materials Chemistry* **2010**, *20*, 8446.

[133] T. Levard, P. J. Diglio, S.-G. Lu, C. D. Rahn, Q. M. Zhang, *Smart Materials and Structures* **2012**, *21*, 012001.

[134] M. T. Cortés, J. C. Moreno, *e-Polymers* **2003**, *3*,.

[135] Z. Lin, Y. Liu, S. Raghavan, K.-s. Moon, S. K. Sitaraman, C.-p. Wong, *ACS Applied Materials & Interfaces* **2013**, *5*, 7633–7640.

[136] K. J. Solis, J. E. Martin, *Journal of Applied Physics* **2012**, *111*, 073507.

[137] J. Su, X. Liu, M. Charmchi, H. Sun, *International Journal of Heat and Mass Transfer* **2016**, *97*, 645–652.

[138] F. Du, J. E. Fischer, K. I. Winey, *Physical Review B* **2005**, *72*, 121404.

[139] S. S. Rahatekar, M. Hamm, M. S. Shaffer, J. A. Elliott, *The Journal of chemical physics* **2005**, *123*, 134702.

[140] T. Tallman, K. Wang, *Nanotechnology* **2014**, *26*, 025501.

[141] A. M. Marconnet, N. Yamamoto, M. A. Panzer, B. L. Wardle, K. E. Goodson, *ACS Nano* **2011**, *5*, 4818–4825.

[142] K. M. Champley, T. M. Willey, H. Kim, K. Bond, S. M. Glenn, J. A. Smith, J. S. Kallman, W. D. Brown, I. M. Seetho, L. Keene *et al.*, *NDT & E International* **2021**, 102595.

[143] J. Schindelin, I. Arganda-Carreras, E. Frise, V. Kaynig, M. Longair, T. Pietzsch, S. Preibisch, C. Rueden, S. Saalfeld, B. Schmid *et al.*, *Nature methods* **2012**, *9*, 676–682.

[144] B. Münch, P. Gasser, L. Holzer, R. Flatt, *Journal of the American Ceramic Society* **2006**, *89*, 2586–2595.

[145] R. A. Ketcham, *Geosphere* **2005**, *1*, 32–41.

[146] T. Mori, K. Tanaka, *Acta metallurgica* **1973**, *21*, 571–574.

[147] S. Azeem, M. Zain-ul-Abdein, *International Journal of Engineering Science* **2012**, *52*, 30–40.

[148] D. Park, Y. Kim, S. Lee, J. Kim, *Synthetic Metals* **2021**, *276*, 116763.

[149] Y. Agari, M. Tanaka, S. Nagai, T. Uno, *Journal of Applied Polymer Science* **1987**, *34*, 1429–1437.

[150] A. Wouterse, S. R. Williams, A. P. Philipse, *Journal of Physics: Condensed Matter* **2007**, *19*, 406215.

[151] A. C. de Leon, B. J. Rodier, C. Bajamundi, A. Espera, P. Wei, J. G. Kwon, J. Williams, F. Ilijasic, R. C. Advincula, E. Pentzer, *ACS Applied Energy Materials* **2018**, *1*, 1726–1733.

[152] G. Postiglione, G. Natale, G. Griffini, M. Levi, S. Turri, *Composites Part A: Applied Science and Manufacturing* **2015**, *76*, 110–114.

[153] J. Perelaer, B.-J. de Gans, U. S. Schubert, *Advanced Materials* **2006**, *18*, 2101–2104.

[154] M. D. Dickey, *Advanced Materials* **2017**, *29*, 1606425.

[155] N. Saengchairat, T. Tran, C.-K. Chua, *Virtual and Physical Prototyping* **2017**, *12*, 31–46.

[156] D. Rus, M. T. Tolley, *Nature* **2015**, *521*, 467–475.

[157] A. D. Valentine, T. A. Busbee, J. W. Boley, J. R. Raney, A. Chortos, A. Kotikian, J. D. Berrigan, M. F. Durstock, J. A. Lewis, *Advanced Materials* **2017**, *29*, 1703817.

[158] A. Greer, Y. Cheng, E. Ma, *Materials Science and Engineering: R: Reports* **2013**, *74*, 71–132.

[159] C. A. Schuh, T. C. Hufnagel, U. Ramamurty, *Acta Materialia* **2007**, *55*, 4067–4109.

[160] R. Besseling, E. R. Weeks, A. Schofield, W. Poon, *Physical Review Letters* **2007**, *99*, 028301.

[161] V. Chikkadi, G. Wegdam, D. Bonn, B. Nienhuis, P. Schall, *Physical Review Letters* **2011**, *107*, 198303.

[162] A. Kabla, G. Debrégeas, *Physical Review Letters* **2003**, *90*, 258303.

[163] M. D. Ediger, C. Angell, S. R. Nagel, *The Journal of Physical Chemistry* **1996**, *100*, 13200–13212.

[164] P. G. Debenedetti, F. H. Stillinger, *Nature* **2001**, *410*, 259–267.

[165] C. S. O'Hern, L. E. Silbert, A. J. Liu, S. R. Nagel, *Physical Review E* **2003**, *68*, 011306.

[166] S. Gokhale, A. Sood, R. Ganapathy, *Advances in Physics* **2016**, *65*, 363–452.

[167] W. Johnson, K. Samwer, *Physical Review Letters* **2005**, *95*, 195501.

[168] Y. Liu, C. T. Liu, W. Wang, A. Inoue, T. Sakurai, M. Chen, *Physical Review Letters* **2009**, *103*, 065504.

[169] P. Guan, M. Chen, T. Egami, *Physical Review Letters* **2010**, *104*, 205701.

[170] T. Egami, *Journal of Alloys and Compounds* **2011**, *509*, S82–S86.

[171] P. Olsson, S. Teitel, *Physical Review Letters* **2007**, *99*, 178001.

[172] A. Basu, Y. Xu, T. Still, P. Arratia, Z. Zhang, K. Nordstrom, J. M. Rieser, J. Gollub, D. Durian, A. Yodh, *Soft Matter* **2014**, *10*, 3027–3035.

[173] V. Chikkadi, D. Miedema, M. Dang, B. Nienhuis, P. Schall, *Physical Review Letters* **2014**, *113*, 208301.

[174] P. K. Jaiswal, I. Procaccia, C. Rainone, M. Singh, *Physical Review Letters* **2016**, *116*, 085501.

[175] B. A. Isner, D. J. Lacks, *Physical Review Letters* **2006**, *96*, 025506.

[176] A. Furukawa, K. Kim, S. Saito, H. Tanaka, *Physical Review Letters* **2009**, *102*, 016001.

[177] R. Hurley, S. Hall, J. Andrade, J. Wright, *Physical review letters* **2016**, *117*, 098005.

[178] J. R. Greer, J. T. M. De Hosson, *Progress in Materials Science* **2011**, *56*, 654–724.

[179] D. J. Strickland, Y.-R. Huang, D. Lee, D. S. Gianola, *Proceedings of the National Academy of Sciences* **2014**, *111*, 18167–18172.

[180] G. L. Hunter, E. R. Weeks, *Reports on Progress in Physics* **2012**, *75*, 066501.

[181] J. Crocker, *Journal of Colloid and Interface Science* **1996**, *179*, 298–310.

[182] A. Ikeda, L. Berthier, P. Sollich, *Physical review letters* **2012**, *109*, 018301.

[183] S. Henderson, T. Mortensen, S. M. Underwood, W. van Megen, *Physica A: Statistical Mechanics and its Applications* **1996**, *233*, 102–116.

[184] E. Bartsch, T. Eckert, C. Pies, H. Sillescu, *Journal of non-crystalline solids* **2002**, *307*, 802–811.

[185] E. R. Weeks, J. C. Crocker, A. C. Levitt, A. Schofield, D. A. Weitz, *Science* **2000**, *287*, 627–631.

[186] P. N. Pusey, W. Van Megen, *Nature* **1986**, *320*, 340–342.

[187] L. C. Hsiao, S. Jamali, E. Glynos, P. F. Green, R. G. Larson, M. J. Solomon, *Physical review letters* **2017**, *119*, 158001.

[188] M. H. Cohen, D. Turnbull, *The Journal of Chemical Physics* **1959**, *31*, 1164–1169.

[189] D. Turnbull, M. H. Cohen, *The Journal of Chemical Physics* **1970**, *52*, 3038–3041.

[190] F. Spaepen, *Acta Metallurgica* **1977**, *25*, 407–415.

[191] A. Argon, *Acta Metallurgica* **1979**, *27*, 47–58.

[192] L. Li, E. R. Homer, C. A. Schuh, *Acta materialia* **2013**, *61*, 3347–3359.

[193] K. Martens, L. Bocquet, J.-L. Barrat, *Physical review letters* **2011**, *106*, 156001.

[194] W. L. Johnson, J. Lu, M. D. Demetriou, *Intermetallics* **2002**, *10*, 1039–1046.

[195] T. Egami, Y. Tong, W. Dmowski, *Metals* **2016**, *6*, 22.

[196] Y. Suzuki, J. Haimovich, T. Egami, *Physical Review B* **1987**, *35*, 2162.

[197] A. S. Clarke, H. Jónsson, *Physical Review E* **1993**, *47*, 3975.

[198] T. C. Hufnagel, R. T. Ott, J. Almer, *Physical Review B* **2006**, *73*,.

[199] W. Dmowski, T. Iwashita, C.-P. Chuang, J. Almer, T. Egami, *Physical review letters* **2010**, *105*, 205502.

[200] U. K. Vempati, P. K. Valavala, M. L. Falk, J. Almer, T. C. Hufnagel, *Physical Review B* **2012**, *85*,.

[201] D. Denisov, M. Dang, B. Struth, G. Wegdam, P. Schall, *Scientific Reports* **2013**, *3*,.

[202] Y. Sun, A. Concustell, A. L. Greer, *Nature Reviews Materials* **2016**, *1*, 1–14.

[203] Y. Tong, T. Iwashita, W. Dmowski, H. Bei, Y. Yokoyama, T. Egami, *Acta Materialia* **2015**, *86*, 240–246.

[204] M. Falk, J. Langer, *Physical Review E* **1998**, *57*, 7192.

[205] V. Chikkadi, S. Mandal, B. Nienhuis, D. Raabe, F. Varnik, P. Schall, *Europhysics Letters* **2012**, *100*, 56001.

[206] E. D. Cubuk, R. Ivancic, S. S. Schoenholz, D. Strickland, A. Basu, Z. Davidson, J. Fontaine, J. L. Hor, Y.-R. Huang, Y. Jiang *et al.*, *Science* **2017**, *358*, 1033–1037.

[207] R. Jana, L. Pastewka, *Journal of Physics: Materials* **2019**, *2*, 045006.

[208] B. Doliwa, A. Heuer, *Physical Review E* **2000**, *61*, 6898.

[209] K. Jensen, D. A. Weitz, F. Spaepen, *Physical Review E* **2014**, *90*, 042305.

[210] H. Jacobs, A. Tao, A. Schwartz, D. Gracias, G. Whitesides, *Science* **2002**, *296*, 323–325.

[211] M. Wong, S. Nakamura, S. DenBaars, *ECS J. Solid State Sci. Technol* **2020**, *9*, 015012.

[212] T. Jung, J. Choi, S. Jang, S. Han, *SID Symp. Dig. Tech. Pap* **2019**, *50*, 442–446.

[213] J. Smith, R. Ley, M. Wong, Y. Baek, J. Kang, C. Kim, M. Gordon, S. Nakamura, J. Speck, S. Denbaars, *Appl. Phys. Lett* **2020**, *116*, 071102.

[214] M. Wong, J. Kearns, C. Lee, J. Smith, C. Lynsky, G. Lheureux, H. Choi, J. Kim, C. Kim, S. Nakamura, J. Speck, S. DenBaars, *Opt. Express* **2020**, *28*, 5787.

[215] M. Wong, D. Hwang, A. Alhassan, C. Lee, R. Ley, S. Nakamura, S. DenBaars, *Opt. Express* **2018**, *26*, 21324–21331.

[216] D. Hwang, A. Mughal, C. Pynn, S. Nakamura, S. DenBaars, *Appl. Phys. Express* **2017**, *10*, 032101.

[217] T. Kim, J. McCall, Y. Jung, X. Huang, E. Siuda, Y. Li, J. Song, Y. Song, H. Pao, R. Kim, C. Lu, S. Lee, I.-S. Song, G. Shin, R. Al-Hasani, S. Kim, M. Tan, Y. Huang, F. Omenetto, *Science* **2013**, *340*, 211–216.

[218] H. Lee, J. Shin, J. Park, S. Hong, S. Park, S. Lee, J. Lee, I. Kang, K. Lee, *Adv. Funct. Mater* **2019**, *29*, 1–14.

[219] J. Wierer, N. Tansu, *Laser Photon. Rev* **2019**, *1900141*, 1900141.

[220] E. Xie, R. Bian, X. He, M. Islim, C. Chen, J. McKendry, E. Gu, H. Haas, M. Dawson, *IEEE Photonics Technol. Lett* **2020**, *32*, 499–502.

[221] J. Park, J. Kim, S. Kim, W. Cheong, J. Jang, Y. Park, K. Na, Y. Kim, J. Heo, C. Lee, J. Lee, F. Bien, J. Park, *Sci. Adv* **2018**, *4*, 1–12.

[222] K. Ding, V. Avrutin, N. Izyumskaya, U. Ozgur, H. Morkoc, *Appl. Sci* **2019**, *9*, 1206.

[223] P. Levermore, T. Schenk, H.-R. Tseng, H.-J. Wang, H. Heil, A. Jatsch, H. Buchholz, E. Bohm, *SID Symp. Dig. Tech. Pap* **2016**, *47*, 484–486.

[224] M. Singh, H. Haverinen, P. Dhagat, G. Jabbour, *Adv. Mater* **2010**, *22*, 673–685.

[225] M. Choi, J. Yang, T. Hyeon, D.-H. Kim, *npj Flex. Electron* **2018**, *2*, 10.

[226] B. Kim, M. Onses, J. Lim, S. Nam, N. Oh, H. Kim, K. Yu, J. Lee, J. Kim, S. Kang, C. Lee, J. Lee, J. Shin, N. Kim, C. Leal, M. Shim, J. Rogers, *Nano Lett* **2015**, *15*, 969–973.

[227] R. Cok, M. Meitl, R. Rotzoll, G. Melnik, A. Fecioru, A. Trindade, B. Raymond, S. Bonafede, D. Gomez, T. Moore, C. Prevatte, E. Radauscher, S. Goodwin, P. Hines, C. Bower, *J. Soc. Inf. Disp* **2017**, *25*, 589–609.

[228] C. Bower, M. Meitl, B. Raymond, E. Radauscher, R. Cok, S. Bonafede, D. Gomez, T. Moore, C. Prevatte, B. Fisher, R. Rotzoll, G. Melnik, A. Fecioru, A. Trindade, *Photonics Res* **2017**, *5*, 23.

[229] S. Cho, D. Lee, S. Kwon, *Conf. Solid-State Sensors Actuators Microsystems Eurosensors* **2019**, *XXXIII*, 402–404.

[230] J. Fang, K. Böhringer, *J. Micromechanics Microengineering* **2006**, *16*, 721–730.

[231] E. Snyder, J. Chideme, G. Craig, *Jpn. J. Appl. Phys* **2002**, *41*, 4366.

[232] E. Saeedi, S. Kim, J. Etzkorn, D. Meldrum, B. Parviz, *Proc. 3rd IEEE Int. Conf. Autom. Sci. Eng. IEEE CASE* **2007**, 375–380.

[233] M. Rein, V. Favrod, C. Hou, T. Khudiyev, A. Stolyarov, J. Cox, C. Chung, C. Chhav, M. Ellis, J. Joannopoulos, Y. Fink, *Nature* **2018**, *560*, 214– 218.

[234] W. Wong, T. Sands, *Appl. Phys. Lett* **1998**, *72*, 599–601.

[235] T. Ueda, M. Ishida, M. Yuri, *Jpn. J. Appl. Phys* **2011**, *50*, 1–6.

[236] M. Wong, C. Lee, D. Myers, D. Hwang, J. Kearns, T. Li, J. Speck, S. Nakamura, S. Denbaars, *Appl. Phys. Express* **2019**, *12*, 097004.

[237] S. Gandrothula, T. Kamikawa, M. Araki, D. Cohen, J. Speck, S. Nakamura, S. DenBaars, *Appl. Phys. Express* **2020**, *13*, 041003.

[238] D. Hwang, B. Yonkee, B. Addin, R. Farrell, S. Nakamura, J. Speck, S. DenBaars, *Opt. Express* **2016**, *24*, 22875.

[239] X. Zou, X. Zhang, W. Chong, C. Tang, K. Lau, *IEEE Trans. Electron Devices* **2016**, *63*, 1587–1593.

[240] C. Kang, S. Kang, S. Mun, S. Choi, J. Min, S. Kim, J. Shim, D. Lee, *Sci. Rep* **2017**, *7*, 1–9.

[241] J. R. Tumbleston, D. Shirvanyants, N. Ermoshkin, R. Janusziewicz, A. R. Johnson, D. Kelly, K. Chen, R. Pinschmidt, J. P. Rolland, A. Ermoshkin, E. T. Samulski, J. M. DeSimone, *Science* **2015**, *347*, 1349–1352.

[242] A. R. Rezk, O. Manor, L. Y. Yeo, J. R. Friend, *Proceedings of the Royal Society A: Mathematical Physical and Engineering Sciences* **2014**, *470*, 20130765.

[243] S. Agarwal, M. M. K. Khan, R. K. Gupta, *Polymer Engineering & Science* **2008**, *48*, 2474–2481.